A fibre optic based-high resolution manometer with hydrodynamic and contact
pressure specificity

by

Christopher Michael Bueley
BSc., University of Alberta, 2008

A Thesis Submitted in Partial Fulfillment
of the Requirements for the Degree of

MASTER OF APPLIED SCIENCE

in the Department of Mechanical Engineering

# Supervisory Committee

A fibre optic based-high resolution manometer with hydrodynamic and contact
pressure specificity

by

Christopher Michael Bueley
BSc., University of Alberta, 2008

**Supervisory Committee**

Dr. Peter Wild, Department of Mechanical Engineering
**Supervisor**

Dr. Martin Jun, Department of Mechanical Engineering
**Department Member**

# Abstract

**Supervisory Committee**

Dr. Peter Wild, Department of Mechanical Engineering
**Supervisor**

Dr. Martin Jun, Department of Mechanical Engineering
**Department Member**

Pressure within the esophagus arises from two mechanisms: intrabolus pressure, which is a hydrodynamic phenomenon, and esophageal occlusion pressure, which is a contact phenomenon. Current esophageal manometers are sensitive to both hydrodynamic and contact pressures and cannot distinguish between the two measurements in the absence of other information. It has been shown that measurement of intrabolus pressure is a clinically relevant parameter in esophageal manometry. There is no single device available that can obtain this measurement directly.

This work presents a novel fibre optic-based flexible catheter for high resolution manometry with sensing pods that can be selectively sensitized to either hydrodynamic pressure alone, or contact and hydrodynamic pressure, offering sensing schemes not possible with existing high resolution manometers. The catheter is designed to be used with a time division multiplexing interrogation technique, yielding a system capable of exceeding the 36-sensor count limit of current solid state manometers.

The device consists of rigid sensing pods connected by flexible tubing with in-fiber Bragg gratings acting as sensing elements within each of the pods. Absent in each sensing pod are rigid anchor points, representing a novel departure from comparable designs and resulting in increased sensitivity and decoupling from axial loading.

Device functionality is demonstrated through bench top trials. A pressure sensitivity of 1.8 pm/mmHg and axial sensitivity of 11 mmHg/N of applied load is demonstrated. Crosstalk between individual sensors is characterized and a compensation scheme is developed and validated. Temperature response is demonstrated to be linear such that its confounding can be corrected for procedurally.

Sensing schemes afforded by this design may yield clinically relevant parameters not achievable by any single existing device.

# Table of Contents

# List of Tables

# List of Figures

# Acknowledgments

I would like to thank first and foremost my advisor, Dr. Peter Wild, whose direction, knowledge and patience has made this work possible.

General assistance from Rodney Katz, Maxym Rukosuyev and later Jesse Coelho and Evan Poulton has also been very much appreciated. I am also grateful to Dr. Martin Jun for providing access to his micromachining lab and general technical advice.

I would like to thank all of my lab mates for helping to foment the great congenial work environment that made coming into the lab every day a pleasure; with particular gratitude to Chris Dennison, Dave Singlehurst, Nigel David and Devan Bouchard. The technical feedback you guys have provided has been invaluable.

Finally, I would like to thank Jennifer Magdalenich for her contribution to some figures in this text, but more so for her support while I was completing this work.

# Dedication

To my family.

# Chapter 1

## 1. Introduction

Advances in the understanding and diagnosis of gastrointestinal disorders are being facilitated in part through the development and implementation of catheters for High Resolution Manometry (HRM), defined as the acquisition of a series of pressure measurements with a spatial pitch of 10 mm or less in a section of the gastrointestinal tract. In the case of esophageal manometry, this is achieved by inserting through the nose a long, slender device with a series of sensing locations distributed along its length.

Current technology is such that solid state HRM devices are available with up to 36 sensing sites; the approximate upper limit achievable with existing commercial designs. Recently, there have been developments in the application of fibre optics to HRM that have yielded designs with numbers of sensing sites exceeding the current limit of 36. These optical designs have typically employed a sensing mechanism based on in-Fibre Bragg Gratings (FBGs), whereby strains within short sections of optical fibre are determined by measuring shifts in reflected wavelengths.

Pressure within the esophagus during peristalsis is comprised of two components: a contact luminal occlusion pressure and a hydrodynamic intrabolus pressure. All existing HRM devices and the majority of reported optical-based systems are sensitive to both hydrodynamic and contact pressures and as a result, are unable to differentiate between the two in the absence of other information. Intrabolus pressure is the only direct indicator for assessment of bolus transport function and its importance has been identified as one of many clinically relevant parameters in esophageal manometry, as discussed

later in this thesis. There is currently no device capable of directly differentiating intrabolus pressure from luminal occlusion pressure.

Singlehurst *et al.* [1] have reported a fibre optic-based distributed pressure sensor that is sensitive to hydrodynamic pressure alone, potentially affording a solution to intrabolus pressure measurement in application to HRM. However, the design has not been shown to be sufficiently flexible nor achieve the required sensor spacing for this application. A method is also lacking to sensitize it to contact pressure − a measurement sought in addition to intrabolus pressure. Lastly, the optical interrogation scheme used in conjunction with this design is not able to achieve 36 sensing points.

Addressing these shortcomings has been the focus of this work. By adapting the opto-mechanical sensing mechanism from Singlehurst's proposal and concurrently developing a novel Time Division Multiplexing (TDM) interrogation technique, an HRM system has been designed that yields more than 36 sensing sites; each individually configurable to sense either hydrodynamic pressure alone, or contact and hydrodynamic pressure. This customizable pressure specificity may offer sensing schemes not possible with existing devices.

This thesis is a presentation of the mechanical sensing component of the novel HRM system.

## 1.1. Objectives

There have been two primary research streams necessary to develop this proposed HRM package: (1) development of the TDM interrogation unit, and (2) development of the mechanical sensor array.

Development of the interrogation unit has been conducted by others and is beyond the scope of this thesis.

The focus of work presented here is the development of the mechanical HRM sensing package. Specifically, the objectives of the work reported here have been as follows:

1. Design a base mechanical sensing unit such that it achieves the performance specifications of HRM by adapting and further developing the sensing mechanism proposed by Singlehurst;

2. Develop a fabrication method, including material selection and assembly techniques, which can be used to produce prototypes of the mechanical sensor array;

3. Construct prototype sensors to demonstrate the fabrication methodology and with which to confirm function;

4. Demonstrate functionality of the mechanical sensing device through bench top testing of the constructed prototypes.

## 1.2. Methods

Content of thesis is organized into seven chapters, arranged as follows:

In Chapter 2, this thesis begins with a discussion of the anatomy of the human esophagus and a description of esophageal peristalsis to provide background information on the performance requirements for esophageal manometry. The technique of manometry is then introduced, followed by an introduction to High Resolution Manometry and its clinical significance whereby the shortcomings of existing devices are discussed. This chapter then adjusts focus to fibre optics, starting with a review of fundamentals of FBGs. This is followed by an assessment of existing fibre-optic based HRM designs, finishing with Singlehurst's optical sensing mechanism. Comment is then

made on the confounding influence of temperature and methods to address it in HRM. Next, a summary of alternative candidate optical interrogation systems is conducted, finishing with an overview of TDM. The chapter then concludes with a summary of the major findings from this literature review.

Chapter 3 begins with a table consolidating the performance specifications that have governed the design of the system. The chapter then presents the sensor system and provides a discussion of its major components and operating principle. This is followed by an analysis of various design parameters and a discussion of the theoretical sensitivity, benchmarking the design presented here against others. The chapter then provides a discussion of crosstalk and the methodology developed to correct for it. The chapter concludes with comment on potential novel sensing schemes possible with this design.

Chapter 4 provides an overview of the materials used to fabricate prototype sensors and includes a summary of the technique used to machine the components, followed by assembly methods.

Chapter 5 outlines the various bench top tests used to confirm sensor operation and overall device functionality.

Chapter 6 contains the outcomes of the tests and concludes with a discussion of the results in the context of high resolution manometry.

Chapter 7 concludes this thesis with a restatement of the objectives, a comparison of the demonstrated performance against the required specifications and finally a discussion of topics for future work.

# Chapter 2

## 2. Background Information and Literature Review

### 2.1. Introduction to the Human Esophagus

The esophagus is a slender muscular tube connecting the mouth to the stomach, comprised of three significant features: the Upper Esophageal Sphincter (UES), Esophageal Body (EB), and the Lower Esophageal Sphincter (LES). These structures are identified in Figure 1.
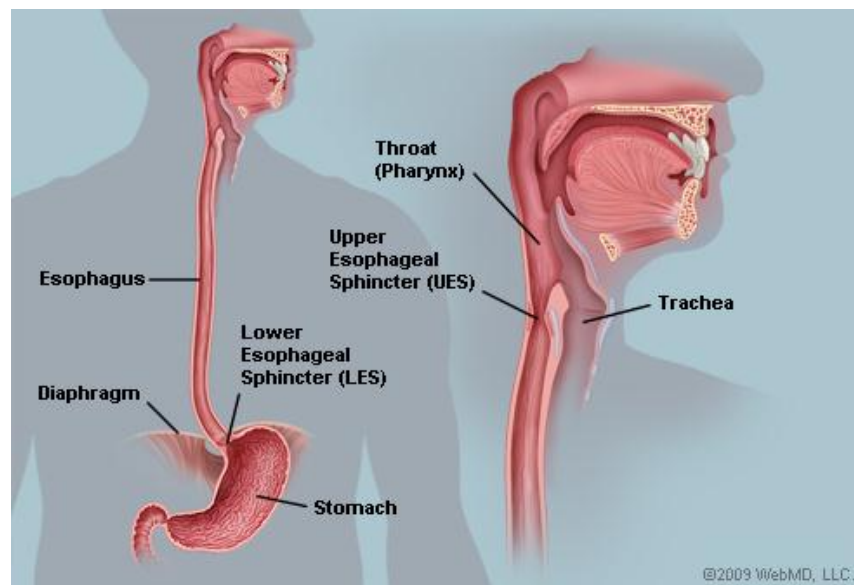


*Figure 1: Anatomy of the esophagus. The esophageal body extends from the UES to the LES and is not specifically identified here. Image reprinted with permission from [2].*

The UES is high pressure zone located at the top of the esophageal body, below the pharynx and associated structures at the back of the throat [3]. The UES acts as a physical barrier at the proximal-most section of the esophageal body and remains closed at its default (rest) state. The musculature of the UES is comprised of the cricopharyngeus

muscle, and to a lesser extent, the inferior pharyngeal constrictor [4]. The cricopharyngeal muscle forms a c-band around this section and produces maximum occlusion force (maximum muscular tension) in the anteroposterior direction, and lesser force in the lateral direction [3][5]. It is comprised of muscle fibre different than the surrounding structures as it consists of a blend of fast and slow-twitch fibres, whereas fast twitch fibres have a significantly lower concentration in the surrounding structures. The UES is also mobile, translating about 0.5 cm along the axis of the esophagus during peristalsis [5].

The esophageal body (EB), extends from the UES to the LES; a distance of about 18 to 25 cm, sphincter to sphincter. When distended, the cross section of the structure is approximately circular with a diameter of $2 - 3$ cm [3]. The musculature of the EB is comprised of two layers: an inner circular layer and an outer longitudinal layer. Between these two muscle layers exists a network of nerves which regulate muscle action, known as the myenteric plexus [4]. The proximal 5% of the esophageal body contains predominately striated muscle, which leads to a blend of striated and smooth muscle for the next 35% of the esophagus, and finishes with a section of smooth muscle for the remaining 60%, where it eventually concludes with the LES.

The LES is the distal-most high pressure zone, situated where the esophageal body merges with the stomach at the gastroesophageal junction. Like the UES, the LES is radially asymmetric. It has been shown that the clamping force of the LES is highest toward the left posterior direction, owing to the asymmetric 'sling' of oblique gastric muscle fibres that exist on the left side. The remaining component of the LES is a circular layer of esophageal smooth muscle fibre on the right side [3].

Together, these structures work in concert to transport material from the mouth to the stomach through the mechanism of peristalsis.

## 2.2. Fundamentals of Swallowing Mechanics

Peristalsis begins with the introduction of material, referred to as a bolus, into the oropharynx by a force applied by the tongue in the distal section of the oral cavity. This initial force against the bolus increases the intrabolus pressure, similar to applying a force to a constrained fluid [6]. Once accelerated, less force is required to maintain bolus velocity and the intrabolus pressure reduces [6]. A continuous series of contraction pressure waves within the oropharynx on the proximal side of the bolus, referred to as the 'tail' of the bolus, drives the bolus downward towards the hypopharynx, approaching the UES. This section is associated with a narrowing of the luminal passage, resulting in an increase in bolus velocity and reduction in intrabolus pressure as it enters the UES [7]. The peristaltic wave driving the bolus propagates at an average velocity of approximately 13 cm/s, corresponding to the speed of the bolus tail. However, the bolus head moves forward at a rate of 30-80 cm/s due to constriction of the pharyngeal structures [8]. Upon clearing the UES, the luminal diameter increases, resulting in a reduction in bolus velocity and an increase in intrabolus pressure. Complete bolus transport through the pharynx to the exit of the UES occurs rapidly, typically in less than 1 second [6]. Intrabolus pressure gradients through this region are produced primarily through inertial forces as the geometric changes create frequent variations in fluid velocity [9].

Within the esophageal body, beginning distal of the UES, the driving peristaltic wave reduces its velocity to 2 – 4 cm/s [6]. Intrabolus pressure gradients within the esophageal

body result primarily from viscous effects due to the low speed and circular, uniform geometry of the structure, in contrast to the inertia-dominated region above.

Brasseur *et al.* [6] have proposed a mathematical approximation of the intrabolus pressure gradient during active peristalsis within the esophageal body, given as

$$\frac{\Delta p}{\Delta x} = -\frac{32\mu}{\pi} \frac{A + \pi v D^2}{D^4} \tag{2.1}$$

where μ is the bolus viscosity, $v$ is the velocity of the bolus fluid, $A$ is a constant relating to fluid friction, and $D$ is the diameter of a given cross section within the bolus. As shown in Equation 2.1, the pressure gradient is proportional to $1/D^4$, indicating that the maximum change in pressure occurs near the bolus tail where the diameter approaches zero. This is also the location of the greatest intrabolus pressure as the frictional forces are largest at the point of esophageal contraction [6], as indicated in Figure 2. Within the bolus, away from the head and tail, the diameter is largest and relatively constant, which results in only gradual variation of intrabolus pressure. It should be noted that this analysis assumes perfect sealing at the bolus tail and a non-zero bolus velocity. A static (non-translating) bolus will have an intrabolus pressure the same everywhere [6].
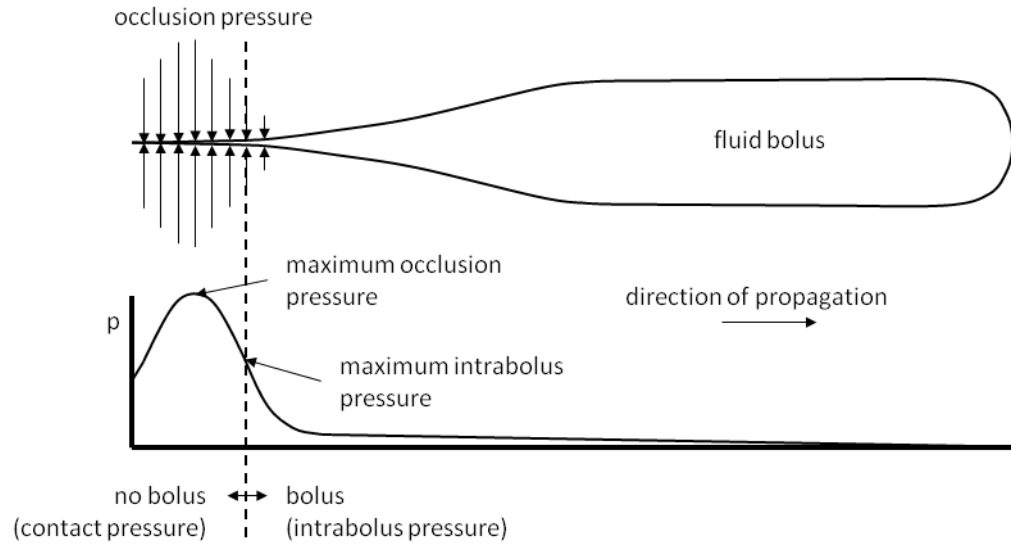
*Figure 2: Demarcation between luminal occlusion pressure and intrabolus pressure. Top image is a schematic of bolus geometry assuming perfect sealing at the bolus tail. Left of the dashed line represents the esophageal section devoid of bolus fluid where esophageal pressure is the result of contact pressure. Right of the dashed line is the bolus-filled section where pressure is hydrodynamic. Maximum intrabolus pressure occurs at the demarcation line. This figure is adapted from [6].*

Bolus transit is facilitated by a continuous contractile wave at the bolus tail. This contractile wave arises from the constriction of the circular-oriented muscle within the esophageal wall, shown as 'occlusion pressure' in Figure 2. The peristaltic contraction wave works to constrict the esophageal lumen and drive the bolus distally towards the stomach. During peristalsis, pressure within the esophagus is the result of occlusion or contact pressure in the region proximal of the bolus, and hydrodynamic pressure within the bolus. These two distinct regions are demarcated by the transition from no bolus to bolus, respectively. This demarcation is shown as a vertical dashed line in Figure 2. With perfect sealing, defined as complete occlusion of the esophagus proximal of the bolus, contact pressure and intrabolus pressure are fundamentally independent [6][10].

The independence between pressures in these two regions arises from the lack of bolus fluid connecting them. As there is no common fluid, hydrodynamic forces are not communicated from one region to the next and, as a result, the forces acting on the surface of the bolus, which are responsible for the intrabolus pressure and bolus transport, are independent of the occlusion pressures on the proximal side of the demarcation line [6]. This is true when the occlusion pressures are sufficient to achieve perfect sealing. For this reason, measurement of peristaltic wave amplitude is not a direct measure of bolus transport.

Perfect sealing occurs only when the occlusion pressure exceeds the maximum hydrodynamic pressure of the bolus. Retrograde bolus leakage can occur if the occlusion pressure is insufficient, allowing penetration of the bolus fluid into the contractile zone. Investigations by Kahrilas *et al.* [11] indicate that the minimum occlusion pressures necessary to seal a bolus are approximately 15 mmHg and 35 mmHg in the proximal and distal regions of the esophagus, respectively. These findings suggest that the maximum intrabolus pressure is somewhere in this range, consistent with findings by others [9][12]. The differences in required sealing pressures along the length of the esophagus have been attributed to the increase in basal pressure (non-peristaltic baseline pressure) as measurement locations approach the stomach [10].

The distinction between occlusion and intrabolus pressure is significant in the study esophageal manometry. For example, Tutuian *et al*. [13] report in a study that 51% of patients diagnosed manometrically with Diffuse Esophageal Spasm (DES) still experience successful bolus transport for both liquid and viscous boluses. Junlong *et al.* [10], among others [9][12], argue that measurement of maximum intrabolus pressure is

necessary to generate a thorough understanding of bolus transit and is likely an important clinical indicator in some esophageal dysfunctions [14].

Despite its importance, this measurement can be difficult to achieve in practice as conventional devices used in esophageal manometry are sensitive to both contact and hydrodynamic pressures. It is generally not possible to distinguish between the two measurements in the absence of other information, as discussed in the following section.

## 2.3. Esophageal Manometry

Investigation of esophageal peristalsis is conducted through means of esophageal manometry. In practice, a long, slender device is introduced nasally into the esophageal tract with pressure sensing regions distributed along its length. Peristalsis is initiated in a recumbent patient by introducing a swallow of 5 – 10 ml of water while pressure readings are recorded at each sensing site as function of time. Multiple swallows are typically conducted (greater than 10), spaced sufficiently to allow the esophagus to clear between trials. The pressure-time information for all sensing sites are plotted and interpreted together to assess overall patterns and assist in the diagnosis of a number of esophageal motility dysfunctions.

Esophageal manometry is considered the 'gold standard' for assessment of impaired esophageal motor function [5] and is indicated for patients experiencing dysphasia (difficulty swallowing) in the absence of a mechanical obstruction capable of explaining the symptoms [4]. The major elements investigated through manometry are efficacy of esophageal peristalsis and degree of sphincter relaxation, for both the UES and LES.

Achlasia, Diffuse Esophageal Spasm (DES), and non-specific motor disorders all have distinct manometric patterns [5].

Esophageal pressure measurements are achieved through two primary methods: water perfusion instruments and solid state sensors. Water perfusion methods use a multi-lumen tube connected to a mechanical pump external to the patient to continually perfuse the tube with water while in the esophagus. The outer diameter of a conventional multi-lumen tube is on the order of 4 - 5 mm, with 7 to 8 sensing ports spanning the esophageal body for conventional instruments. The back-pressure within each lumen is measured and recorded, from which esophageal pressure can be inferred. The spacing between sensing points on many conventional water-perfused systems is approximately 4 cm, longer than the contractile area of the LES, which makes it difficult to assess LES contraction. To address this, a sleeve device is placed over a few of the distal-most sensing points of the manometer spanning the structure of the LES. This sleeve device allows the multi-lumen manometer to record the maximum pressure generated anywhere along the length of the sleeve, affording measurement of the occlusion pressure generated at the sphincter.

Water perfusion methods utilize low cost, durable equipment and have historically been the most widely used. They are limited however, in their application for assessment of pharyngeal contraction as this measurement requires a frequency response of at least 60 Hz; exceeding the achievable frequency response of water-perfused devices due to system compliance. Additionally, water-perfused methods are sensitive to hydrostatic influences (water column height, for example), and differences in resistance to flow in different luminal channels [5]. These methods also force patients who are already

experiencing difficulty swallowing to consume water constantly perfused by the device during operation, which can lead to poor tolerance.

An alternative device for esophageal manometry is a sensor array instrumented with electrical solid-state sensing points. These devices can be made with a smaller diameter than conventional water perfusion devices, though the advantage of this is considered marginal [5]. The two primary advantages of these devices are the increased frequency response and the lack of water perfusion. The frequency response of these devices makes them suitable for measurement within the pharynx. Disadvantages of these devices include high sensor cost and fragility compared to water perfusion systems.

Data produced by conventional manometry is typically presented as a pressure-time line plot for each of the sensing points. A schematic of device output for a typical, well-functioned swallow is presented in Figure 3.
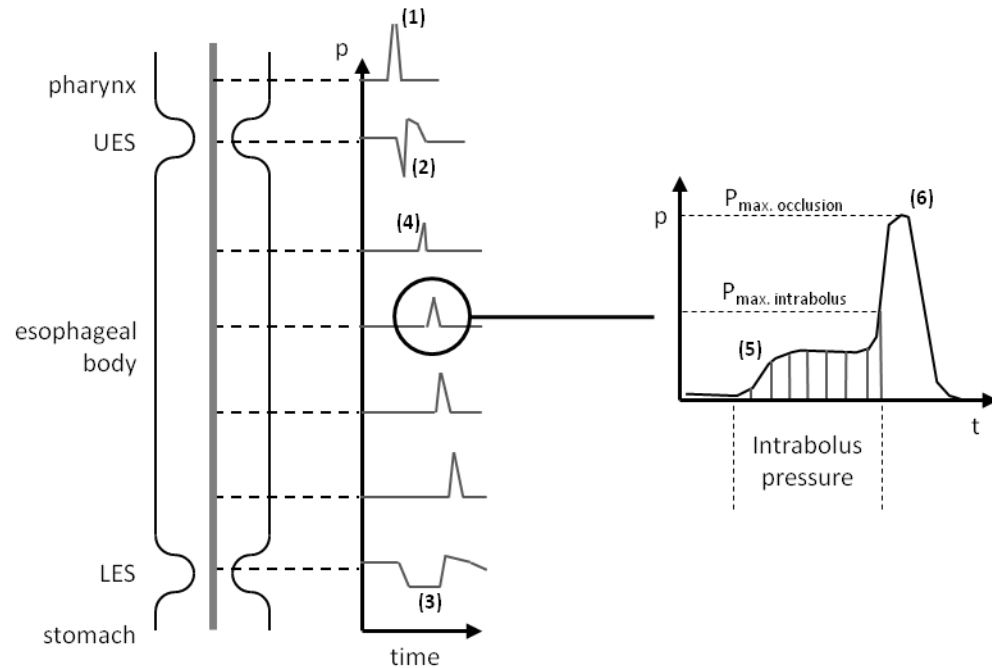
*Figure 3: Example pressure profile for normal peristalsis. Left – progression plot of peristalsis, right –indicated pressure profile within the esophageal body. Shaded area represents intrabolus pressure. Numbered items: (1) pharyngeal pressure wave, (2) relaxation of the UES, (3) relaxation of the LES, (4) peristaltic wave, (5) pressure reading corresponding to intrabolus pressure, (6) pressure reading corresponding to occlusion pressure. Conventional manometry alone cannot distinguish between intrabolus and occlusion pressure. The location of maximum intrabolus pressure shown here is approximated. Figure adapted from [15].*

Of note is the pharyngeal pressure wave that precedes all other readings and which indicates the commencement of peristalsis, identified as (1) in Figure 3. Following this is the simultaneous relaxation of the UES and the LES, noted (2) and (3) respectively. The peristaltic contractile wave, item (4), is tracked through the esophageal body by the time-series of increasing pressure peaks. Inspection of the pressure waves within the esophageal body depict an initial marginal increase in pressure corresponding to intrabolus pressure, identified as (5), followed by a much larger increase in magnitude indicating esophageal occlusion pressure, identified as (6). The maximum intrabolus

pressure is not discernible from the pressure plot alone. It should be noted that the pressure increase depicting intrabolus pressure in Figure 3 has been idealized for clarity and it is not always easily discerned in practice.

The clinically-relevant features of these pressure-time series are the relaxation of the sphincters and the progression of the contractile wave through the esophagus. Sphincter relaxation is primarily a measure of contact pressure and is readily discerned by conventional manometry. The peristaltic pressure wave, however, is a combination of both intrabolus pressure and esophageal occlusion pressure, between which conventional manometric devices alone cannot distinguish.

## 2.4. High Resolution Manometry

Advances in technology have recently yielded esophageal manometers with sensing locations spaced at a pitch of 10 mm, center to center. Procedures making use of these devices are referred to as HRM. Similar to conventional manometers, these devices are available as water-perfused or solid state systems.

Sierra Scientific (Los Angeles, California), offer a solid state device with 36 sensing points that detects pressure through a proprietary electrical mechanism. Medical Measurement Systems (MMS), (Dover, New Hampshire) offer both a 36 sensing point solid state sensor and a 22 sensing point water perfused device. HRM devices currently available are known to be limited to approximately 36 sensors as an increase in sensor count results in stiffening of the device and an increase in diameter [16].

The primary advantage of HRM over conventional techniques is the ease of data interpretation; diagnosis is quicker and easier [4]. Instead of a series of pressure line

plots, data resolution is sufficient to produce colourful topographic pressure plots which more readily depict peristaltic patterns. Additionally, the frequency response of solid-state HRM sensors makes them suitable for measurement of pharyngeal contraction. The tight spacing of sensing points also affords the ability to measure contractile pressures within the LES without the use of a sleeve device.

Owing to these advantages, HRM has been demonstrated to yield superior diagnostic sensitivity and specificity of esophageal dysfunctions [4][17].

## 2.5. Measurement of Bolus Transit and Intrabolus Pressure

In recent years, there have been investigations of hydrodynamic intrabolus pressure as a potential clinical indicator, using both conventional and HRM techniques.

Pal *et al.* [9] conducted a study investigating the Intrabolus Pressure Gradient (IBPG) of a group of patients diagnosed with non-defined dysphasia. The IBPG was determined by overlaying pressure readings obtained via water perfusion manometry with images obtained using video fluoroscopy. Video fluoroscopy involves swallowing a radio-opaque dye, typically barium, in the presence of an x-ray camera to visually track bolus transit through the esophagus. The IPBG was determined using a post-processing method that required visually defining the boundaries of the bolus at discrete time steps and correlating the associated manometric pressures. With this method, Pal identified some previously undiagnosed mechanical constrictions within the esophagus and concluded that measurement of IBPG is clinically useful.

More recently, Ghosh *et al.* [12] conducted a study of bolus transport within the mid-esophagus of patients suffering from reflux esophagitus. The mid-section of the

esophagus is a section where peristaltic waves do not propagate continuously. In this region, a bolus is passed across a short, non-contractile segment (gap) of the esophagus via two separate and distinct peristaltic waves: one occurring proximal of the gap and the second, separate wave, occurring distal of the gap. The physical distance between conclusion of the proximal contractile wave and commencement of the distal contractile wave is referred to as the spatial jump.

In this study, Ghosh used procedures similar to Pal in which manometric pressure readings, this time using HRM, were compared to bolus boundaries identified using video fluoroscopy to determine the maximum intrabolus pressure. The maximum intrabolus pressure was in turn used to determine the length of the spatial jump that exists between contractile waves in this region of the esophagus. Ghosh determined that a larger spatial jump correlated to a propensity for bolus retention; again indicating that measurement of intrabolus pressure is clinically relevant.

Both of these investigations used manometry in conjunction with video fluoroscopy to determine pressures within the bolus. A device sensitive to hydrodynamic pressure alone may provide a more direct method of achieving these measurements and preclude the use of x-rays and time consuming post processing.

An alternative method of determining bolus transport is through the measurement of distributed electrical impedance. Electrical impedance techniques operate by measuring the impedance to alternating currents across two excited probes (cross-pairs) exposed within the esophagus. Measured impendence changes in response to the presence of a fluid bolus, and thus a distribution of impedance cross-pairs throughout the esophagus can provide information on bolus transport [18]. However, this technique does not

provide pressure information, so it must be combined with manometric sensors to provide a comprehensive picture of bolus transport. Both Sierra Scientific and MMS offer combined HRM-impedance devices.

Despite the combined bolus transport and pressure information provided by these devices, it may be difficult to employ them in attempts to repeat the studies described here in lieu of fluoroscopy as the impedance and pressure sensing locations are spatially offset. This offset between pressure and bolus-presence detection may necessitate post processing correction and it is not clear how accurately this can be done to reveal true maximum intrabolus pressure.

Again, a system sensitive only to hydrodynamic pressure may provide a more direct method of determining intrabolus pressure and accordingly, some clinically-relevant parameters.

## 2.6. Fibre Optic High Resolution Manometers

In last 10 years or so there have been investigations into the application of fibre optics to the field of HRM, with some designs promising to exceed the current 36 sensing point limit of commercially available solid state devices. The small form factor and ability to produce multiple sensing sites on a single optical fibre make these devices attractive for distributed sensing applications. To the knowledge of this author, all fibre optic-based HRM devices proposed to date rely on Fibre Bragg Gratings (FBGs) as a sensing mechanism [1][16] [19][20].

### 2.6.1. Fibre Bragg Grating Fundamentals

FBGs are defined as a periodic change in the index of refraction of an optical fibre core [21], a schematic of which is shown in Figure 4 (a). When light propagating within a fibre core encounters an FBG, a narrow band of light is preferentially reflected by the grating while the remainder of incident light passes through [22]. This condition is described by Bragg's law and the corresponding centre wavelength of the reflected band of light, referred to as the Bragg wavelength $\lambda_B$, can be calculated as

$$\lambda_B = 2n_{eff}\Lambda \tag{2.2}$$

where $\Lambda$ is the spatial period of the changes in refractive index and $n_{eff}$ is the effective index of refraction of the grating [22–24]. Light at this particular wavelength is reflected by the grating while the remainder of incident light proceeds through as transmission (Figure 4 (c)).
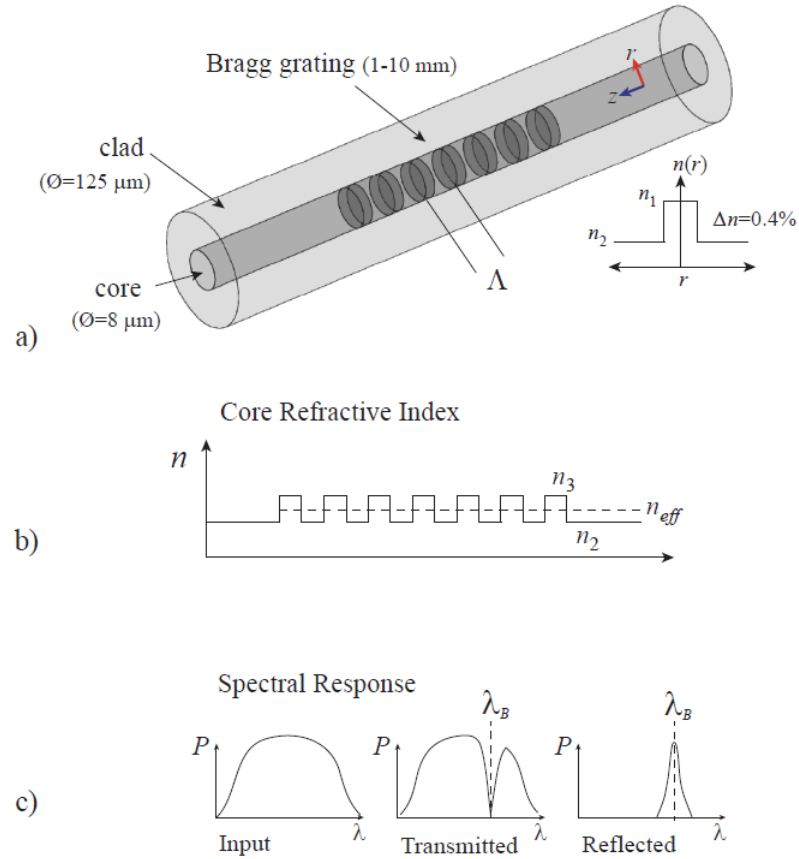
*Figure 4: Fibre Bragg Grating fundamentals. a) dark shaded areas indicated fibre core volumes of altered index of refraction b) periodic stepped-index of refraction profile in the fibre core along axis. c) spectral response of an FBG. Image reprinted with permission from N. David [25].*

Characteristics of the reflection spectrum, including spectral width and reflectivity, depend on grating length $L$, period $\Lambda$, intensity of perturbed index of refraction $n_3$, and magnitude of change in the refractive index $\Delta n$. The maximum reflectivity can be calculated according to [21]

$$R_{max} = tanh^2 \left[ \pi \left( \frac{\Delta n}{n_2} \right) \left( \frac{L}{\Lambda} \right) \right] \tag{2.3}$$

and the Full Width Half Max (FWHM), $\Delta\lambda_w$, can be calculated using [21]

$$\Delta \lambda_w = 2\lambda_B \left[ \left( \frac{\Lambda}{L} \right) \left( \frac{\Delta n}{2n_2} \right) \right]^{\frac{1}{2}} \tag{2.4}$$

As shown in the above equations, the reflectivity and spectral width of the Bragg reflection are related to grating length, among other variables. For a grating centered at a wavelength of 1550 nm, typical of many sensor applications, the spectral width (FWHM) can range from 0.2 nm to over 1 nm for grating lengths of 10 mm and 1 mm, respectively. Reflectivities can also vary from less than 1% to over 50%.

Fibre Bragg Gratings are inherently sensitive to temperature and fibre strain. It can be shown that the change in Bragg wavelength due to temperature and homogeneous isotropic strain can be expressed as [21]

$$\frac{\Delta \lambda_B}{\lambda_w} = (1 - p_e)\varepsilon + (a_\Lambda + a_n)\Delta T \tag{2.5}$$

where $p_e$ is the strain-optic coefficient, $\varepsilon$ is fibre strain, $a_\Lambda$ is thermal expansion coefficient of the fibre, $a_n$ is the thermo-optic coefficient and $\Delta T$ is the change in temperature from reference. Response to temperature is due primarily to the thermo-optic effect [24]. The strain-optic coefficient is a property of the optical fibre and can be calculated using

$$p_e = \left( \frac{n^2}{2} \right) [p_{12} - v(p_{11} + p_{12})] \tag{2.6}$$

where $p_{11}$ and $p_{12}$ are the components of the strain-optic tensor and $v$ is Poisson's ratio. In the absence of temperature influence, a grating centred in the 1550 nm band exhibits a linear wavelength shift in response to axial strain of approximately 1.2 pm/$\mu\varepsilon$ [22], providing a sensing mechanism. In the absence of strain, the same grating will respond to

temperature with a sensitivity of about 13 pm/$^{o}$C [22]. The sub-picometer wavelength resolution of modern commercially available optical interrogators allows resolving power of better than 1 $\mu\varepsilon$ and 0.1 $^{o}$C for strain and temperature, respectively.

The dual-sensitivity to both strain and temperature can be problematic in the development of sensors. The confounding influence of temperature can be addressed through the application of an additional grating isolated from strain to act as a temperature reference. In such a technique, both gratings respond to the influence of temperature, but only one grating responds to the measurand (strain), allowing compensation for the thermal effects [26].

Multiple sensing sites on a single optical fibre are achieved through the introduction of multiple gratings, referred to as multiplexing. There are a variety of methods to interrogate multiplexed FBGs, including Wavelength Division Multiplexing (WDM), Optical Frequency Domain Reflectometry (OFDR), and Time Division Multiplexing (TDM). These methods are described later in this section.

### 2.6.2. Applications to HRM

Early work to introduce fibre optics to the field of esophageal manometry was conducted by Swart, *et al.* [20][27]. Swart proposed a sensing mechanism based on a long, linearly-chirped FBG in an optical fibre housed within a continuous cylinder of pliable polymer. The operating principle was demonstrated by applying localized contact pressures to various locations along a 100 mm long chirped grating and measuring the group delay characteristics. Localized contact pressures applied along the length of the grating induced phase delay characteristics. Specifically, the location and magnitude of

the applied load were determined by the amount of phase change and the local slope of the phase change, respectively.

A key strength of this work is the distributed sensing ability of the grating-containing optical fibre. However, the device as demonstrated operated at 5 Hz; too slow for dynamic measurements within the human esophagus, though this limitation was the result of the time response of the phase detector used and may be remedied through an upgrade in equipment. More significantly, the sensor form factor is such that the optical fibre is the primary contributor to axial stiffness. This results in the overwhelming majority of any applied axial load to be carried by the sensing fibre. It has been reported that the peristaltic wave within the human esophagus can impart an axial load in excess of 140 g [28]; more than sufficient to swamp this sensor. Additionally, this form factor is expected to yield a sensor highly sensitive to localized bending as there are no structures present to keep sensing regions straight. This sensitivity to axial load and bending may limit the practicality of this design as an esophageal manometer.

A similar design has been proposed by Voigt *et al.* [19] and demonstrated by Becker [29]. In this design, discrete Bragg gratings are distributed along an optical fibre in lieu of one continuous chirped grating. A schematic of this design is shown in Figure 5.
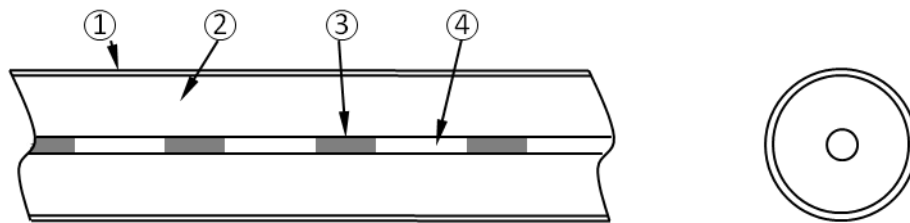


*Figure 5: Sensor schematic proposed by Voigt. Device shown cross-sectioned in two planes. Numbered items: (1) outer shell (high durometer silicone), (2) inner mantle (low durometer silicone), (3) FBG, (4) optical fibre. Pressure acts on the outer mantle and results in axial strain in the gratings.*

The fibre is housed in a compliant elastomer, similar to the proposal by Swart [20]. In this design, the elastomeric housing consists of a soft inner mantle, indicated as (2) in the figure, and a thin outer shell of high durometer silicone, indicated as (1). Individual gratings, item (3) in the figure, are interrogated through the use of wavelength division multiplexing (described in more detail in Section 2.7) at a rate of 1 KHz using a standalone interrogation unit (Blue Fiber Box, IPHT Jena, Jena, Germany). A system with 32 sensing sites has been demonstrated in bench top trials. Though an improvement in acquisition rate, this design is subject to the same limitations as the design proposed by Swart concerning axial and bending sensitivity.

An alternative design has been reported by Arkwright *et al.* [30]. This design consists of multiple 3 mm gratings distributed throughout the length of an optical fibre at a spacing of 10 mm whereby each grating-containing section of fibre is spanned across the open face of a c-shaped rigid substrate, as shown in Figure 6.
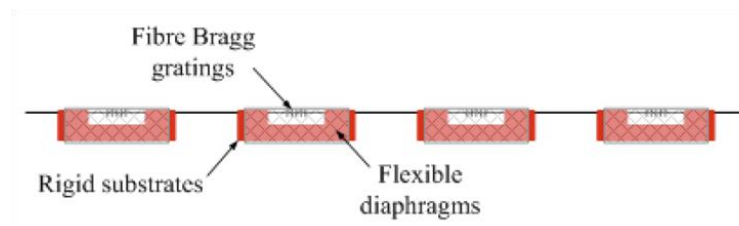


*Figure 6: Sensor schematic proposed by Arkwright. Fibre and rigid substrate assembly is sheathed in a silicone sleeve and potted with a soft silicone elastomer. Image reprinted with permission from OSA [30].*

A flexible diaphragm is wrapped over the open face of each substrate contacting the spanned fibre, providing the sensing mechanism. External pressure, contact or hydrodynamic, acts on the flexible diaphragm which imparts a transverse force to the fibre and induces strain within the grating. The entire substrate-fibre assembly is sheathed

in a silicone sleeve and potted with a low modulus silicone elastomer. The interrogation method used in this design is WDM. For reasons discussed in a later section (ref: Section 2.7), a maximum of 32 sensing sites may exist on a single optical fibre under these grating and interrogation parameters, so additional sensing sites on the device necessitate the use of extra optical fibre. Arkwright packages the additional fibre by crossing fibre strands at the midpoint between the substrates, allowing the overall sensor package to remain flexible. A sensor with 72 sensing points has been successfully demonstrated [16].

Of the optical esophageal manometer work discussed thus far, Arkwright's work is the most advanced as *in vivo* demonstrations in both the human esophagus and colon have been reported with promising results [31] [32].

The rigid substrate in this design helps to reduce the bending and axial sensitivity that confound other designs as each individual grating is supported independently and isolated, to some extent, from the fibre strain between sensing sites. In the experience of this author, however, it is generally not possible to completely isolate a grating from fibre strain beyond the envelope of the rigid substrate in these configurations. This suggests that the design likely suffers from axial load and bending sensitivity similar to designs by Voigt and Swart, albeit to a lesser extent. By inspection, it is suspected that the grating containing section of optical fibre provides an appreciable contribution to overall stiffness of the sensing regions, to the extent that an axial load of 140 g is likely sufficient to induce large (in the context of esophageal manometry) erroneous pressure readings. Actual sensitivity to axial loading is not reported, though Arkwright acknowledges the existence of this confounding influence and argues that the silicone sheath encasing the

sensor package will act to reduce the ability of the esophagus to 'grip' the sensor and load it axially. The efficacy of this is unknown.

An additional limitation is that this sensor design is sensitive to pressure in one radial direction only, which makes it orientation sensitive. This may be significant as it has been shown that orientation dependant sensors can be a source of error when measuring the contraction pressures of axially asymmetric esophageal structures, such as the UES and the LES [33].

Importantly, none of the optical sensor designs discussed thus far are able to discern between contact and hydrodynamic pressure, which generally limits their diagnostic functionality in the esophagus to that of existing solid state devices.

In contrast, Singlehurst has recently proposed an optical distributed pressure sensor design that is sensitive only to hydrodynamic pressure [1]. A schematic of the design is shown in Figure 7.
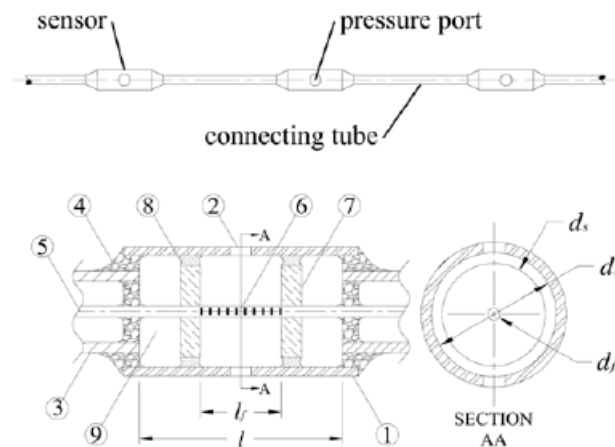


*Figure 7:  Sensor schematic reported by Singlehurst. Top – device form factor. Bottom – sensing mechanism. Components: (1) stainless tube, (2) sensing port, (3) Nitinol$^{TM}$ tube, (4) epoxy anchors, (5) optical fibre, (6) 1 mm Bragg grating, (7) pressure diaphragm. (8) silicone seals. Figure reprinted with permission from [1]. © IEEE 2012.*

The design uses rigid diaphragms, identified as item (7) in the figure, secured to the optical fibre (5) on either side of each Bragg (6) grating housed within a rigid stainless steel tube (1). An annular silicone seal (8) is created between the outer edges of the diaphragms and the inner surface of the stainless steel tube. The inner chamber is exposed to hydrodynamic pressure through two sensing holes distributed radially around the housing (2). Applied pressure imparts a force against the diaphragms, which in turn induces axial strain in the fibre Bragg grating. Adjacent pods are connected with Nitinol$^{TM}$ tubing (3) to provide flexibility.

Similar to proposals by Arkwright and Voigt, Singlehurst uses WDM to interrogate multiple Bragg gratings. This is a limiting factor compared to Arkwright's design as these gratings are 1 mm in length, in contrast to Arkwright's 3 mm gratings. The reduction in grating length results in an increase in the spectral width (FWHM) of each grating (ref. Equation 2.4), which further limits the total number of gratings that can be interrogated on a single optical fibre for reasons discussed later in Section 2.7. In this case, 23 gratings are possible compared to the 32 in Arkwright's design.

Singlehurst validated the operating principle of this design by constructing and testing a prototype with three pods spaced at 6 cm. To the knowledge of this author, this design is the only fibre optic-based distributed pressure measurement design that is not sensitive to contact pressure, making it suitable for directly discerning hydrodynamic (intrabolus) pressure when applied to HRM. Accordingly, it offers an attractive sensing mechanism on which to base further work.

While the fundamental sensing mechanism has been demonstrated, there are a number of design challenges in adapting this technology. The design as-reported has not been

shown to achieve sufficient flexibility for use in the esophagus, nor does it have the 10 mm spacing between sensing points required for HRM.

Discussions with Singlehurst have also indicated that this sensor package is significantly sensitive to axial loading and bending [34]. While no formal data has been collected addressing the magnitude of these confounding influences, Singlehurst argues that a protective silicone sheath, similar to that employed by Arkwright and Voigt, may serve to reduce the ability of the esophagus to 'grip' the sensor and apply axial load in practice [34]. Again, the efficacy of this method is unknown as any investigations into this have not been reported.

It should also be noted that a hydrodynamic pressure-specific manometer may still be required to be sensitive to contact pressures where sensing ports are in the proximity of the UES and LES, as contractile and relaxation pressures in these areas are diagnostically important. Therefore, the ability to sensitize select pods to contact pressure is required and no technique to achieve this has been reported.

Finally, the WDM interrogation method employed in this design limits the system to a lower sensor count than existing commercially available solid state and water perfusion manometers.

Addressing these shortcomings and adapting this sensing mechanism to HRM has been the focus of the work presented in this thesis.

### 2.6.3. The Influence of Temperature

It should be noted that all optical sensors reviewed here are intrinsically sensitive to the influence of temperature, as described in Equation 2.5. Voigt argues that the temperature profile is essentially constant for the length of the esophagus, so baseline readings with

the device warmed to the temperature of the esophagus are expected to be sufficient to minimize temperature variation error [19]. Ensuring swallows are conducted with liquid pre-warmed to the correct temperature may further reduce temperature variation affects. Arkwright provides no discussion of this potential source of measurement error despite having conducted *in vivo* trials [35].

Voigt's argument is substantiated by Pandolfino's discussion of thermal variation affects on Sierra Scientifics' solid state sensors and the method employed to correct it [36]. Pandolfino states that at the end of a clinical investigation, Sierra Scientific's software takes a baseline reading of the proximal-most sensing point immediately as it exits the nasal passage of the patient. At this instant, the sensing point is exposed to air yet remains at body temperature, affording a baseline pressure reading to use as a correction factor for all other sensing sites. This method is valid only under the assumption that all sensing points on the manometer are at the same temperature within the esophagus. It is reasonable to assume that this has been investigated by Sierra Scientific and determined to be valid, as this is the temperature correction method the company employs.

It is expected that a similar procedure can be used for fibre-optic designs.


## 2.7. Fibre Bragg Grating Interrogation Techniques

Three interrogation schemes suitable for reading multiplexed Bragg gratings include Wavelength Division Multiplexing (WDM), Optical Frequency Domain Reflectometry (OFDR) and Time Division Multiplexing (TDM).

### 2.7.1. Wavelength Division Multiplexing

WDM is the most straightforward of the three multiplexing techniques and is characterized by centering each Bragg grating at a unique wavelength. By knowing the centre wavelength, $\lambda_{Bi,}$ for each grating, $i$, strain and/or thermal information for each sensing point can be inferred by observing the wavelength shift of the corresponding spectrally-unique Bragg wavelength, as shown in Figure 8. This scheme is employed by many standalone commercially available optical interrogators, with scanning frequencies of 1 KHz or more.
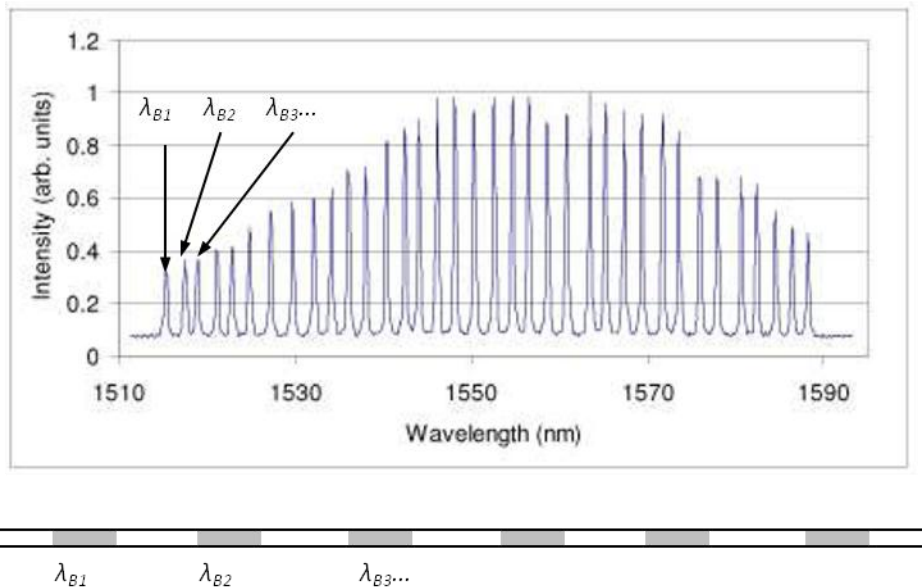


*Figure 8:  Wavelength Division Multiplexing technique. Top image shows unique spectral address for each grating. Bottom image shows corresponding locations of each grating within a sensing fibre, shown shaded. Bragg wavelengths, $\lambda_{Bi,}$ shift in response strain at the corresponding gratings. Variations in wavelength intensities are due to differences in gain levels. Image modified and reprinted with permission from OSA [16].*

The number of gratings that can be interrogated on a single optical fibre is a function of the available spectral width of the interrogation system. For example, with a given array of gratings in the 1550 nm band where each grating is 1 mm in length, it reasonable to

allocate about 3.5 nm of spectral width for each grating. This is to accommodate the 2 nm FWHM (ref. Equation 2.4) and the total dynamic range (total expected wavelength shift) of each grating. Spectral distance between gratings must be sufficient to ensure that reflected Bragg wavelengths are not able to 'shift' into adjacent peaks and overlap. Current interrogation systems from major manufacturers have a typical spectral width of 80 nm (SmartScan, Smart Fibres Ltd., Bracknell, UK), which allows about 22 of these hypothetical gratings to exist on a single fibre. Using longer grating lengths can increase the maximum grating count as this reduces the FWHM of each grating, but grating length is often dictated by the form factor of the sensing device so this is not always possible. Grating count can also be increased by reducing the dynamic range (total allowable wavelength shift) of the sensors, though this is typically determined by the application. For HRM, the required close spacing of the sensing points is such that grating lengths are necessarily on the order of a few millimetres. Thus, achieving more than 32 sensing points (or 23 in the case of Singlehurst's design) requires the use of multiple optical channels (multiple optical fibres) and quickly switching between them. While fast optical switching is offered by interrogators (SmartScan, Smart Fibres Ltd., Bracknell, UK), there are implications in the sensor design as the multiple optical fibres must be accommodated.

Another drawback of WDM is the high cost associated with manufacturing the sensing array. The requirement for each grating to have a unique Bragg wavelength is such that there is an increase in complexity and labor associated with increasing grating count. In the experience of this author, quotes of approximately $100/grating are typical for low quantity orders, which suggests a price approaching $3600 for the cost of the fibre alone

in a 36 grating sensor array. An additional cost with this system is the interrogator unit: prices ranging from $20,000-$35,000 per unit are typical.

## 2.7.2. Optical Frequency Domain Reflectometry

OFDR is a method that allows both strain and spatial information within an optical fibre to be determined. A schematic OFDR system as described by Soller *et al.* [37] is shown in Figure 9.
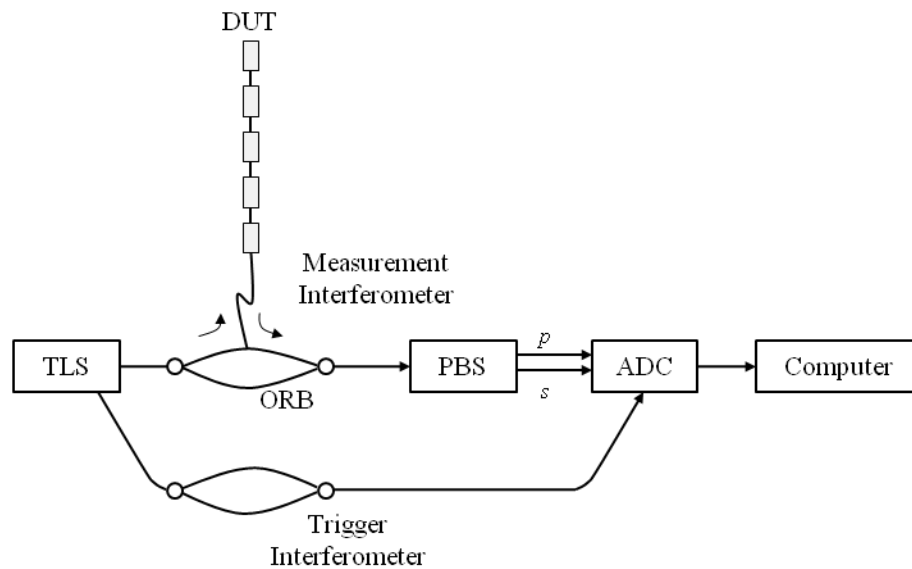


*Figure 9: Schematic OFDR system. Components: Tunable Laser Source (TLS), Device Under Test (DUT), Optical Reference Branch (ORB), Polarization Beam Splitter (PBS), Analogue to Digital Converter (ADC). P and S represent orthogonal polarization states. Frequency-dependant reflected light is time shifted when it returns from the DUT, where it is combined with the ORB which generates an interference pattern on the ADC. The interference pattern contains information concerning stain and displacement within the DUT. Figure adapted from [37].*

A Tunable Laser Source (TLS) launches frequency-varying light into a system as a continuously repeating linear saw tooth pattern. The incident light is evenly split between the Device Under Test (DUT), in this case an HRM device, and an Optical Reference

Branch (ORB). Light reflected within the DUT is a function of incident frequency. Thus, the frequency-varying laser results in light reflected from the DUT that is time-varying. This reflected light is also time-delayed relative to light from the reference branch. The reflected light is recombined with the light from the ORB, which generates a frequency-dependant coherent interference pattern incident on an optical receiver. The Polarization Beam Splitter (PBS) ensures that reflective events within the DUT that manifest as changes in polarization alone are detected. The amplitude of the current output of the optical receiver, which is a function of the intensity of the evanescent field incident upon it, provides information about the spectral return loss of the DUT. The phase of the recombined light carries information about the length and dispersion [37]. Applying an FFT to this frequency-intensity information allows spatial and strain information to be inferred. There are two methods of inferring fibre strain with this interrogation technique: FBGs and Rayleigh Backscatter.

FBGs change the local reflectivity of a fibre section in response to strain. Specifically, grating strain under this interrogation scheme manifests as a change in intensity in a reflectivity-distance plot, in contrast to a wavelength shift in WDM techniques. Strains are attributed to specific gratings based on the calculated distance. A key strength of this technique is that it allows, but does not require, all gratings within a fibre to exist at the same Bragg wavelength. This can significantly reduce manufacturing costs as the more efficient and less labour intensive method of writing gratings at the fibre draw-tower can be used to produce a grating array.

FBGs provide convenient reflective events because they are highly reflective and easily discernible from noise. However, through efforts to minimize system noise, the noise

floor can be reduced such that reflectivity due Rayleigh Backscatter becomes discernible [37], providing an alternative sensing mechanism.

Rayleigh Backscatter results from changes in refractive index in small volumes throughout the length of the fibre as a result of variations in core radius and density. It can be modelled as an FBG with a random but static period [38].

To determine fibre strain, a baseline reading of the DUT is first obtained to provide a reference. The fibre is then scanned again after the application of strain and the resulting reflectivity-distance plot, this time indicating Rayleigh Backscatter, is compared to the reference. The reflectivity-distance plot is mathematically sectioned and peak correlation is conducted. By matching reflective peaks from the strained plot against the reference plot, physical fibre displacement for discrete sections can be measured, indicating strain.

A significant advantage of this technique is that no gratings are required; a standard length of optical fibre can be used as a sensing mechanism, making the sensing fibre cost negligible. Additionally, this method affords truly distributed strain sensing.

Though promising, this technique is limited by scanning speed. To the knowledge of this author, the fastest demonstration of this technique has been 3 Hz; essentially static. Standalone units capable of achieving an interrogation frequency of up to 50 Hz are reportedly under development (Luna Technologies, Blacksburg, Virginia), though discussions with the development company have indicated that the unit cost will be significantly more than conventional WDM interrogators and no firm release date is available. The high cost and unknown equipment availability make this technique unattractive for the application of optical HRM.

### 2.7.3. Time Division Multiplexing

Time division multiplexing is a technique that allows the polling of individual gratings centred on the same Bragg wavelength by reading reflected pulses separated by a time delay. A system schematic for this method is given in Figure 10.
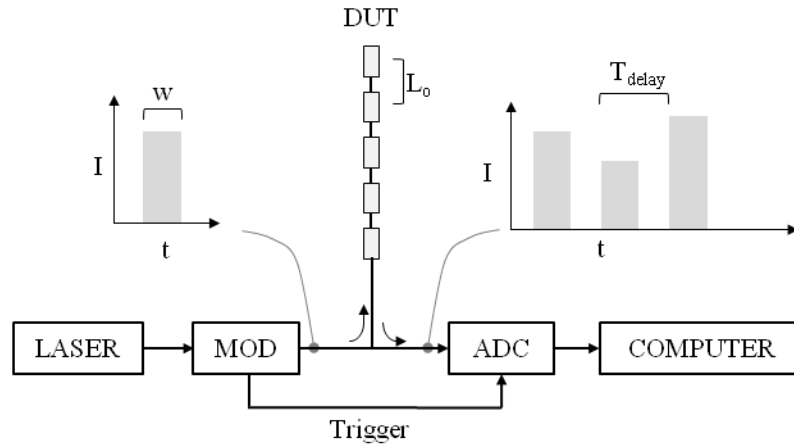


*Figure 10:  TDM schematic. MOD is a high frequency modulator, ADC is an analogue to digital converter. Top left plot represents interrogation pulse into the Device Under Testing, DUT, and the top right plot shows the resulting pulse train incident on the ADC (only the first three pulses are shown for clarity). Pulse intensities in the pulse train yield strain.*

Interrogation of the DUT commences with a single pulse into the system from the high frequency modulator. This pulse is directed into the DUT where it is partially reflected by each of a series of spatially distributed low reflectivity FBGs. Each grating reflects a portion of the input light pulse which results in a series of reflected pulses, referred to as a pulse train, separated by a timing delay, $T_{delay}$, given by

$$T_{delay} = \frac{2L_0 n_{eff}}{c_0} \qquad (2.7)$$

where $n_{eff}$ is the effective index of refraction of the optical fibre, $c_0$ is speed of light in a vacuum and $L_0$ is distance between gratings. The integer, 2, is present to indicate that the light pulse makes a round trip between each FBG; that is, it travels distance $L_0$ twice.

The pulse train consists of N light pulses, where N is the number of FBGs present. For FBGs with 10 mm spacing, as in the case of HRM, $T_{delay}$ is on the order of 100 ps.

The width of the interrogation pulse, indicated as $w$ in the figure, must be less than the delay between each pulse in the pulse train to ensure that individual pulses can be discerned. In practice, this value may be set to about half of $T_{delay}$, or 50 ps. Triggering is synchronized to the pulse train frequency, given as $1/T_{delay}$. This results in a required triggering frequency of about 10 GHz for a grating spacing of 10 mm.

To measure grating wavelength shifts, the laser wavelength, $\lambda_{Laser}$, is centered on the linear portion of the FBG reflection spectrum, as shown in Figure 11.
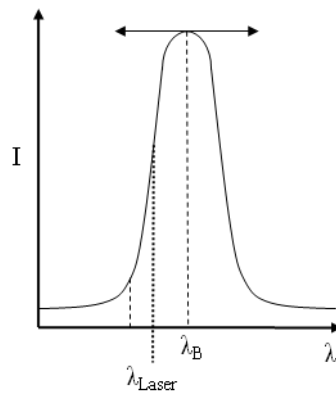


*Figure 11:   Intensity-modulation method of measuring Bragg wavelength shift. Interrogating laser wavelength, $\lambda_{Laser}$, is centered on the linear portion of the Bragg grating's reflection spectrum. Arrows indicate that the reflected spectrum shifts while the laser wavelength remains fixed. Measuring intensity, I, indicates wavelength shift.*

Information concerning strain in each grating is carried by the intensity of the reflected light pulses. The laser wavelength remains fixed while the reflected spectrum from each grating shifts in response to applied strain, thus strain within each grating can be determined by measuring the intensity of the corresponding light pulse in the pulse train.

The interrogation frequency of the DUT is determined by temporal pulse spacing and the number of gratings in the fibre. A new pulse cannot be fired into the device until the

pulse train resulting from the preceding input pulse has cleared. This results in a maximum time delay given by

$$T_{delay} = \frac{2L_0 n_{eff}}{c_0} \tag{2.8}$$

With 10 mm spacing and 36 sensors, this yields a polling frequency of about 278 kHz; the fastest of any method discussed.

Similar to OFDR-FBG methods previously described, this interrogation method benefits from the ability to have all gratings at the same centre wavelength, significantly reducing manufacturing costs relative to WDM. The maximum number of sensors achievable on a single fibre is governed by the sensitivity of the optical detector. Light pulses reflecting from the most distant gratings will be reduced in intensity by the gratings preceding it. While definitive numbers quantifying this effect have not been established, discussions with researchers in this field have indicated that the maximum number of gratings that can exist on a single sensor is approximately 50 [39].

It should be noted that the reflected intensity of a given grating will be attenuated by each of the gratings that exist between it and the optical detector, inducing optical crosstalk. To compensate for this, the reflected intensity of each grating must be determined sequentially from gratings 1 to N, where 1 is the proximal grating, such that the influence of the gratings preceding a given measured grating $n$, can be quantified and corrected.

A standalone TDM unit capable of achieving these performance specifications is not commercially available. However, advances in telecommunications technology are such that off the shelf equipment capable of meeting these requirements (laser, modulator, and

receiver) are currently available, suggesting that such a unit can be built. Collaboration with researchers in this field has indicated that the expected cost of a custom-built unit is likely to be in excess of existing WDM interrogators, but significantly less than the expected cost of OFDR units when they become available.

A commercially available TDM unit is expected to have application beyond HRM. Specifically, any distributed FBG-based optical sensing system may benefit from the availability of such a device, and the current lack of a comparable system on the market affords potential commercial opportunity.

In summary, the projected cost, performance specifications and the lack of a commercially available comparable unit have made this interrogation method an attractive scheme on which to base the development of an optical HRM system.

## 2.8. Summary

A review of fundamental swallowing mechanics has illustrated that measurement of esophageal occlusion pressure is not a direct indicator of the efficacy of bolus transit. Existing esophageal manometers are sensitive to both contact and hydrodynamic pressures and cannot distinguish between the two measurements in the absence of other information. It has been established that measurement of intrabolus pressure is clinically significant. Efforts have been made to combine manometric readings with information from video fluoroscopy and impedance measurements to determine intrabolus pressure, however a more direct method of obtaining true intrabolus pressure may be preferable.

Application of fibre optics to distributed pressure sensing offers the ability to exceed the 36 sensing point limit of current commercial HRM devices. However, the majority of

reported fibre-optic based distributed pressure sensor designs are sensitive to both hydrodynamic and contact pressure, generally limiting their functionality to that of existing HRM devices. One sensing mechanism design stands out as it is sensitive to hydrodynamic pressure alone. This design, proposed by Singlehurst, offers the ability to fill the measurement gap inherent in current esophageal manometry; specifically, the ability to measure and discern intrabolus pressure directly. It is for these reasons that Singlehurst's sensing mechanism has been selected to be adapted to a pressure-specific HRM system.

Of the three optical interrogation methods discussed, time division multiplexing represents the optimal technique to achieve the required 36 (or more) sensing points on a single optical fibre. However, no standalone TDM unit capable of achieving the required specifications is currently available. Development work in this area has also been conducted.

In summary, combining Singlehurst's fundamental sensing mechanism with a time division multiplexing interrogation scheme has afforded the ability to develop an HRM system that exceeds the current sensor count of existing devices and provide the ability to directly discern between hydrodynamic and contact pressure.

This thesis is a presentation of the mechanical sensing component of this HRM system.

# Chapter 3

## 3. Sensor Design and Analysis

This chapter provides details on the physical description, sensing principle, theoretical performance and pressure specificity of the mechanical HRM device.

The chapter begins with a summary of the sensor performance specifications, followed by a physical description of the device, including a discussion of the sensing mechanism. Next, this chapter outlines equations governing theoretical sensor performance, followed by the identification of various design constraints and parameters, ultimately yielding theoretical sensitivity and a benchmark against comparable designs. An analysis of mechanical crosstalk is then provided.

Finally, comment is made on the pressure-selective configurations afforded by this design and identification of potential novel sensing schemes in HRM.

### 3.1. Performance Specifications

Based on the requirements for high resolution esophageal manometry discussed in Section 2, Table 1 is a summary of the specifications that have guided the design of this sensor system.

*Table 1: Summary of sensor performance requirements*

| Specification | Target Value |
| --- | --- |
| Pressure specificity: | Two configurations<br><br>1. Sensitive to hydrodynamic pressure<br>2. Sensitive to hydro. and contact pressure |
| Pressure Resolution: | 1 mmHg |
| Pressure Range: | 0 – 400 mmHg |
| Sensing pitch: | 10 mm |
| Min. Bend Radius: | 50 mm |
| Max. Outside Diameter: | ~3 mm |
| Min. Sensor Count: | 36 |
| Min. Interrogation Frequency: | 60 Hz |

A description of the mechanical sensing device is provided in the following section.

## 3.2. Device Description

The developed distributed fibre optic pressure sensing device consists of a series of rigid sensing pods spaced at a pitch of 10 mm. Each pod is approximately 3.5 mm in length with an outside diameter of 2.8 mm, connected to adjacent pods with Nitinol$^{TM}$ tubing. Each pod has four rectangular sensing ports which allow applied pressure to reach the opto-mechanical sensing mechanism contained within. The unit-repeating nature of the sensing pods is such that the total number of sensing sites may be increased arbitrarily, limited only by the interrogation system.

The rigid pods and Nitinol$^{TM}$ tubing comprise a robust, flexible superstructure that houses an 80 μm optical fibre. The fibre exits the sensing array at proximal end of the superstructure and connects to the interrogation system, as indicated in Figure 12. The

sensing structure is comprised entirely of medical grade materials, including silicones and epoxies.
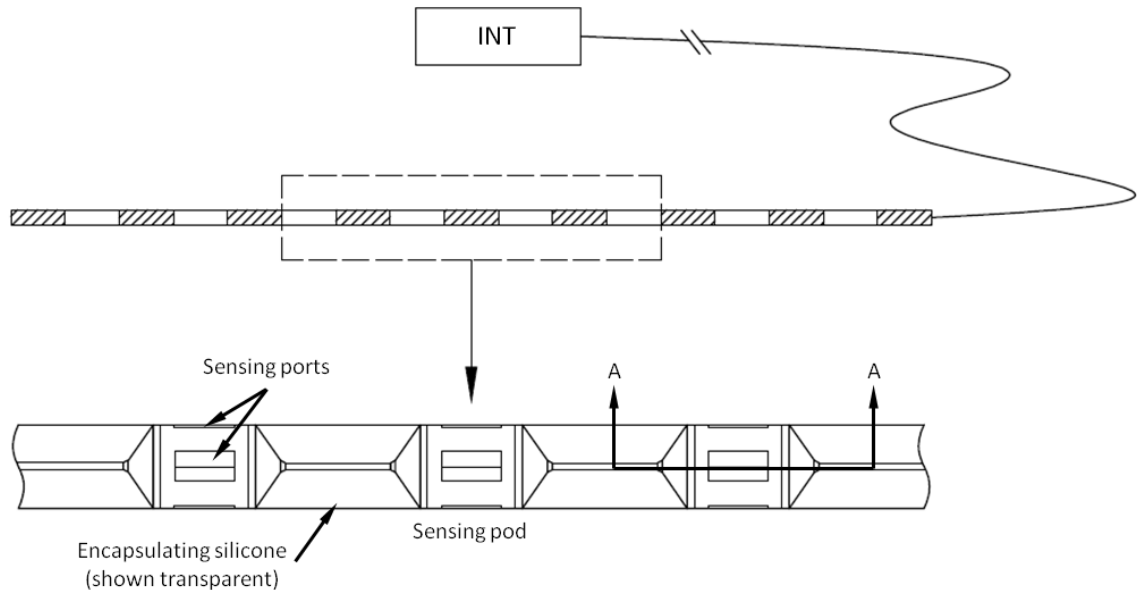


*Figure 12: Overview of HRM sensing system. Shaded areas in top image indicate sensing pods; nine pods shown here for clarity. 'INT' indicates interrogation system. Overall sensor diameter is approximately 3 mm. Metal superstructure is shown here continuously encased in silicone which may or may not be representative depending on sensing configuration. Section A-A shown in Figure 13.*

The superstructure is designed to be encased in a continuous uniform cylinder of high durometer silicone to provide compliance for patient tolerance, as indicated in the figure.

The device affords individual sensing pods to be selectively sensitized to specific pressure phenomena by providing two possible sensing configurations: (1) sensitivity to hydrodynamic pressure, or (2) sensitivity to both contact and hydrodynamic pressure. Details of the operating principle of the device for both sensing configurations are provided in the following section.

### 3.3. Operating Principle

The fundamental opto-mechanical sensing mechanism housed within each sensing pod is identical between the two possible sensing configurations: sensitivity to hydrodynamic pressure or sensitivity to hydrodynamic and contact pressure. This mechanism consists of an FBG-containing optical fibre spanned between two rigid pressure diaphragms, identified as items (1) and (2) in Figure 13, respectively. The diaphragms are secured to the optical fibre with epoxy anchors (7). The fibre is an intact polyimide-coated 80 μm single mode optical fibre. An annular flexible silicone seal (3) is located between the outer edge of the rigid diaphragms and the inner surface of the pod housing (4).
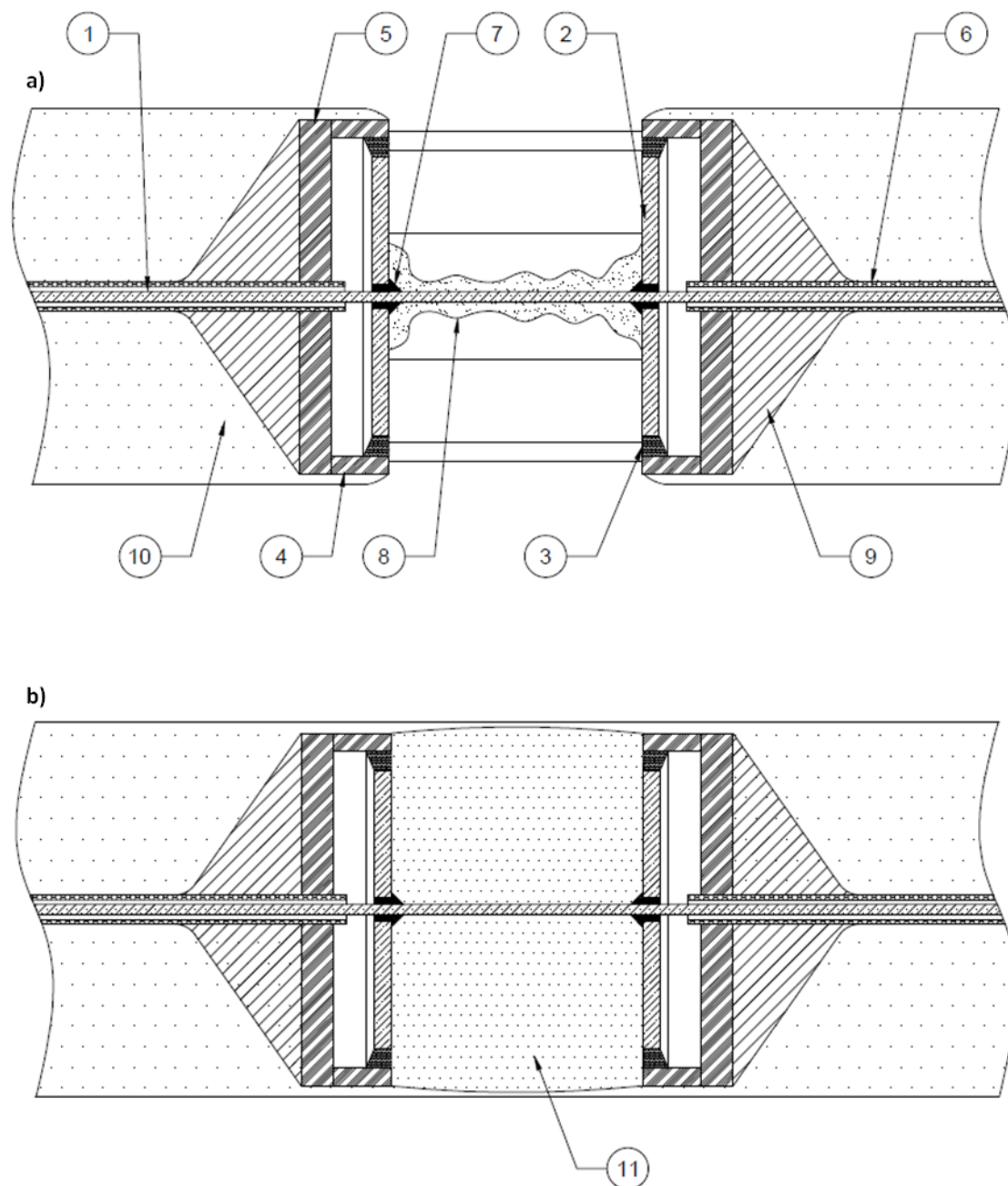
*Figure 13: Sensing pod cross section A-A (Ref. Figure 12). a) Hydrodynamic pressure-sensitive configuration. Pressure in this configuration acts on the inside face of item (2). b) Contact-sensitive configuration. Pressure in this configuration acts over the outside surface of the silicone (10). Components are as follows: 1) 80 $\mu$m optical fibre. 2) Rigid diaphragm. 3) Flexible silicone seal. 4) Pod housing. 5) Capping washer. 6) Nitinol$^{TM}$ tubing. 7) Epoxy anchors. 8) Sealing silicone. 9) Solder connection. 10) Encapsulating silicone. 11) Ultra-soft silicone potting gel. FBG is located midpoint between diaphragms.*

In the case of the hydrodynamic pressure-specific configuration (configuration (a) in Figure 13), pressurized fluid is allowed to enter the sensing pod and act directly upon the rigid diaphragms (2). This imparts a force normal to the inside surfaces of diaphragms which is resisted by the optical fibre, resulting in axial strain in the FBG-containing section of optical fibre. Thus, applied pressure is determined by monitoring grating strain, providing the sensing mechanism. The epoxy anchors and the spanned section of optical fibre are coated and sealed with low-durometer silicone (8) to provide a physical barrier separating these components from the pressurized fluid. Sealing these components from the pressurized fluid is important as polyimide (the outer coating of the fibre) and some epoxies are known to swell in the presence of water. The entire pod-tube superstructure is encapsulated in continuous high-modulus silicone (10), with the exception of the sensing ports, which are left open.

For the second configuration in which the pod is sensitive to both contact and hydrodynamic pressure (identified as configuration (b) in Figure 13), applied pressure acts on the outer surface of the encapsulating silicone (10) which compresses the ultra-soft silicone gel (11) that fills the internal cavity of the pod housing (4). Volume of the ultra-soft gel is preserved due to its Poisson's ratio, thus the gel expands axially. This axial expansion imparts a force to the rigid diaphragms and results in fibre strain in a similar fashion to the hydrodynamic pressure configuration. It should be noted that the pod structures are identical between the two possible sensing configurations (items $1 - 7$, $9 - 10$), with the exception of the ultra-soft silicone gel potting (11), which is unique to the contact-sensitive variant.

Of note in this design is the lack of rigid anchors securing the optical fibre to the sensor superstructure. The fibre-diaphragm assembly in this design, which consists of a combination of items (1) and (2) in Figure 13, is effectively free-floating as its only connection to the superstructure is through the flexible silicone seals, noted as item (3). This is a significant departure from the design originally proposed by Singlehurst and results in an increase in pressure sensitivity and a reduction in response to axial loading of the sensor superstructure. This design feature also has implications for packaging of the sensing mechanism as it yields a shorter sensing pod, improving overall device flexibility. A discussion of these effects is provided in more detail in the following section.

### 3.3.1. Governing Equations

Analysis of the sensing mechanism employed in this design begins with a schematic of the mechanism originally proposed by Singlehurst, which consists of a rigid anchor and diaphragm on either side of a grating, as shown in Figure 14. This represents the hydrodynamic pressure configuration.
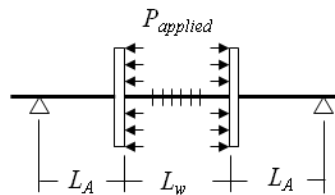


*Figure 14: Schematic of the sensing mechanism originally proposed by Singlehurst. Anchor points are indicated by triangles. FBG is represented by vertical gradient lines between the two rigid diaphragms.*

Anchor points are indicated by triangles in the figure and represent rigid connections between the optical fibre and the superstructure, considered the 'ground' for this analysis.

With applied hydrostatic pressure, the midpoint of the fibre span between the two rigid diaphragms undergoes zero displacement while the diaphragms translate along the axis of the fibre. This mechanism can be modelled using spring analysis, for which a schematic is provided in Figure 15.
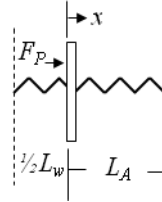


*Figure 15:  Spring analysis of sensing mechanism. Dotted line represents centreline between rigid diaphragms. Heavy vertical line at right indicates anchor.*

The length of the fibre section between the diaphragms is indicated by $L_w$, while the span from the inside face of the diaphragm to the anchor is represented by $L_A$. Force applied due to pressure is shown as *Fp,* while *x* represents displacement of the rigid diaphragm. The sections of optical fibre under consideration here are modelled as linear springs. Stiffness effects from the flexible silicone seal are ignored as the silicone's elastic modulus is orders of magnitude lower than that of the optical fibre, thus, the system stiffness is governed overwhelmingly by the fibre. The 'ground' is considered infinitely stiff for this analysis.

Force applied to the rigid diaphragm is related to the stiffness of the system, $k_{eff}$, and displacement of the diaphragm according to Hooke's Law:

$$F_p = k_{eff}\Delta x \qquad (3.1)$$

The effective stiffness of the system is governed by the two strained fibre sections: $L_A$ and $L_w$. For the orientation shown in Figure 15, the FBG-containing fibre section undergoes tension while the anchoring section experiences compression. The actions of

these two fibre sections can be modelled as springs acting in parallel, resulting in an effective stiffness calculated as

$$k_{eff} = \frac{2EA_F}{L_w} + \frac{EA_F}{L_A} \tag{3.2}$$

where $E$ is the elastic modulus of the optical fibre and $A_F$ is the cross sectional area of the fibre sections. From Equation 3.2, it is evident that if $L_w$ is small relative to $L_A$, then the system stiffness is governed by the first term of the equation and applied load is imparted primarily to the FBG-containing section of fibre. Likewise, if $L_A$ is small relative to $L_w$, then the effective stiffness is primarily a function of $L_A$ and the majority of applied load is carried by the anchoring sections of fibre.

Substituting the effective stiffness into Hooke's Law and rearranging $F_p$ in terms of applied pressure results in

$$PA_{dia} = \left(\frac{2EA_F}{L_w} + \frac{EA_F}{L_A}\right)\Delta x \tag{3.3}$$

where $A_{dia}$, is the area of the rigid diaphragm. In practice, the area that the applied pressure acts upon is slightly larger than the area of the rigid diaphragm as the total projected area includes the annular face of the flexible silicone. The difference in area is small, however, and has been ignored for this analysis. The projected area lost due to the optical fibre has also been disregarded. Displacement, $x$, is related to the change in length of the FBG section of optical fibre according to

$$\Delta x = \frac{1}{2}\Delta L_w \tag{3.4}$$

Substituting this into Equation 3.3 and solving for $\Delta L_w$ yields

$$\Delta L_w = \frac{2PA_{dia}}{EA_F \left(\frac{2}{L_w} + \frac{1}{L_A}\right)}$$

(3.5)

Strain within the FBG is the measurand of the sensing system and is determined from:

$$\varepsilon_{FBG} = \frac{\Delta L_w}{L_w}$$

(3.6)

Substituting this relationship into Equation 3.5, solving for strain and simplifying results in

$$\varepsilon_{FBG} = \frac{2PR_{dia}{}^2}{E\left(2 + R_{length}\right)}$$

(3.7)

where $R_{length}$ is the length ratio of the FBG-containing section of fibre to the anchored section of fibre, defined as

$$R_{length} = \frac{L_w}{L_A}$$

(3.8)

and $R_{dia}$ is the diameter ratio between the rigid diaphragms and the optical fibre:

$$R_{dia} = \frac{d_{diaphragm}}{d_{fibre}}$$

(3.9)

In this analysis, sensitivity is defined as wavelength shift per unit of applied pressure. Thus, by rearranging Equation 3.7 the sensitivity is determined as

$$\frac{\Delta\lambda}{P} = C\frac{2R_{dia}{}^2}{E\left(2 + R_{length}\right)}$$

(3.10)

where $C$ is a constant relating Bragg wavelength shift to strain; equal to 1.2 pm/$\mu\varepsilon$ for the gratings used in this application.

With Equation 3.10, theoretical sensitivity for the hydrodynamic pressure configuration can be determined for various design parameters.

### 3.3.2. Design Parameters and Sensitivity

From Equation 3.10, it is evident that pressure sensitivity is proportional to the square of the diameter ratio $R_{dia}$, and inversely proportional to the elastic modulus of the optical fibre $E$, and fibre length ratio $R_{length}$.

The overall diameter of the diaphragms is constrained by the maximum allowable outside diameter of the device; about 3 mm as per Table 1. Increasing the diaphragm diameter will increase sensitivity, but this parameter is limited by the internal diameter of the pod shell. Maximum sensitivity for a given outside sensor diameter is thus achieved by using thin-walled materials for the sensing pod. An annulus of about 50 μm is nominally allocated between the outside edge of the rigid diaphragm and the inside surface of pod. Accounting for wall thickness, this affords a maximum $d_{dia}$ of approximately 2.4 mm.

The elastic modulus of the optical fibre is a material property and generally cannot be altered. Plastic Optical Fibre (POF) has an elastic modulus an order of magnitude lower than silica-based fibre [40] and its use would result in an increase in sensitivity. However, POF is lossy [41], and more significantly has an outer diameter measured in hundreds of microns to millimeters [41]; too large for this application.

Alternatively, sensitivity can be increased by reducing the diameter of the optical fibre. The diameter of a standard 125 μm silica fibre can be reduced through chemical wet etching methods [42]. However, these techniques are involved and require the use of Hydrofluoric Acid (HF); a chemical preferably avoided. These techniques also leave the

optical fibre fragile prior to a suitable polyimide recoat, which complicates handling and sensor manufacture. It is therefore preferable to avoid chemical wet etching methods and instead use an intact version of the smallest diameter optical fibre commercially available. Fibre with a cladding diameter of 40 μm has been developed [43], but it is considered specialty fibre and its cost is significant. The smallest non-specialty fibre commercially available is 80 μm fibre, and therefore is the fibre employed in this design. This results in a diameter ratio, $R_{dia}$, of 30.

The final remaining variable influencing sensitivity is the fibre length ratio, $R_{length}$. As previously discussed, decreasing the length of the FBG-section of fibre relative to the anchoring section of fibre results in an increase in pressure sensitivity. The minimum length achievable for the FBG-section is dictated by grating length. In this case, the 1 mm FBGs necessitate a fibre span of approximately 2 mm to allow room for the epoxy anchors and general manufacturing tolerances. The remaining option is to increase the length of the anchoring-fibre sections, but this parameter is constrained by overall device flexibility. Specifically, increasing this length necessitates increasing the overall length of the rigid sensing pods, which in turn reduces the length of Nitinol$^{TM}$ tubing between them. The Nitinol$^{TM}$ tubing is responsible for providing device flexibility, so any reduction in tubing length is accompanied by a reduction in flexibility. In practice, it is preferable to maximize the length of the Nitinol$^{TM}$ tubing.

Theory indicates that the maximum sensitivity possible through manipulation of $R_{length}$ is achieved by placing the rigid fibre anchors at the midpoint between sensing pods (midpoint of Nitinol$^{TM}$ tubing), but this is not practical. Instead, the same effect can be achieved by eliminating the rigid anchor points altogether.

If all sensing pods are simultaneously exposed to the same hydrostatic pressure, then in the absence of rigid anchors the midpoints of the Nitinol™ tube are locations of zero fibre displacement due to the balance of forces from one sensing pod to the next, resulting in the same effective behaviour as if physical anchors existed. This yields an effective $R_{length}$ of 0.25, the lowest length ratio achievable for this sensor spacing and grating length.

The effect of these various parameters on pressure sensitivity is summarized in Figure 16.



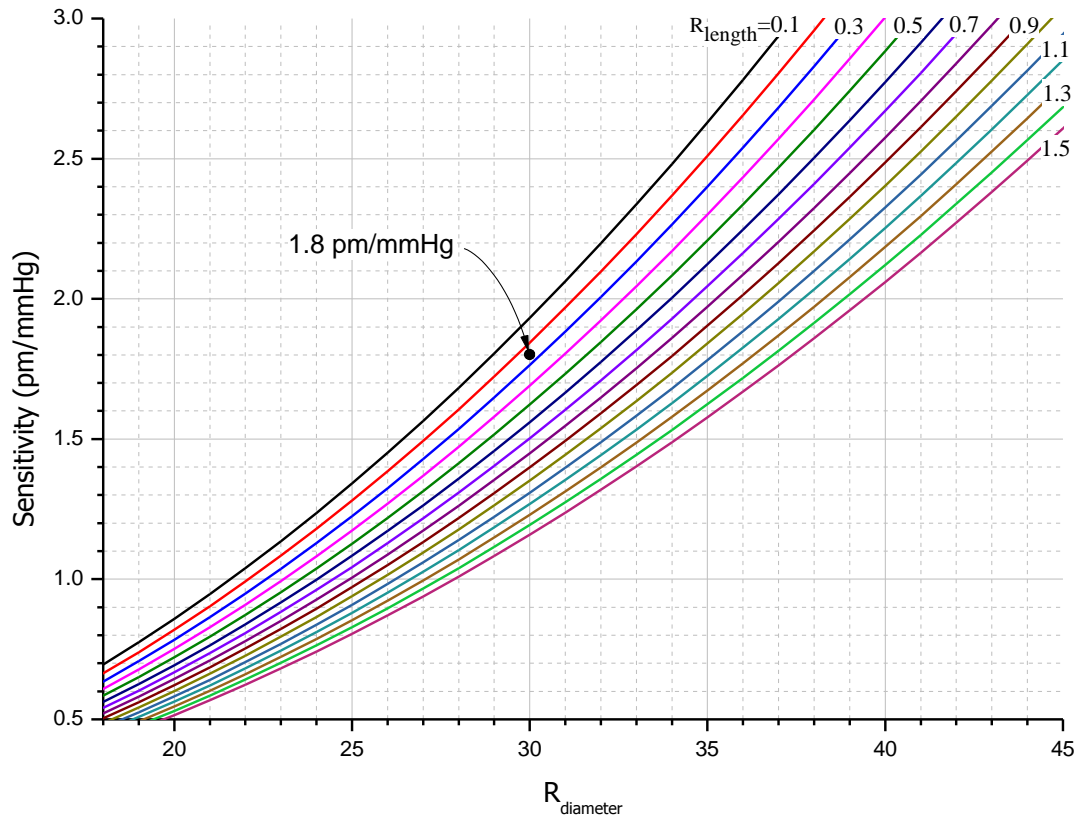*Figure 16:  Theoretical sensitivity for various dimensional configurations. $R_{length}$ is the length ratio of the FBG-containing fibre sections to the anchoring fibre sections. $R_{diameter}$ is the diameter ratio of the diaphragm to the optical fibre. This plot produced with an elastic modulus of 71 GPa for optical fibre. Theoretical sensitivity of this design is 1.8 pm/mmHg in the hydrodynamic pressure configuration.*

As indicated in Figure 16, the theoretical pressure sensitivity for this sensor design, based on the design parameters discussed, is approximately 1.8 pm/mmHg. In comparison, Voigt and Arkwright report pressure sensitivities of about 0.8 pm/mmHg and 1.0 pm/mmHg, respectively [19][16]. Additionally, Singlehurst's design when applied here complete with fixed anchors, yields a theoretical sensitivity of 1.3 pm/mmHg; 38% less than the sensitivity achieved by this design. It is clear that this design affords an improvement in sensitivity over comparable devices.

It should be noted that this analysis is applicable to the hydrodynamic-specific configuration of the sensor. The contact pressure-sensitive configuration will have reduced sensitivity due to the introduction of silicone and silicone gel to the sensing mechanism (items 10 and 11 of Figure 13). This reduction in sensitivity is attributed to the mechanical properties of the silicone. Specifically, the encapsulating silicone has a shear and a bending stiffness which will result in a reduction of force transmitted to the optical fibre for a given applied pressure.

This design is a significant departure from the original mechanism proposed by Singlehurst and has a number of implications. Apart from the improvement in pressure sensitivity, the absence of rigid anchors allows the length of the rigid sensing pods to be reduced, which contributes to improvement in overall flexibility of this sensor.

Additionally, the lack of rigid anchors results in a reduction in sensitivity to axial loading of the superstructure. When rigid anchor points are present, the fibre acts as a load path in conjunction with the superstructure. The elastic modulus of optical fibre is comparable to the materials of the superstructure, so its contribution to the overall effective stiffness of the device is considerable. This results in an appreciable proportion

of any applied axial load to be carried by the optical fibre, producing erroneous pressure readings. This affect is known to be significant in Singlehurst's device and suspected to be significant in Arkwright's.

As anchor points are absent in this design, the ability of the superstructure to load the fibre array is reduced and axial load sharing between the optical fibre and the metal superstructure is minimized. Though not quantified in this analysis, the fibre is largely removed as a load path, which results in a significant reduction in axial loading response.

The trade-off for these improvements in sensitivity, flexibility and improved immunity to axial loading is mechanical crosstalk.

### 3.3.3. Sensor Crosstalk

In the absence of rigid anchors, fibre displacements from a given pod are communicated to adjacent pods via the optical fibre, resulting in strain of adjacent gratings. This produces erroneous pressure indications in adjacent pods.

Assuming small displacements, the assembly of annular silicone seals and optical fibre can be approximated as a system of linear springs. The assumption of small displacement is valid for the specified operating range of the sensor system. Consequently, the spurious strain communicated from one pod to the next can be approximated as being linearly proportional to the strain within the source pod, allowing the influence of crosstalk to be corrected.

Analysis of this crosstalk correction method begins with a given sensor array of N sensing pods, as shown in Figure 17.
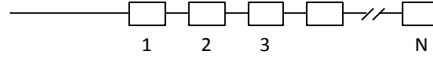
*Figure 17:   Crosstalk correction of array with N sensing pods*

Assuming each pod is individually subjected to an arbitrary pressure, the measured strain across a given FBG will contain information concerning the pressure applied directly to the pod, in addition to the pressure applied to the other pods. The strain due only to a given pod's applied pressure can then be established through superposition by including a correction factor for each of the remaining pods, expressed as

$$\varepsilon_n = \varepsilon_{n,meas} - \sum_{j=1,j\neq n}^{N} \delta_{n,j}\,\varepsilon_j \tag{3.11}$$

where $\varepsilon_n$ is the strain at sensor pod $n$ due only to applied pressure, $\varepsilon_{n,meas}$ is the strain measured by the interrogation system at sensor pod $n$ which includes the confounding influences of other pods, $\delta_{n,j}$ is the strain influence on pod $n$ due to pressure applied to pod $j$, and $\varepsilon_j$ is the strain on the $j$'th pod due to pressure applied to pod $j$.

Expanding this equation and solving for known quantity $\varepsilon_{n,meas}$ results in:

$$\varepsilon_{1,meas} = \varepsilon_1 + \delta_{12}\varepsilon_2 + \delta_{13}\varepsilon_3 + \cdots + \delta_{1N}\varepsilon_N$$
$$\varepsilon_{2,meas} = \delta_{21}\varepsilon_1 + \varepsilon_2 + \delta_{23}\varepsilon_3 + \cdots + \delta_{2N}\varepsilon_N$$
$$\varepsilon_{3,meas} = \delta_{31}\varepsilon_1 + \delta_{32}\varepsilon_2 + \varepsilon_2 + \cdots + \delta_{3N}\varepsilon_N$$
$$\vdots$$
$$\varepsilon_{N,meas} = \delta_{N1}\varepsilon_1 + \delta_{N2}\varepsilon_2 + \delta_{N3}\varepsilon_{3_2} + \cdots + \varepsilon_N$$

These equations can be represented in matrix form:

$$[\varepsilon]_{meas} = [\delta][\varepsilon]$$

where $[\varepsilon]_{meas}$ is an array of the measured strain values for gratings 1 to N, $[\delta]$ is the correction coefficient matrix and $[\varepsilon]$ is the array of strain values due only to individually applied pressures. Solving for the values of interest $[\varepsilon]$, results in

$$[\varepsilon] = [\delta]^{-1}[\varepsilon]_{meas} \tag{3.12}$$

where

$$[\varepsilon] = \begin{bmatrix} \varepsilon_1 \\ \varepsilon_2 \\ \varepsilon_3 \\ \vdots \\ \varepsilon_N \end{bmatrix}$$

$$[\varepsilon]_{meas} = \begin{bmatrix} \varepsilon_{1,meas} \\ \varepsilon_{2,meas} \\ \varepsilon_{3,meas} \\ \vdots \\ \varepsilon_{N,meas} \end{bmatrix}$$

$$[\delta] = \begin{bmatrix} 1 & \delta_{1,2} & \delta_{1,3} & \cdots & \delta_{1,N} \\ \delta_{2,1} & 1 & \delta_{2,3} & \cdots & \delta_{2,N} \\ \delta_{3,1} & \delta_{3,2} & 1 & \cdots & \vdots \\ \vdots & & & \ddots & \\ \delta_{N,1} & \delta_{N,2} & \delta_{N,3} & \cdots & 1 \end{bmatrix}$$

Thus, the influence of mechanical crosstalk can be negated by multiplying a given array of measured strains by the inverse of the correction matrix $[\delta]$.

The correction matrix is determined as part of calibration prior to sensor use. The matrix is populated with correction coefficients by individually pressuring each sensing pod and recording the resulting strain in all other pods, then normalizing the resulting strains against the strain measured in the pressurized pod; repeated for all pods.

### 3.4. Sensor Pressure Specificity

A key strength of this design is the ability to selectively sensitize individual sensing pods to particular pressure phenomenon; either hydrodynamic or hydrodynamic and contact pressure. This flexibility affords a variety of novel sensing schemes not possible with existing manometric devices.

For example, one configuration possible is to sensitize the five or so most proximal and distal pods to contact (and hydrodynamic) pressure while the remaining pods in the middle of the device are sensitized to only hydrodynamic pressures. This configuration has the potential to provide information regarding both sphincter function (such as relaxation of both the LES and UES) and a direct measurement of bolus transit within the esophageal body. This is a sensing scheme not possible with existing HRM devices alone.

Alternatively, all sensing pods may be sensitized to contact pressures, in which case the device will function as a typical HRM system.

An additional option is to sensitize every second pod to hydrodynamic pressure with the remaining pods sensitized to contact pressure, yielding a pattern of alternating pressure-specific pods. This may provide measurement of esophageal occlusion pressure and intrabolus pressure semi-continuously (at a spacing of 20 mm) throughout the length of the esophagus. Such a configuration is expected to be capable of simultaneously discerning indicators suggesting DES and separately, indicators of a large spatial gap between peristaltic wave transitions in the mid-esophagus; an additional sensing scheme not possible with existing HRM devices alone.

Finally, sensitizing all pods to hydrodynamic pressure may provide information concerning bolus transit through the entire length of the esophagus, including passage through both the UES and the LES, which may provide new opportunity for study of bolus transit mechanics.

## 3.5. Summary

This design provides the ability to selectively sensitize individual pods to either hydrodynamic pressure, or contact and hydrodynamic pressure. In either configuration, the fundamental opto-mechanical sensing mechanism is the same: applied pressure works to axially strain a section of fibre which contains an FBG. In the case of the hydrodynamic configuration, this is achieved by allowing the pressurized fluid to act directly on the rigid diaphragms. In the case of the contact-sensitive configuration, applied pressure compresses the ultra-soft silicone gel contained inside the sensing pod, which then expands axially and strains the fibre.

The lack of rigid anchors securing the optical fibre to the superstructure is a novel departure from the design proposed by Singlehurst and results in pressure sensitivity higher than comparable designs, as well as a theoretical reduction in axial loading sensitivity and bending sensitivity.

The trade-off for these improvements is the introduction of mechanical crosstalk, though a method to correct for this crosstalk has been developed.

In conclusion, the ability to selectively sensitize individual pods to different pressure phenomena affords the ability to employ novel sensing schemes not possible with existing HRM devices alone.

# Chapter 4

## 4. Sensor Fabrication

To confirm design function and performance, this work has included fabrication and testing of prototype sensors. This chapter provides discussion of the materials and methodology used to construct these prototypes.

### 4.1. Material Selection and Machining of Parts

A prototype sensor is fabricated from a variety of medical grade materials including epoxies, silicone elastomers, stainless steel, and Nitinol$^{TM}$. The materials and components used in the prototypes are listed in Table 2.

*Table 2: List, description and source of sensor prototype fabrication components*

| Item | Name | Description | Source |
|------|------|-------------|--------|
| 1 | Optical Fibre | 80 μm, single mode; polyimide coated. | ITF Labs; Montreal, QC |
| 2 | Rigid diaphragm | Stainless steel washer; 2400 μm OD, 210 μm ID, 130 μm THK. | Laser cut from 0.005" SS shim stock |
| 3 | Silicone seal | Annular silicone seal of MED1-4013 silicone adhesive; medical grade. | NuSil Technology; Carpinteria, CA |
| 4 | Pod housing | 2.9 mm long, 2.8 mm OD, 2.5 mm ID; Holes 2x1 mm. | Laser cut from 12 gage thin wall hypodermic SS tube |
| 5 | Capping washer | Stainless steel washer; 2800 μm OD, 410 μm ID, 250 μm THK. | Laser cut from 0.010" SS shim stock |
| 6 | Nitinol$^{TM}$ Tube | 7.08 mm long, JM-83088. 378.5 μm OD, 254 μm ID. | Johnson Matthey; West Chester, PA |
| 7 | Epoxy anchor | Loctite$^{TM}$ Hysol M-31CL medical grade epoxy | Henkel; Mississauga, ON |
| 8 | Sealing silicone | MED1-4013 silicone adhesive; medical grade. | NuSil Technology; Carpinteria, CA |
| 9 | Solder connection | Indalloy® #121; 96.5Sn-3.5Ag with flux #3; Lead free solder. | Indium Corporation; Clinton, NY |
| 10 | Encapsulating silicone | MED-6010 high durometer silicone elastomer; medical grade. | NuSil Technology; Carpinteria, CA |
| 11[*] | Ultra-soft silicone potting gel | MED-6345 high penetration tacky silicone gel; medical grade. | NuSil Technology; Carpinteria, CA |
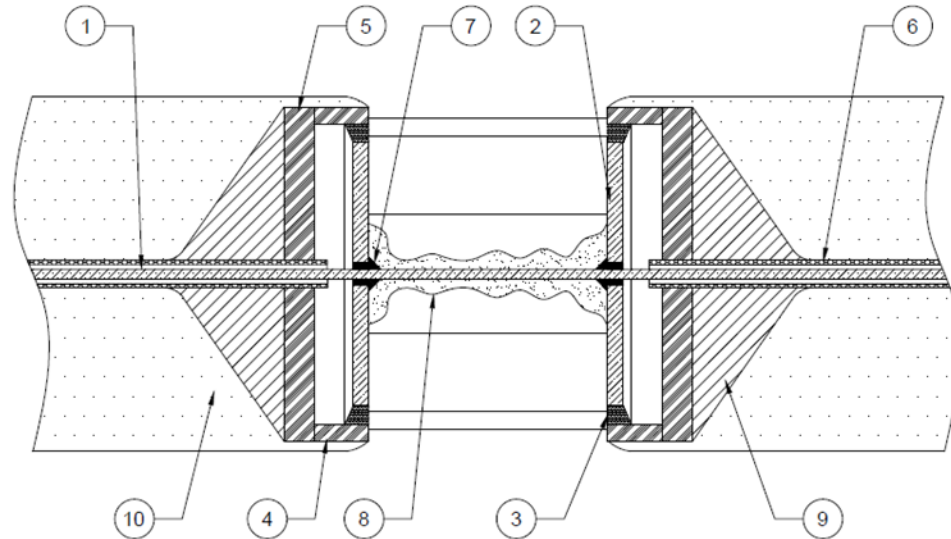


*\* Specific to contact pressure configuration. Not shown in this image. Refer to Figure 13*

The two flat stainless steel components, the rigid diaphragms and capping washers

(indicated as items (2) and (5) in the table), are laser-cut from stainless steel shim stock

using a femtosecond laser. Pieces of shim stock are secured to glass slides mounted under the optics of the laser and a purpose-coded laser trajectory is then executed to conduct the automated cutting process. The resulting parts are then cleaned and degreased with acetone in an ultrasonic bath.

Machining of the pod housing (item 4) is more involved. For this purpose, a mechanical rotator has been designed and fabricated to precisely hold sections of stock hypodermic tubing under the optics of the femtosecond laser, shown in Figure 18.
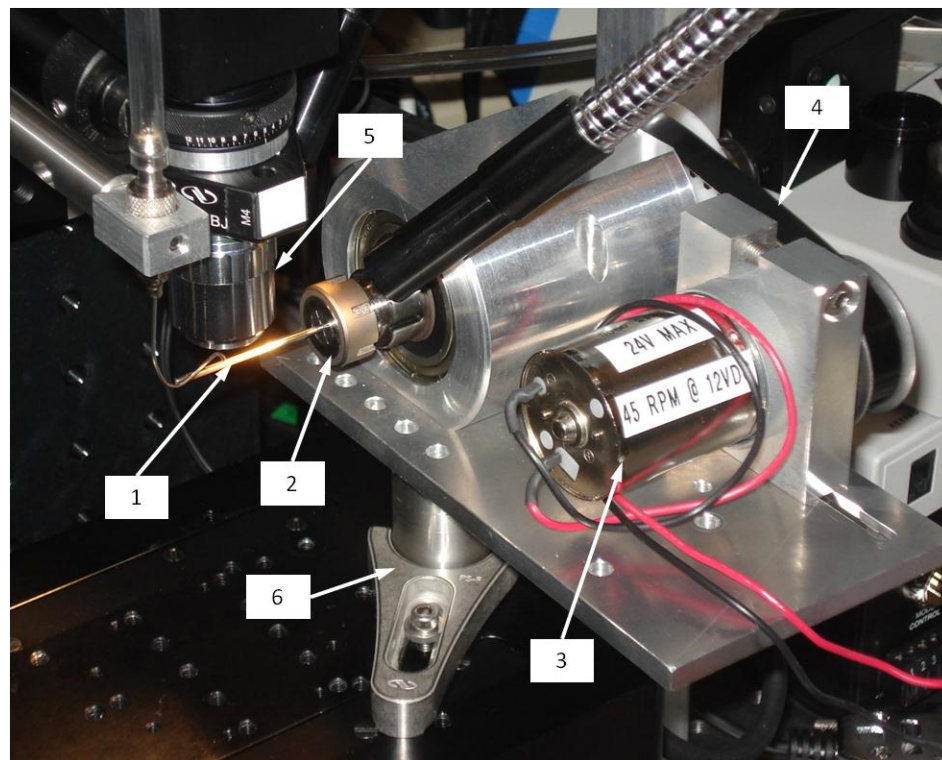


*Figure 18:  Laser machining of the sensing pod body with the purpose-built precision rotator*
*Components: (1) workpiece, (2) precision chuck, (3) drive motor, (4) drive belt, (5) laser*
*objective, (6) mounting fork to 3-axis stage*

The mechanical rotator consists of a precision micro-milling chuck (2) mounted into two bearings, belt driven (4) by a gear motor (3). Rotator speed is controlled by the voltage supplied to the drive motor. The chuck utilizes an exchangeable collet system

capable of precisely holding stock tubing sizes ranging from 0.255 mm to 5 mm. The entire rotator assembly is mounted to a 3-axis stage with a mounting fork (6).

This precision rotator mounted to the three-axis stage allows automated movement of the workpiece in the three primary directions, and continuous or intermittent rotation about the axis of the workpiece. Runout at the collet has been measured to be on the order of microns.

The pod housings of the sensor are cut from lengths of hypodermic tubing. The rectangular sensing ports of the pod housing are cut first by holding the hypodermic tube fixed and lasing a rectangular trajectory on the top surface of the workpiece. A series of multiple ports are cut along the length of the tube to batch-produce pods. The rotator is then rotated $90^{o}$ and the process repeated; continuing until ports are cut at $90^{o}$ intervals around the circumference of the tube.

To cut the individual pods from the stock, the hypodermic tube is continuously rotated while the focal point of the laser is translated down the cut plane of the tube, perpendicular to the tube axis. This method is similar to the cut-off techniques of mechanical lathes and effectively acts as a laser-lathe. These highly-automated laser-based techniques are able to repeatedly produce high quality components.

After cutting, the pods are cleaned and degreased with acetone in an ultrasonic bath.

## 4.2. Assembly Method

The mechanical sensor package consists of two unit-repeating sub-assemblies. These sub-assemblies are fabricated separately and then mated together prior to inserting and securing an optical fibre. As shown in Figure 19, the first sub-assembly consists of the

pod housing (4), rigid diaphragms (2), and annular silicone seals (3), while the second sub-assembly consists of capping washers (5), solder (9) and lengths of Nitinol$^{TM}$ tubing (6).
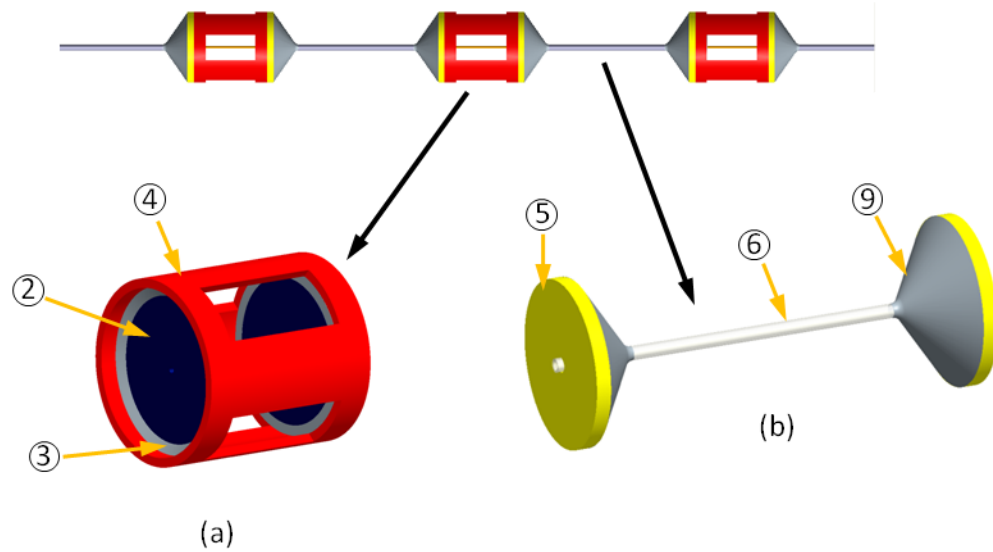


*Figure 19:  Sensor sub-assemblies. Sub-assembly (a) components: (2) rigid diaphragms, (3) silicone seals, and (4) pod housing. Sub-assembly (b) components: (6) Nitinol$^{TM}$ tubing, (5) capping washers, and (9) solder. Numbered items correspond to Table 2.*

To fabricate the first sub-assembly, identified as (a) in Figure 19, two purpose-built jigs are used, described in Figure 20.
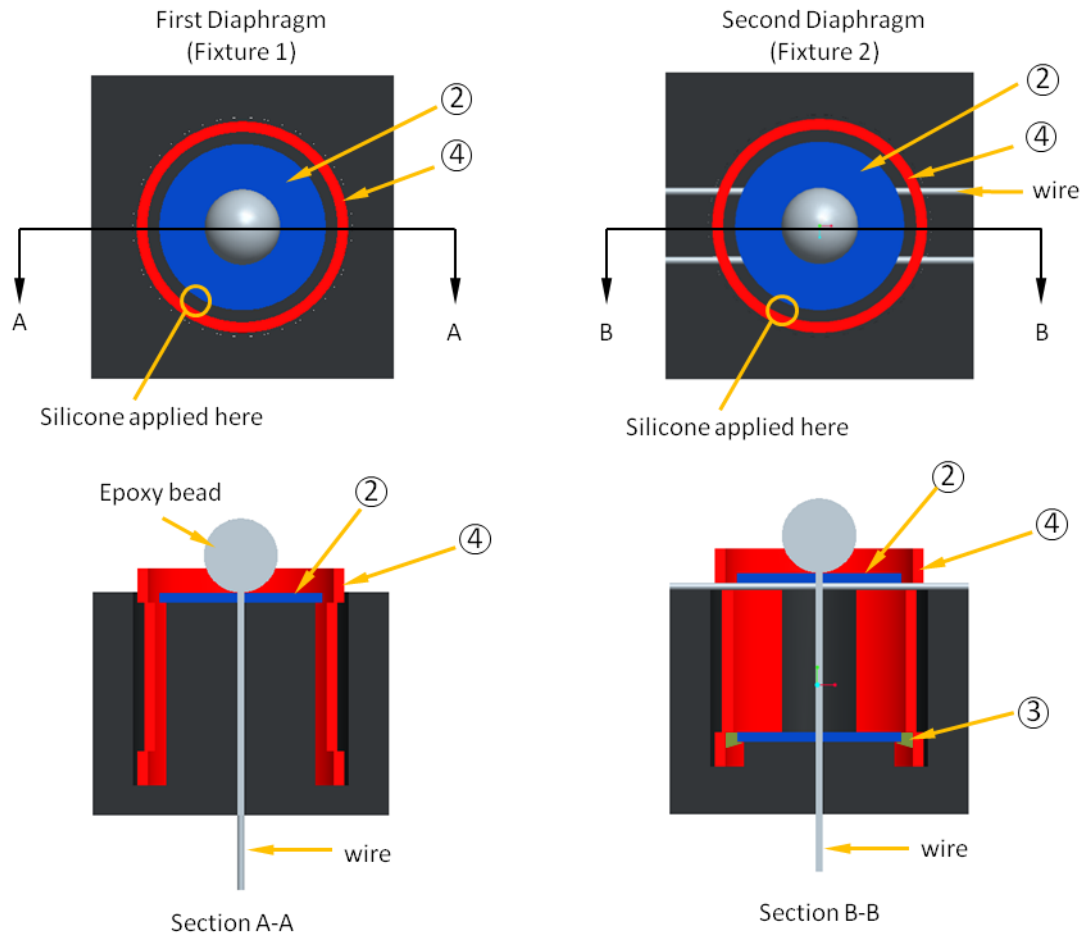
*Figure 20: Jigs used in construction of first pod sub-assembly. Left: installation of first diaphragm. Right: installation of second diaphragm. Numbered items as per Figure 19.*

To install the first diaphragm (diaphragms are indicated as item 2 in Figure 20), Fixture 1 holds a diaphragm at the correct elevation within an upright pod housing (4). A length of wire with an epoxy bead at the end is threaded through the central hole of the diaphragm and secures it to the jig. The wire also acts to ensure that the diaphragm remains concentric within the pod housing. Silicone is injected from the top of the assembly using a 25 gauge needle to continually fill the annulus. The entire fixture and assembly is then heated to cure the silicone, completing installation of the first diaphragm.

The sub-assembly, which at this point consists of one rigid diaphragm and pod housing, is then re-oriented and fixed in the second purpose-built jig (Fixture 2) such that the previously installed diaphragm is at the bottom of the pod housing. In this fixture, the pod housing is again held upright and two wires are passed horizontally through the rectangular sensing ports to support a second rigid diaphragm, as shown in the figure. Again, wire with an epoxy bead secures the diaphragm to the fixture and silicone is injected into the annulus with a 25 gauge syringe, followed by a heat-cure. This completes installation of the second diaphragm and thus fabrication of the first sub-assembly.

To fabricate the second sub-assembly, identified as (b) in Figure 19, two capping washers are threaded onto a piece of Nitinol$^{TM}$ tubing with excess length, as indicated in Figure 21.
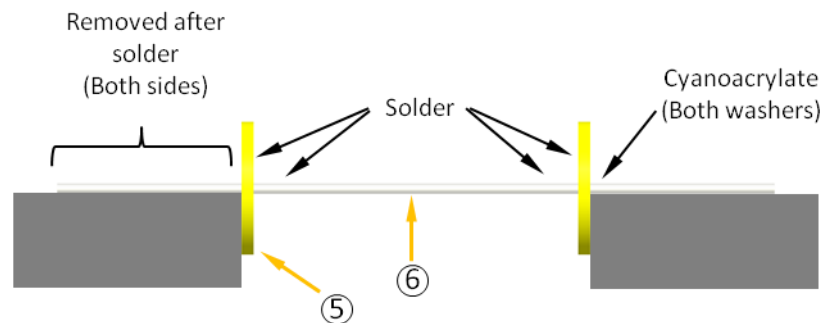


*Figure 21: Fabrication of second sub-assembly (sub-assembly (b) from Figure 19). Numbered items are as per Figure 19.*

The Nitinol$^{TM}$ tubing, identified as item 6 in the figure, is mechanically abraded beforehand to remove the protective titanium oxide surface layer and promote solder wetting. The capping washers (5) are also mechanically abraded to promote solder adhesion. The tubing is spanned across an open gap with a width corresponding to the appropriate face-to-face dimension of the capping washers.

The capping washers, supported by the excess length of tubing, are pressed flush to the vertical walls on either side of the gap and fixed in place with cyanoacrylate. This is done to ensure that the face-to-face distance of the capping washers is dimensionally correct and that the washers remain parallel during soldering. Care is taken to ensure that the cyanoacrylate is applied only to the outside faces of the capping washers, away from the soldering surface. Flux is liberally applied to the washer-tube interface and the connection is soldered.

Discussions with suppliers of Nitinol$^{TM}$ products have indicated that joining Nitinol$^{TM}$ to stainless steel is a common challenge in industry. The two materials cannot be satisfactorily joined by welding and to solder them requires specialized solder in conjunction with an aggressive flux. Attempts by this author to join these materials with epoxy have not produced acceptable results. It is for these reasons that speciality Sn-AG solder is used with flux #3, described in more detail in Table 2 (item 9).

After soldering, the joints are mechanically scrubbed to remove residual flux and the cyanoacrylate is dissolved with acetone, releasing the sub-assembly. Completion of this sub-assembly is then achieved by grinding off the excess tubing and cleaning the assembly in an ultrasonic bath with acetone.

Following fabrication of multiple copies of the two sub-assemblies, components are threaded onto a length of 35 gauge polyimide tubing with adjacent parts pressed flush. These components are then placed in a fixture which contains a groove of the appropriate width to hold the assembly straight, as shown in Figure 22.
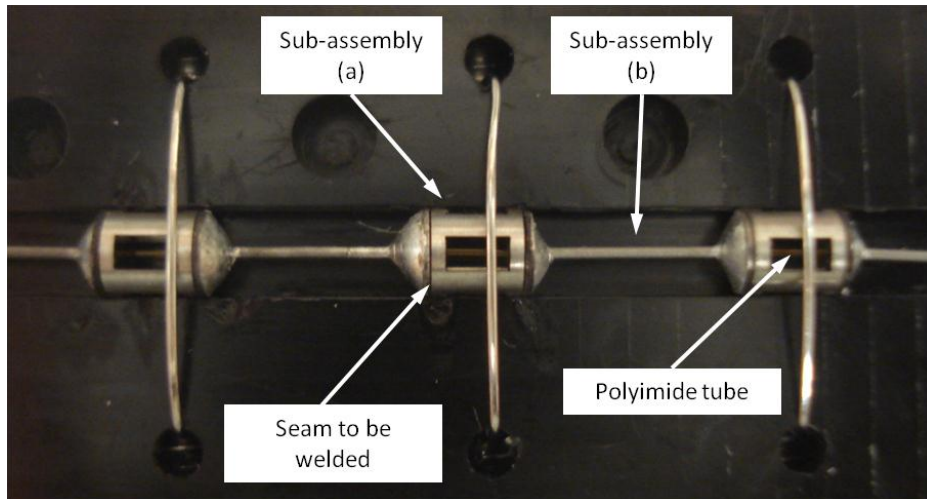
*Figure 22: Fixture used for laser welding. Components secured with bailing wire. Polyimide tube can be seen through the sensing ports. Laser welding is used to create a continuous seam around the locations indicated above.*

The components are lashed down with small diameter bailing wire, allowing the entire assembly to be handled. Each sub-assembly is then bonded to the next via laser welding. Specifically, mating lines between the capping washers and pod housings are bonded by continuous butt-welds around the circumference of the pods. With the components secured in the jig, welding commences at seam locations accessible to the laser welder. When all exposed seam sections are joined, the bailing wire is removed and the partially-welded sensor is extracted from the jig. The remaining un-welded seam sections are then joined by holding the sensor structure by hand under the laser welder, completing the welding. This results in a robust, flexible, metallic superstructure that can be safely handled without risk of damage to the superstructure.

To complete the sensor, the assembled superstructure is held fixed and an optical fibre is inserted into one end of the polyimide tube. The fibre is located within the superstructure such that the FBGs are at the midpoint of the sensing ports, between the rigid diaphragms. The fibre is then held in place while the polyimide tube is withdrawn

from the distal end of the assembly, leaving a correctly located optical fibre running the length of the superstructure. The fibre is then secured to the rigid diaphragms with epoxy applied via a pick passed through the sensing ports (indicated as item 7 in Table 2). Care is taken to ensure that epoxy is only applied to regions of the fibre that do not contain an FBG. The structure is then left to cure for 24 hrs, followed by a post-cure heat cycle. Sealing silicone (item 8 in Table 2) is then applied to the exposed fibre and epoxy within the pod housing with a wire pick, followed by heat curing. This completes the base sensing structure of the device.

At this stage, the sensor array is sensitive only to hydrodynamic pressure and encasing it entirely with silicone (with the exception of the sensing ports) would complete the sensing device.

To sensitize the pods to contact pressure, short lengths of heat shrink tubing, each with a single hole cut in the side, are secured over the sensing pods such that each hole aligns with one of the sensing ports, effectively creating a sealed chamber with one open port through which silicone gel is injected (item 11 in Table 2). The silicone gel is cured with a heat cycle. The heat shrink jacket is then removed, leaving behind a filled (potted) sensing pod. Encasing this assembly entirely in silicone would complete this sensor configuration.

For prototype testing conducted in this work, the contact-sensitized pods are dip-coated with encapsulating silicone to produce sensing pods functionally identical a continuously-encapsulated design. Hydrodynamic sensitive pods are left unencapsulated as silicone encapsulation has no functional effect in such a configuration.

## 4.3. Summary

The stainless steel components of the prototype devices are produced with highly automated femtosecond laser cutting techniques and are assembled using purpose-built jigs. With appropriate control of tolerances, the methods discussed here may be applied to produce sensor arrays of arbitrary length.

A key strength of these methods is that the majority of sensor fabrication work is done in the absence of an optical fibre. This is beneficial as optical fibres are fragile and mistakes during assembly can break them.

In summary, these manufacturing methods are reliable and are able to repeatedly produce identical prototype sensors. These methods have been used to construct prototype sensors for bench top testing.

# Chapter 5

## 5. Testing Methodology

To demonstrate the sensing principle and performance of the sensor design, two sensor prototypes were fabricated using the assembly methods described in Section 4. Prototypes constructed included a three-pod sensor with one Bragg grating (located in the middle pod) and a more advanced three-pod prototype with three gratings. With the exception of grating count, the multiple sensor prototypes were identical. A typical completed prototype is shown in Figure 23.
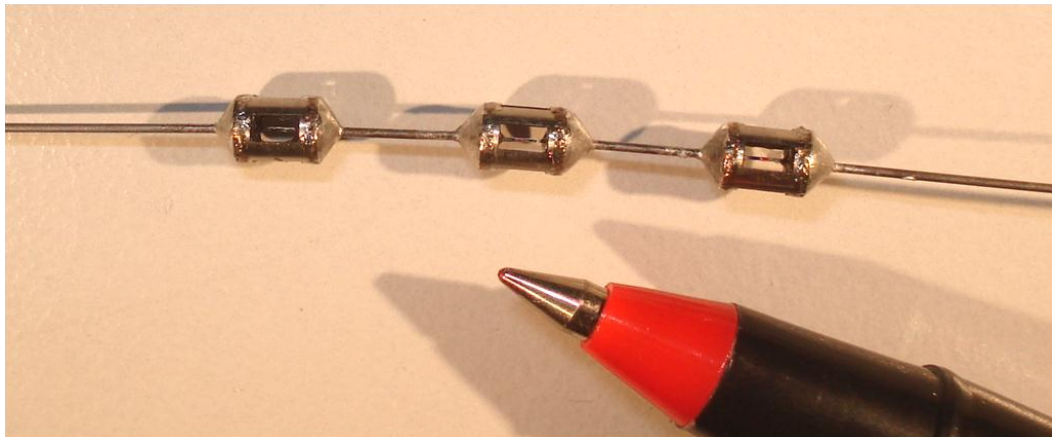


*Figure 23:   Typical three-pod prototype in hydrodynamic configuration. Shown here is a three-grating sensor; indistinguishable from the single-grating variant.*

Investigation of these fabricated prototypes included tests to determine pressure sensitivity, demonstration of insensitivity to contact pressure, bending sensitivity, temperature sensitivity, axial load sensitivity and crosstalk characterization (in the case of the three-grating sensor only). These tests were conducted with all sensing pods of the two prototypes in the hydrodynamic pressure-specific configuration; hereby referred to as the hydrodynamic configuration.

After testing in the hydrodynamic configuration, the three-grating sensor prototype was reconfigured to be sensitive to contact pressure; hereby referred to as the contact pressure configuration. Further testing of this prototype included a repeated pressure and temperature sensitivity test, as per the sensor in the hydrodynamic configuration prior, and additionally a demonstration of sensitivity to contact pressure.

At the time of this work, the described TDM interrogation system was unsuitable for testing purposes, thus all methods described here were conducted using a standalone commercially available WDM interrogator unit (SmartScan, SmartFibres Ltd. Bracknell, UK) with purpose-built custom LabView$^©$ code. Gratings used in the three-pod sensor prototype had Bragg reflections centred at unique wavelengths, as per WDM requirements.

This interrogation unit has a base operating frequency of 2.5 KHz. Real-time boxcar averaging was employed during data collection for all tests which resulted in an effective interrogation frequency of 60 Hz. The custom LabView$^©$ code continuously displayed real-time readings and provided data collection abilities through either logging single points on command or using a continuous logging mode.

Methodology used for each test is described below.

## 5.1. Testing with Hydrodynamic Pressure Configuration:

### 5.1.1. Pressure Sensitivity

Pressure sensitivity was determined by placing the prototype sensor in a purpose-built pressure manifold and incrementally increasing the hydrostatic pressure. Secured to the proximal-most length of Nitinol$^{TM}$ tube on all sensors was a Luer-Lok$^®$ connector such

that the three pods of the sensor array could be inserted and sealed with a mating Luer-Lok® on the pressure manifold, as indicated in Figure 24. The system was configured such that the working fluid, room temperature water, could be flushed in either direction to remove entrapped air using the flushing port and reservoir.
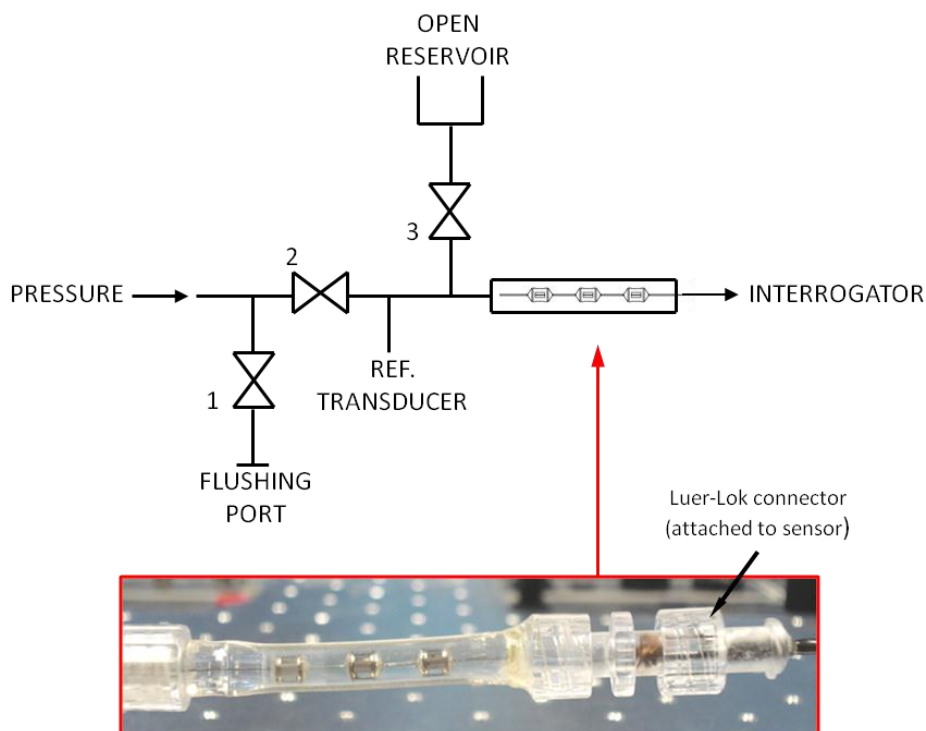


*Figure 24:  Pressure manifold schematic. Luer-Lok® anchored to sensor array via epoxy (shown darkened within).*

Hydrostatic pressure was applied via a mechanical screw-driven syringe connected to the pressure manifold with a length of Tygon$^{TM}$ tubing. A pressure transducer (Omega© PX01K1-010G5T, 0-10psig, ±0.05%FSO, Omega Engineering Inc., Stamford, CT) was connected to the manifold to provide reference pressure values. Data was simultaneously read from the pressure transducer and interrogator at 60 Hz using the LabView© code previously described.

Measurements were logged as follows:

1. Reference pressure transducer and sensor wavelength readings were zeroed by opening Valve 3 on the manifold and equalizing with ambient pressure. Baseline readings were logged and Valve 3 was closed.

2. Pressure was increased by approximately 15 mmHg via the screw-driven syringe and Valve 2 (the isolation valve) was then quickly closed.

3. When readings stabilized, usually within 3 seconds, pressure and wavelength points were logged from the reference gauge and interrogator, respectively.

4. The isolation valve was then opened again and Steps 2-4 repeated.

Pressure was varied from atmospheric to approximately 400 mmHg, more than covering the operating range of a typical esophageal manometer. Sensitivity was determined with post-processing using linear regression of the recorded Bragg wavelength shifts versus reference pressure data for each grating using Microsoft Excel (2007).

### 5.1.2. Demonstration of Insensitivity to Contact Pressure

To confirm the insensitivity of the sensor to contact pressures while in the hydrodynamic configuration, a device with the ability to apply contact pressure to the sensing pods was constructed. This contact pressure-applying device consisted of a flexible latex rubber tube, open to atmosphere at either end, spanning the length of a clear plastic pressure manifold, as shown in Figure 25.
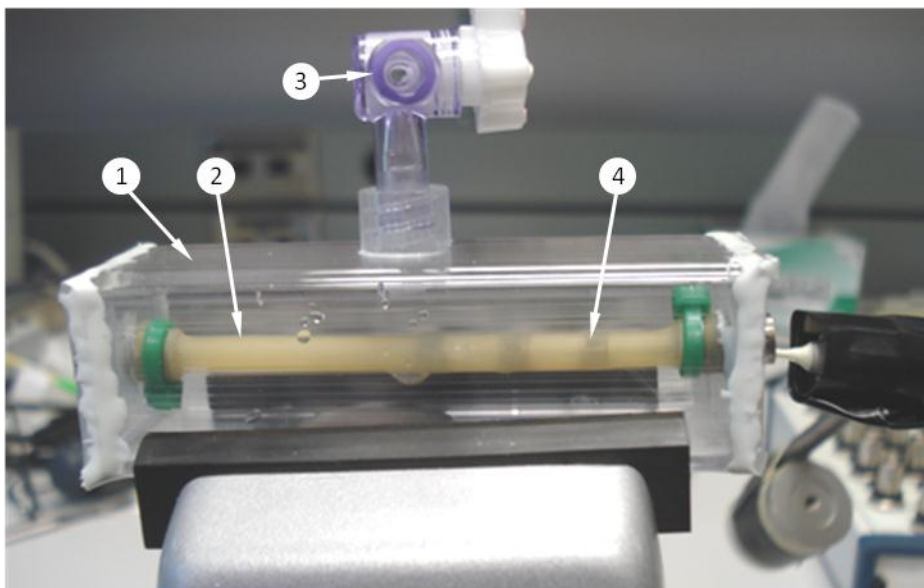
*Figure 25:   Contact pressure-applying device held fixed in a vice. Sensor array is visible within rubber tube exiting on the right hand side of the device. Components: (1) Pressure manifold, (2) Rubber tubing, (3) Valve, (4) Sensor pod (within the rubber tube).*

Contact pressure was applied to the sensing pods (indicated as item 4 in Figure 25) by inserting the sensor into the interior of rubber tube (2) and increasing the pressure within the manifold (1) through a syringe connected to a three-way valve on the top surface of the device (3). The pressure transducer previously described was connected to the system to provide a reference pressure within the manifold.

The operating principle of the device is that the manifold pressure acts on the outside surface of the rubber tube, which in turn applies an axially-symmetric 'occlusion pressure' to the sensor within the tube.

The test was conducted by supplying the manifold with an arbitrary pressure waveform generated by manually pumping the attached syringe. Data were recorded continuously using the custom LabView[©] previously described, which generated a series of Bragg wavelength shifts and manifold pressure as a function of time.

### 5.1.3. Device Flexibility and Bending Response

Investigation of sensor bending had two objectives: to non-destructively establish the overall flexibility of the device and to determine its sensitivity to bending.

Establishment of sensor flexibility was achieved through a flexibility test. To conduct the test, the sensor prototype was mechanically wrapped by hand around various cylindrical objects of incrementally decreasing diameters. The device was considered to be at its bend radius limit when buckling or any other permanent deformation to the sensor was considered imminent, determined subjectively by monitoring the device's resistance to bending.

To establish the influence of bending on wavelength shift (or indicated pressure), the sensor was subjected to a three-point bend test. A schematic of this test is shown in Figure 26.
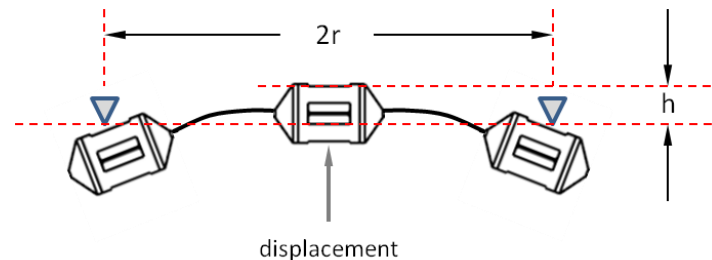


*Figure 26: Three point bend test schematic. Shaded triangles indicated pivot points of proximal and distal sensing pods. Zero displacement corresponds to a straight sensor.*

To conduct the test, the distal and proximal sensing pods were held fixed against two small diameter screws and allowed to pivot and translate as the middle pod was mechanically displaced in-plane using a rod secured to a micrometer-driven three-axis stage. The middle pod was incrementally displaced from straight ($h = 0$) to a displacement matching the limiting radius of curvature determined in the previous flexibility test.

Approximation of the radius of curvature as a function of displacement, *h*, was achieved using a spherometer equation. Given a circle with measurements *h* and *r,* as indicated in Figure 27 (and corresponding to the parameters in Figure 26),
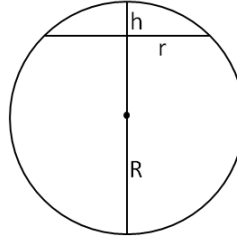


*Figure 27:  Three point bend test schematic to determine bend radius. Variables shown here correspond to parameters in Figure 26.*

the radius of curvature, *R*, can be estimated with

$$R = \frac{r^2}{2h} + \frac{h}{2}$$
(5.1 )

The spherometer equation as applied in this scenario provides the radius of curvature of the outside edge of the sensor. Internal or 'wrapping' radius is thus determined by subtracting the diameter of the sensing pods from Equation 5.1, yielding a radius of curvature directly comparable to the radius of the flexibility test.

The wavelength shift was logged using the custom LabView[©] code previously described and displacement was measured by manually reading the micrometer. The measurements were logged at each displacement increment. Post-processing of the data was conducted with Microsoft Excel (2007). The measured wavelength shifts were divided by the previously established sensitivity of each sensing pod to generate a data series of 'indicated pressure' versus radius of curvature.

### 5.1.4. Temperature Sensitivity

To determine temperature sensitivity, the sensor array was held fixed in a water-filled 80 ml beaker placed in a programmable oven. Reference temperature was determined using a resistance temperature device (Omega© DRF-RTD, 0-100$^o$C, 0.1%F.S Stamford, CT) with a probe tip located adjacent to the sensor pods immersed in the water bath. The purpose of the water bath was to reduce the dead-band effect of the oven temperature controller and to help stabilize temperature readings. Care was taken to ensure that the probe tip remained in close proximity to the sensing pods and that both items were located in centre of the beaker. The water bath was given time to settle after initial setup to ensure that water within the bath was motionless prior to testing.

Oven temperature was incrementally adjusted from approximately 30$^o$C to 40$^o$C in steps of 2$^o$C, more than spanning typical human body temperature. Wavelength and temperature readings were logged at each temperature increment when it was determined that steady-state temperature had been achieved, indicated by approximately flat lines on both temperature and wavelength live readings.

Temperature sensitivity was determined using linear regression of the wavelength shift versus temperature data series produced. Wavelength shift was converted in post-processing to 'indicated pressure' versus temperature by dividing the wavelength shift values by the sensitivity of the sensor previously established.

### 5.1.5. Axial Load Sensitivity

To determine the sensitivity of the sensor to axial loading, the prototype was held vertical and fixed at the proximal-most section of Nitinol$^{TM}$ tube. Load was applied to the distal-most Nitinol$^{TM}$ tube to ensure that the applied load spanned multiple sensor pods.

Load was applied by free-hanging incrementally increasing masses from a clamping mechanism that mechanically gripped the distal tubing. Care was taken to ensure that wavelength shift readings were taken only when the hanging masses had stopped swinging. This was indicated by visual inspection of the assembly and monitoring the live wavelength information display provided by the LabView$^{©}$ code.

Mass applied ranged from 0 to 250 grams. Applied load was calculated by multiplying the mass, including the clamping mechanism, by the gravitational acceleration constant (9.81 m/s$^2$). Post-processing was used to convert the logged wavelength shifts to 'indicated pressure' and linear regression was employed to determine its relationship to applied load.

## 5.1.6. Crosstalk Characterization and Correction

To characterize the mechanical crosstalk between pods, a system was assembled such that individual sensing pods could be pressurized. The system consisted of a split aluminum pressure manifold that clamped onto and sealed against the sensor, as shown in Figure 28.
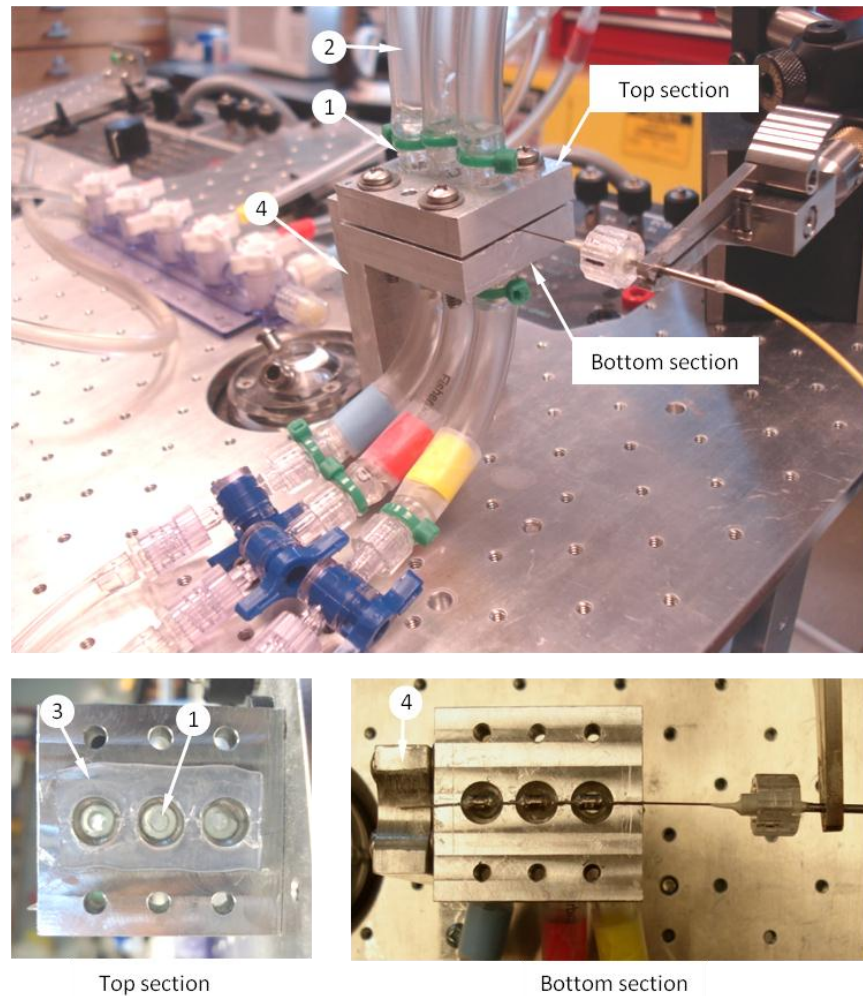
*Figure 28:  Split pressure manifold used to individually pressurize sensor pods. Sealing faces of top and bottom sections shown. Components: (1) Luer-Lok® connection, (2) Tygon tubing$^{TM}$, (3) Silicone seal, (4) Support Bracket.*

Within each half of the manifold were machined a series of cavities centered over the pods of the sensor. At the base of each cavity a through-hole was drilled at which point a Luer-Lok® connection (1) was glued into place to provide a mounting point for Tygon$^{TM}$ tubing (2). The top half of the manifold had a bead of silicone (3), (Dow Corning RTV 3140, Midland, MI), around the perimeter of the cavities to provide a sealing mechanism against the mating face of the bottom manifold section and the Nitinol$^{TM}$ tubing of the

sensor. The two halves of the manifold were secured together with four screws and supported by a custom bracket (4).

Valves were located upstream and downstream of each pressure chamber. Pressure was supplied through a mechanical screw-driven syringe upstream of the manifold and all downstream lines emptied into an open reservoir. The working fluid was room temperature water. Specifying which chambers were pressurized was achieved by controlling the appropriate upstream valves, as shown in Figure 29.
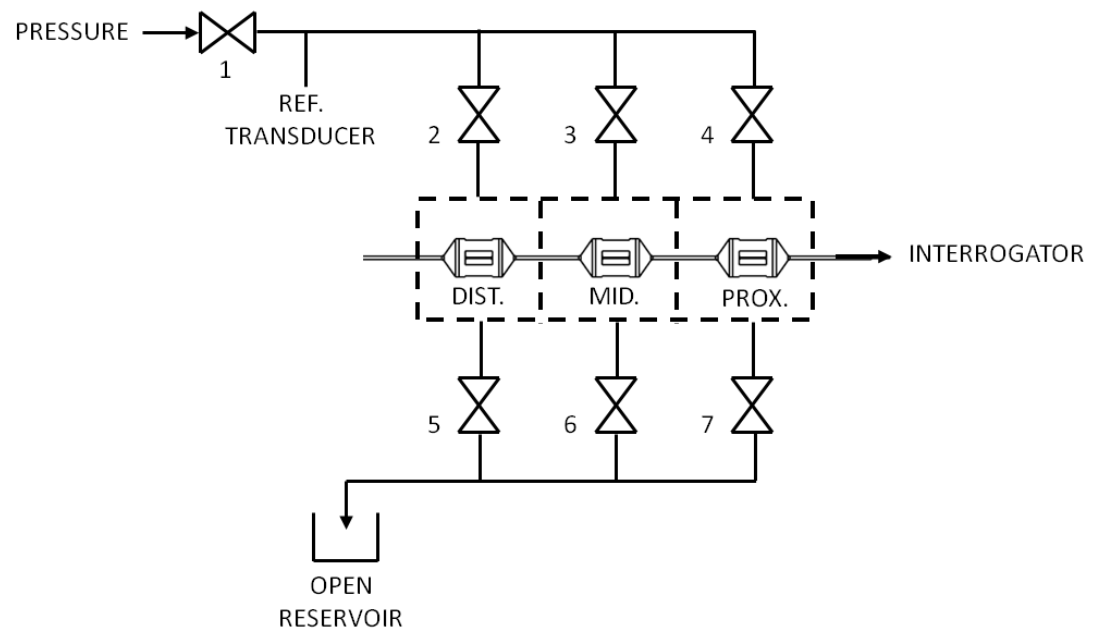


*Figure 29: Crosstalk test schematic. Numbered items indicate valves. Dashed line indicates pressure manifold envelope.*

To maintain a given sensor pod at atmospheric pressure, the chamber was drained of water and the upstream valve was closed while the downstream valve was opened. Alternatively, to pressurize a given pod, the pod was first filled with water and then flushed in both directions to remove entrapped air, after which the downstream valve was closed. To pressurize the distal sensor pod for example, valves (1), (2), (6) and (7) were opened while valves (3), (4) and (5) were closed.

Confirmation of sealing was achieved by individually pressurizing each chamber by hand with a syringe and checking for leaks in adjacent chambers; indicated by either dripping water or a loss of pressure within the chamber. Clamp force provided by the screws was increased until leaks were no longer detected. Hand-snugging with a screwdriver was typically sufficient.

System pressure was measured by a reference transducer (Omega© PX01K1-010G5T, 0-10psig, ±0.05%FSO, Omega Engineering Inc., Stamford, CT) located upstream of the manifold.

To characterize mechanical crosstalk, the follow procedure was used:

1.  Pressurization of proximal sensor:

    a.  Middle and proximal chambers were emptied of water and valves (3) and (4) were closed. Distal chamber was flushed and filled with water and valve (5) was closed. Valves (2) and (1) were open.

    b.  Baseline readings were logged for all sensor pods and reference transducer; providing a zero.

    c.  Pressure was applied via the screw driven-syringe. Valve (1) was immediately closed.

    d.  When pressure readings became constant points were logged.

    e.  Valve (1) was opened, pressure was incremented, and valve (1) was closed.

    f.  When pressure readings became constant points were logged.

    g.  Steps (c) to (g) were repeated until approximately 400 mmHg.

2.  Pressurization of middle sensor:

    a.  Repeated steps (a) to (g) with middle chamber pressurized and proximal and distal chambers emptied.

3. Pressurization of proximal sensor:

    a. Repeated steps (a) to (g) with proximal chamber pressurized and distal and middle chambers emptied.

Three data sets were produced from these tests which correspond to pressurization of the distal, middle and proximal sensor pods. To produce the correction coefficient matrix, linear regression was used for all series within each data set. For example, with the distal pod pressurized, linear regression was used to correlate wavelength shifts of the proximal and middle pods as a function of pressure applied to the distal pod, producing $\delta_{prox,dist}$ and $\delta_{mid,dist}$, respectively. This was repeated for all three data series and was used to populate the correction coefficient matrix, $[\delta]$, as previously described in Section 3.3.3.

To demonstrate the use of the correction matrix in practice, a worst-case crosstalk scenario was tested. In this trial, the proximal and distal pods were subjected to pressure while the middle pod remained at atmospheric pressure. This is a worst-case crosstalk scenario as it subjects the middle pod to the combined influences of two immediately adjacent pods.

An additional test in which only the distal pod was pressurized was conducted to characterize response under conditions more likely to occur with the device in practice.

To conduct the first demonstration, the middle manifold chamber was emptied of water and the two outer chambers (proximal and distal sensing pods) were pressurized. Testing was conducted in accordance with the methods outlined above. The resulting data series was then modified in post-processing. The wavelength shifts recorded at each pressure increment were multiplied by the correction coefficient matrix, generating a series of sensor data points that were crosstalk compensated. These compensated values for the middle sensing pod were then compared to the original non-compensated values to

indicate method efficacy. Post processing was conducted using a purpose-written MATLAB code (MATLAB V7.6, MathWorks, Natick, MA).

The second demonstration was conducted similarly with the middle and proximal pods emptied.

## 5.2. Testing with Contact Pressure Configuration:

For these investigations, the three-grating prototype sensor was sensitized to contact pressure using the methods previously described in Section 4.2.

### 5.2.1.  Pressure Sensitivity

The pressure sensitivity test was conducted in accordance with the methods outlined for the hydrodynamic configuration.

### 5.2.2.  Temperature Sensitivity

The temperature sensitivity test was conducted in accordance with the methods outlined for the hydrodynamic configuration.

### 5.2.3.  Contact Pressure Demonstration

The objective of this investigation was to demonstrate sensitivity of the sensing pods to contact pressure. To achieve this, the sensor was inserted into the contact pressure-applying device previously described in Section 5.1.2.

It should be noted that the contact pressure applied to the sensor pods is a function of both the hydrostatic pressure within the manifold and mechanical properties of the latex tube (refer to Figure 25). As such, this test was conducted as a qualitative demonstration

of response to contact pressure and was not designed to determine contact pressure sensitivity directly.

This test was conducted in accordance to the method previously described, with an additional post-processing step. As the effective sensitivities of the sensing pods were reduced in this device due to the mechanical properties of the rubber tube, the wavelength shift values were linearly scaled such that the peak pressures indicated by the sensors matched the peak pressure indicated by the reference manifold. This was done to more accurately compare the pressure waveform recorded by the sensing pods to the waveform recorded by the reference transducer.

# Chapter 6

## 6. Results and Discussion

To validate performance of the sensor design, two constructed prototypes, a three pod single-FBG prototype (referred to as the single-FBG prototype) and three pod three-FBG prototype (referred to as the three-FBG prototype), were used in a series of bench top tests. With the exception of grating count, the two prototypes were identical.

Testing was first conducted with both prototypes in the hydrodynamic pressure configuration. Investigations conducted with the prototypes in this configuration included pressure sensitivity, demonstration of insensitivity to contact pressure, flexibility and bending response, temperature sensitivity, axial load sensitivity, and crosstalk characterization, as described in Section 5.

Additional testing was done with the three-FBG prototype configured for sensitivity to contact pressure. These tests included pressure sensitivity, temperature sensitivity, and demonstration of sensitivity to contact pressure, as described in Section 5.

This chapter is a presentation of results from these tests.

### 6.1. Hydrodynamic Pressure Configuration Results:

#### 6.1.1. Pressure Sensitivity

The first test conducted was an investigation of sensitivity to hydrodynamic pressure for the two prototypes sensors. Response for the three-grating variant is shown in Figure 30.
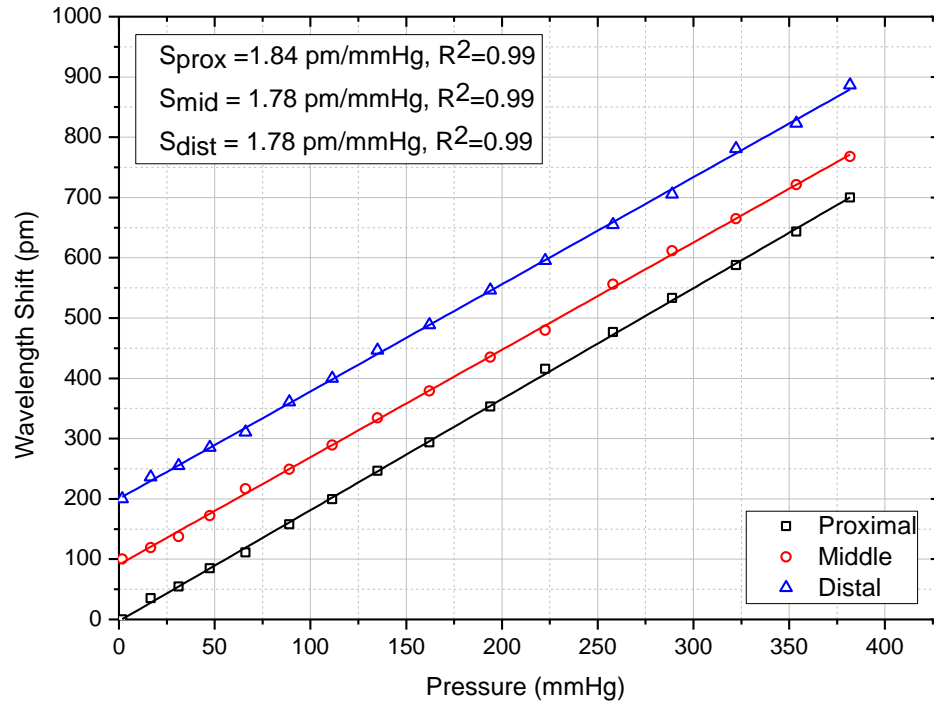
*Figure 30:  Measured hydrostatic sensitivities of the three-grating prototype in the hydrodynamic pressure configuration. Series shown with offset y-intercepts for clarity. Measured sensitivities indicated top left.*

As shown in the figure, the Bragg wavelengths increased in response to increases in hydrostatic pressure. The calculated sensitivities for the proximal, middle and distal sensing pods were 1.84 pm/mmHg, 1.78 pm/mmHg and 1.78 pm/mmHg, respectively; each with an $R^2$ of 0.99, indicating strong linearity.

The sensitivity of the single-grating sensor was determined to be 1.81 pm/mmHg, also with an $R^2$ greater than 0.99. The calculated sensitivities for all of the sensors were within 3.5% and were closely approximated by the 1.8 pm/mmHg predicted by theory (refer to Section 3.3.2). Sensor response remained linear across the entire operating range.

**6.1.2. Demonstration of Insensitivity to Contact Pressure**

To demonstrate the insensitivity of the sensor in the hydrodynamic configuration to contact pressure, the three-FBG prototype was tested with the contact pressure-applying device described in Section 5.1.2. Indicated pressure as a function of contact pressure is shown in Figure 31.
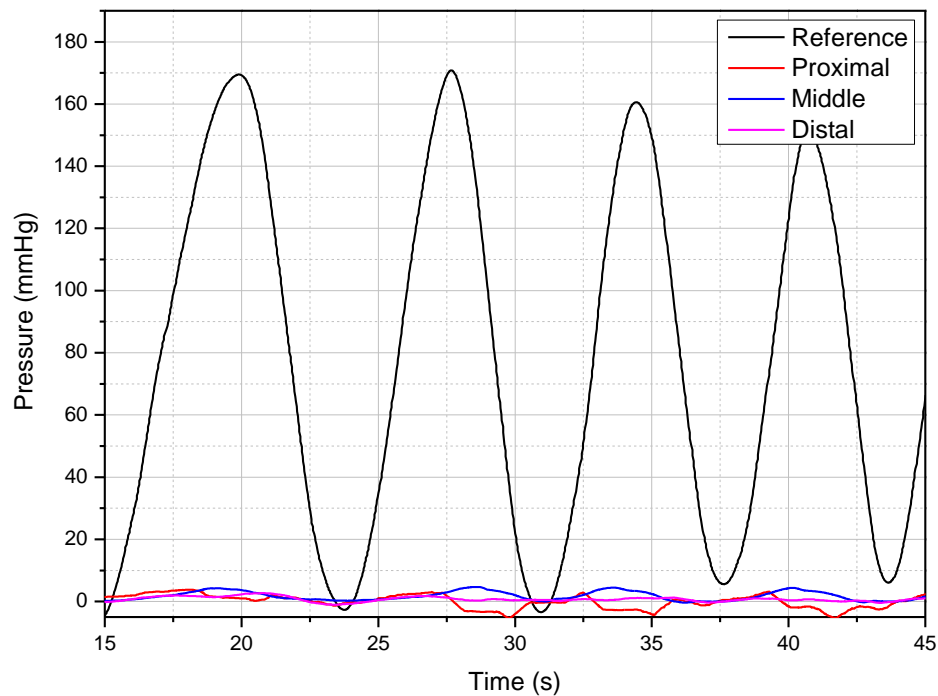


*Figure 31: Response to contact pressure in hydrodynamic configuration. Three-FBG sensor shown.*

The distal and middle sensors demonstrated negligible response (1 mmHg or less) to the applied contact pressure. However, the middle sensor yielded discernible peaks which approximately corresponded to the maximum manifold pressures, though the maximum indicated pressures of the sensor were low; approximately 4 mmHg or less. It is thought the minor response to contact pressure exhibited by the middle sensor is due to potential contact between the rubber tube of the contact pressure-applying device (refer item 2 of

Figure 25) and the silicone seal within the pod housing (item 3 in Table 2). Such contact

is possible if the seal has excess silicone protruding into the interior of the pod housing

and the compliance of the rubber tube is sufficient to penetrate a short distance into the

pod housing. However, this affect appears minor and is limited to the middle sensing pod.

In summary, the distal and middle pods demonstrated insensitivity to contact pressure,

while the proximal pod demonstrated only minor response.

### 6.1.3. Device Flexibility and Bending Response

The minimum bend radius for the sensor was estimated to be approximately 18 mm.

An image of the sensor achieving this bend radius is shown Figure 32. Bending at this

radius did not induce any permanent deformation and the sensor continuously sprung

back to its original shape through repeated trials.
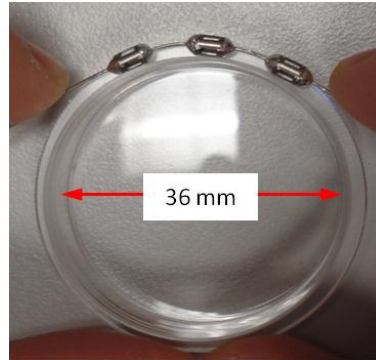


*Figure 32:   Demonstration of sensor flexibility. Sensor shown with a bend radius of 18 mm.*

The grating within the sensor was monitored at all times during these flexibility tests to

identify any potential signs of fibre distress. No such signs were observed during testing:

there was no noticeable attenuation of the Bragg signal and the total shift of the Bragg

wavelength was small in the context of its maximum allowable dynamic range. These

tests were repeated for the one-grating sensor and the three-grating sensor with no variation in results, suggesting high consistency from prototype to prototype.

For investigation of the effect of bending on indicated pressure, a three-point bend test was conducted. Results for the one-grating sensor prototype is presented in Figure 33.
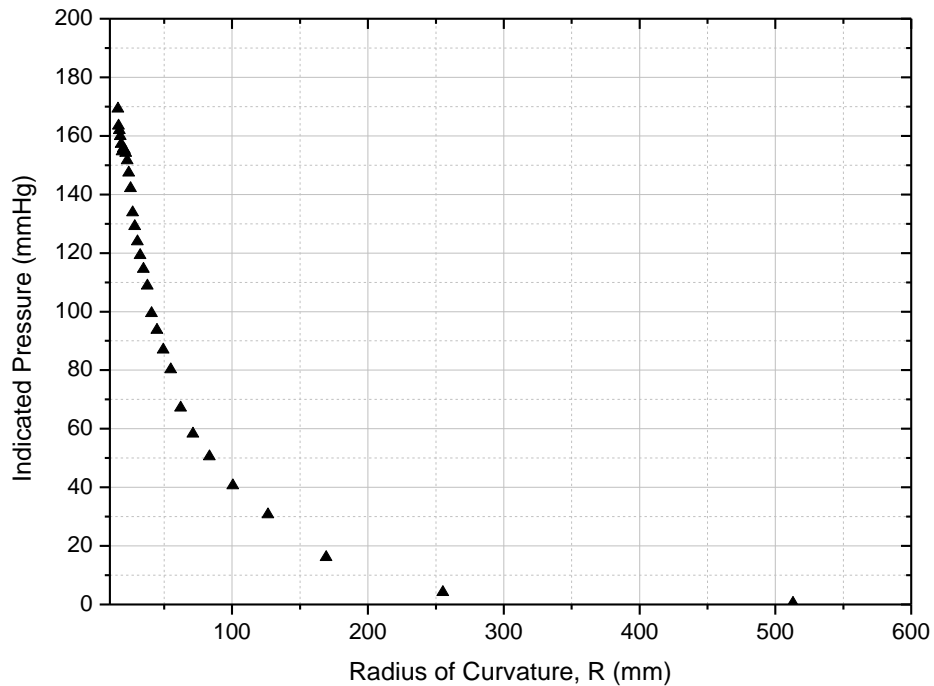


*Figure 33:   Indicated pressure as a function of bending for the one-grating sensor prototype.*

As shown in the figure, indicated pressure is strongly influenced by bending at small radii. The indicated pressure remained below 5 mmHg until the bending radius of curvature approached 250 mm; beyond which the indicated pressure began to rise significantly. At radii tighter than 60 mm or so, the response became approximately linear. At the maximum bend radius tested, 15 mm, the indicated pressure was about 170 mmHg.

**6.1.4. Temperature Sensitivity**

For the investigation of temperature sensitivity, increasing temperature resulted in increasing Bragg wavelengths, and thus, an increase in erroneous indicated pressure. A plot of these results is shown in Figure 34.
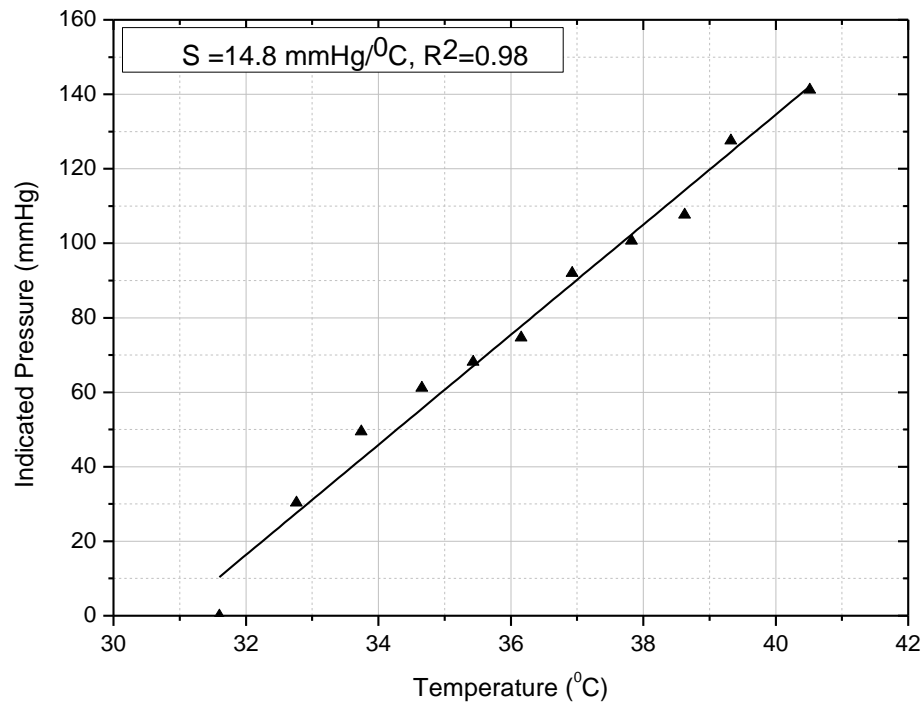


*Figure 34: Temperature sensitivity in hydrodynamic configuration for single-grating sensor. Calculated sensitivity to temperature influence is 14.8 mmHg/°C.*

For the single-grating sensor prototype, the relationship between indicated pressure and temperature was determined to be 14.8 mmHg/°C with an $R^2$ of 0.98, indicating strong linearity.

**6.1.5. Axial Load Sensitivity**

Results for the axial load sensitivity test are shown in Figure 35.
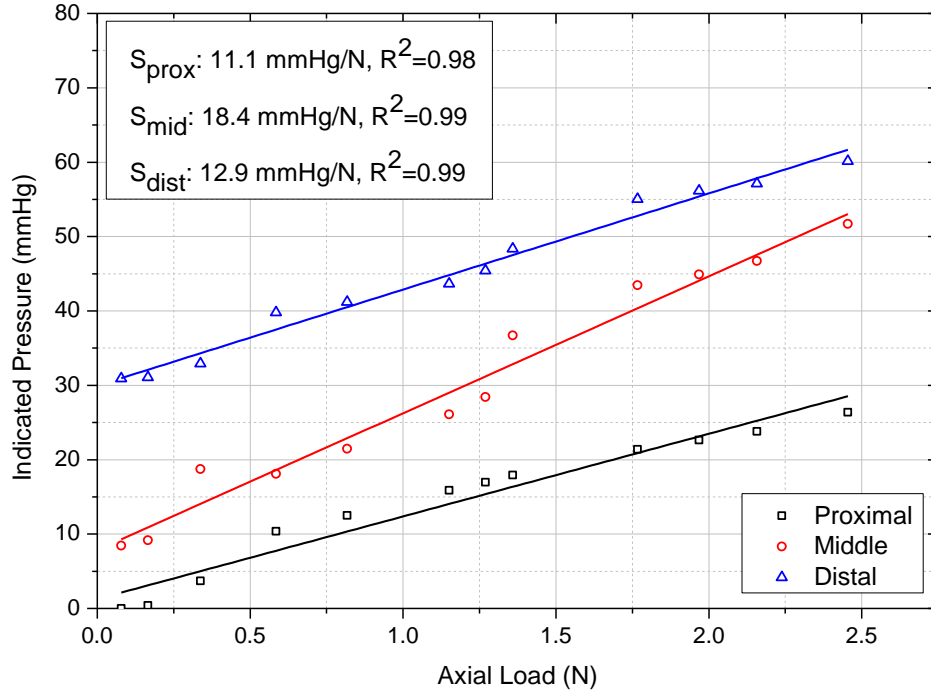
*Figure 35: Sensitivity to axial loading. Results from three-grating sensor presented here.*
*Plots shown here with arbitrary intercepts for clarity.*

It was observed that applying an axial load to the sensor superstructure resulted in an increase in Bragg wavelengths, which resulted in an increase in indicated pressure. The proximal, middle and distal sensors of the three-grating prototype yielded an indicated pressure per applied load of 11.1 mmHg/N, 18.4 mmHg/N and 12.9 mmHg/N, respectively. Scatter in the results is thought to be due to imperceptible swinging of the free-hanging masses during testing, though this affect appears to be minor as the $R^2$ values for all responses were greater than 0.9, indicating that the responses were linear across the load range tested.

### 6.1.6. Crosstalk Characterization and Correction

To populate the correction coefficient matrix, the proximal, middle and distal pods were individually pressurized. Pressurizing the middle pod alone resulted in a positive

wavelength shift for the middle sensor and negative wavelength shifts for the proximal and distal sensing pods. A plot of the middle pod pressurization trial is show in Figure 36.
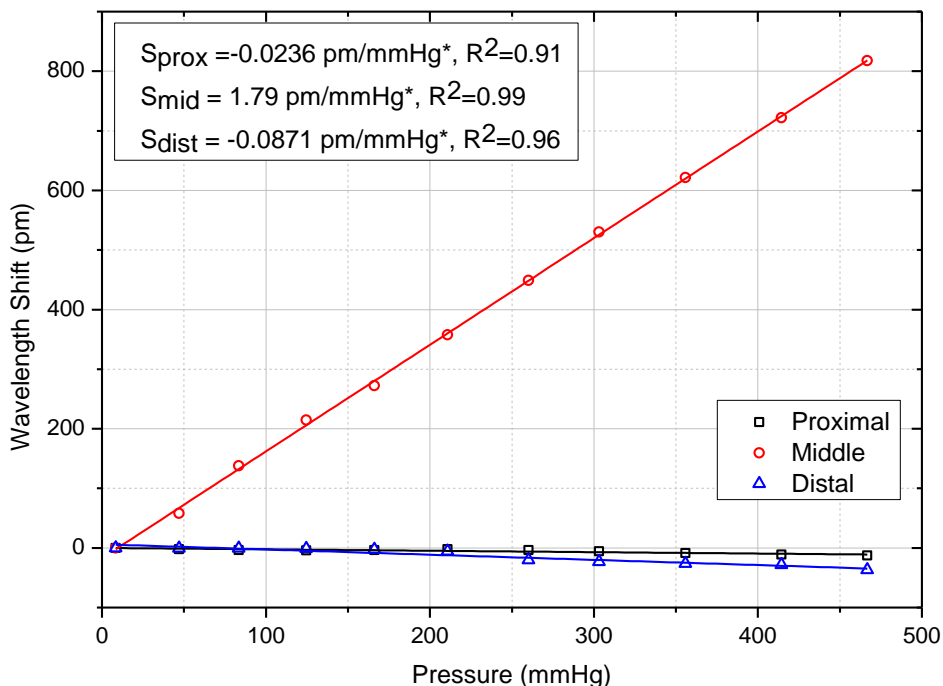


*Figure 36: Response curves for pressure applied to the middle sensing pod. (\*) indicates wavelength shift per unit of pressure applied to middle pod. Pattern shown here is indicative of results for when the proximal and distal pods are individually pressurized.*

As shown in the figure, the middle sensor responded with a pressure sensitivity of 1.79 pm/mmHg, while the proximal and distal sensors responded with -0.0236 and -0.0871 pm/(mmHg of pressure applied to middle pod), respectively. All $R^2$ values were 0.9 or better.

The negative slopes of the proximal and distal responses indicate that pressure applied to the middle pod induces compressive strain within the proximal and distal sensing pods. Dividing the response of these two sensing pods by the response of the middle sensor yields crosstalk values, as shown in Table 3.

*Table 3: Crosstalk characterization and correction coefficient matrix*

| | Sensitivity (pm/mmHg) | | | Correction Matrix* [$\delta$] | | |
|---|---|---|---|---|---|---|
| | **Proximal Response** | **Middle Response** | **Distal Response** | | | |
| **Proximal Pressurized** | **1.86** (0.99) | -0.0435 (0.85) | -0.00801 (0.91) | 1 | -0.0235 | -0.00430 |
| **Middle Pressurized** | -0.0236 (0.91) | **1.79** (0.99) | -0.0871 (0.96) | -0.0132 | 1 | -0.0486 |
| **Distal Pressurized** | -0.0157 (0.95) | -0.0686 (0.98) | **1.77** (0.99) | -0.00887 | -0.0387 | 1 |

($R^2$ values shown in brackets)
*correction coefficients unitless

For example, dividing the proximal response (-0.0236 pm/mmHg) by the middle response (1.79 pm/mmHg) results in a crosstalk of -1.32%, from the middle to the proximal sensing pod. Similarly, crosstalk from the middle pod to the distal pod is -4.86%. These calculated crosstalk values represent coefficients in the correction matrix [$\delta$] (refer Section 3.3.3). Specifically, $\delta_{prox,mid}$ (influence on the proximal pod from the middle pod) is -0.0132, and $\delta_{dist,mid}$ (influence on the distal pod from the middle pod) is -0.0486, as shown in Table 3.

Similar patterns were obtained from the distal and proximal pressurization tests. For the proximal test, the responses were 1.86, -0.0435 and -0.00801 pm/(mmHg of pressure applied to proximal pod) with $R^2$ values of 0.99, 0.85 and 0.91 for the proximal, middle and distal pods, respectively. This resulted in crosstalk values from the proximal pod to the middle and distal pods of -2.35% and -0.430%, respectively.

The distal-pressurization test resulted in -0.0157, -0.0686 and 1.77 pm/(mmHg of pressure applied to distal pod) with $R^2$ values of 0.95, 0.98 and 0.99 for the proximal, middle and distal sensors, respectively. This resulted in crosstalk values from the distal pod to the middle and proximal pods of -3.87% and -0.887%, respectively.

To demonstrate the crosstalk correction method, the proximal and distal sensor pods were pressurized while the middle pod was left at atmospheric pressure (reference

pressure of 0 mmHg). The indicated pressure of the middle pod was then corrected by multiplying the measured wavelength shifts by the inverse of the correction matrix [δ] (refer Equation 3.12), at each test pressure. These values are referred to as the corrected values. The results for both the corrected and uncorrected values of the middle sensor pod for the test-pressures of the proximal and distal pods are shown in Figure 37.
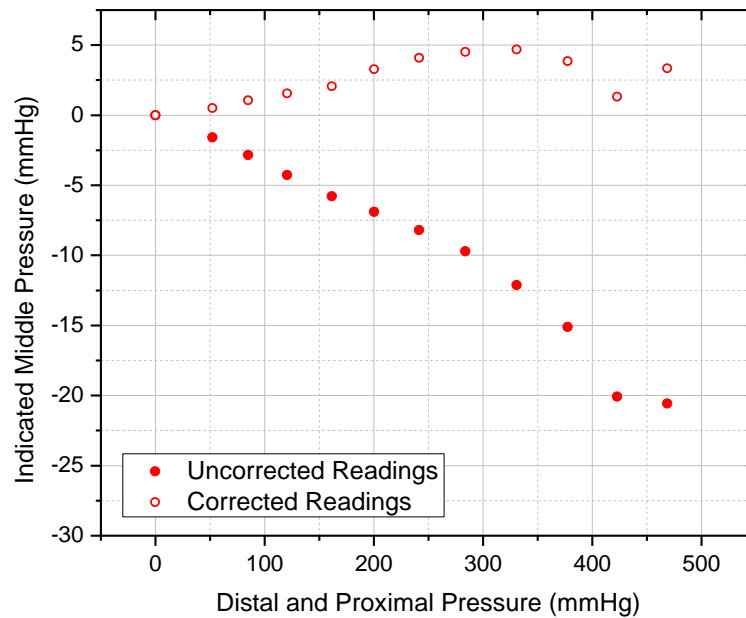


*Figure 37:   Crosstalk correction – response of middle sensor when distal and proximal prods are pressurized.*

The uncorrected values demonstrate a strong negative trend as pressure increases in the proximal and distal pods, while the corrected values remain less than 5 mmHg. The trend of the corrected values is non-linear. At the maximum pressure in the distal and proximal pods, the uncorrected values indicate approximately -21 mmHg, while the corrected values indicate a pressure of approximately 4 mmHg; an 80% reduction in erroneous pressure indication. When the proximal and distal pods are pressurized to about 150

mmHg, the maximum occlusion pressure within the esophagus, the uncorrected and corrected readings are approximately 6 mmHg and 2 mmHg respectively; a 67% reduction in error.

An additional test was conducted with only one sensing pod pressurized to characterize response with reduced crosstalk influences. In this case, the distal pod was pressurized and the middle and proximal pods were left at atmospheric pressure. Results are shown in Figure 38.



*Figure 38: Crosstalk correction – distal pod pressurized, middle and proximal held at atmospheric. Filled points indicate uncorrected values*

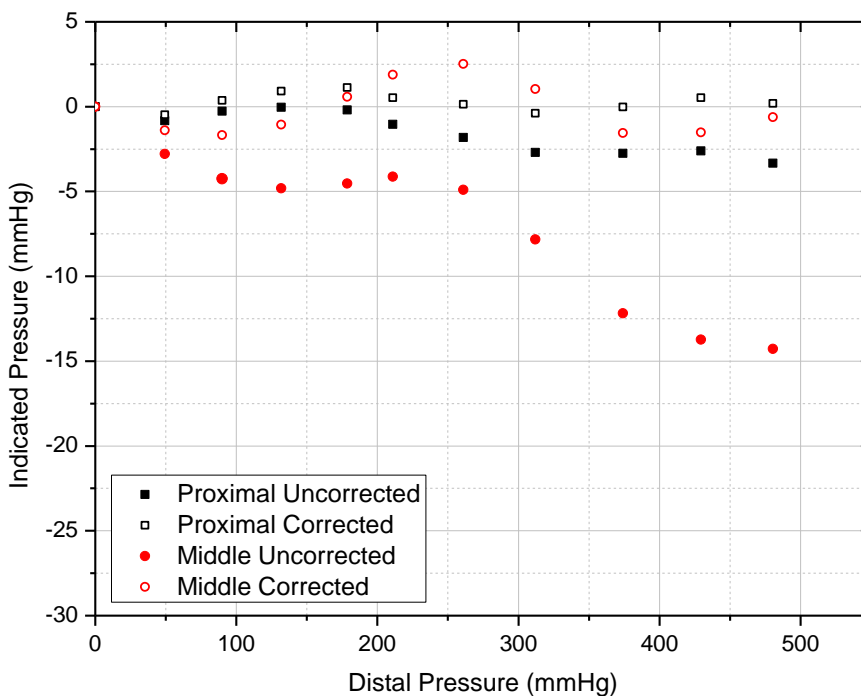As shown in figure, when the distal pod is pressurized the middle pod, and to a lesser extent the proximal pod, generally responds with a negative indicated pressure (filled data points) over the pressure range tested. In contrast, the corrected (unfilled) values are

not a linear function of applied distal pressure and these corrected values are generally an improvement (closer to 0 mmHg indicated pressure) over the uncorrected values.

There are test points where the proximal uncorrected values are closer to 0 mmHg than the corrected values, at distal pressure of 130 mmHg for example, though these data points are isolated incidents and the magnitude of the erroneous readings are approximately 1.25 mmHg of indicated pressure or less, for both the corrected and uncorrected values.

At a distal pressure 130 mmHg, the uncorrected indicated middle pressure is approximately -5 mmHg, while the corrected reading is approximately -1 mmHg; an 80% reduction in erroneous pressure reading. At higher pressures, the improvement of the corrected values over the uncorrected values increases.

In summary, these results demonstrate that pressure readings corrected with the crosstalk correction method are an improvement over uncorrected measurements.

## 6.2. Contact Pressure Configuration Results:

For these tests, the three-grating sensor was potted with ultra-soft silicone gel and dip-coated with encapsulating silicone using the methods described in Section 4.2. The resulting silicone encapsulation of the sensing pods was approximately uniform around the circumference of the pods, however, thicknesses differed from one pod to the next. The middle pod had the thinnest jacket of silicone with an overall diameter of about 3.3 mm, followed by the proximal pod with a diameter of 3.5 mm, and the distal pod with a diameter of about 3.6 mm. These variations in thicknesses were the result of the 'dip-coating' method of encapsulation used. While these diameters were slightly greater than

the designed diameter of the sensor, they were acceptable to characterize response in this configuration.

The results of testing in this contact-sensitive configuration are reported below.

### 6.2.1. Pressure Sensitivity

The pressure response of the sensor in the contact-sensitive configuration is similar to the hydrodynamic configuration: application of hydrostatic pressure results in a linear increase of the Bragg wavelengths, as shown in Figure 39.
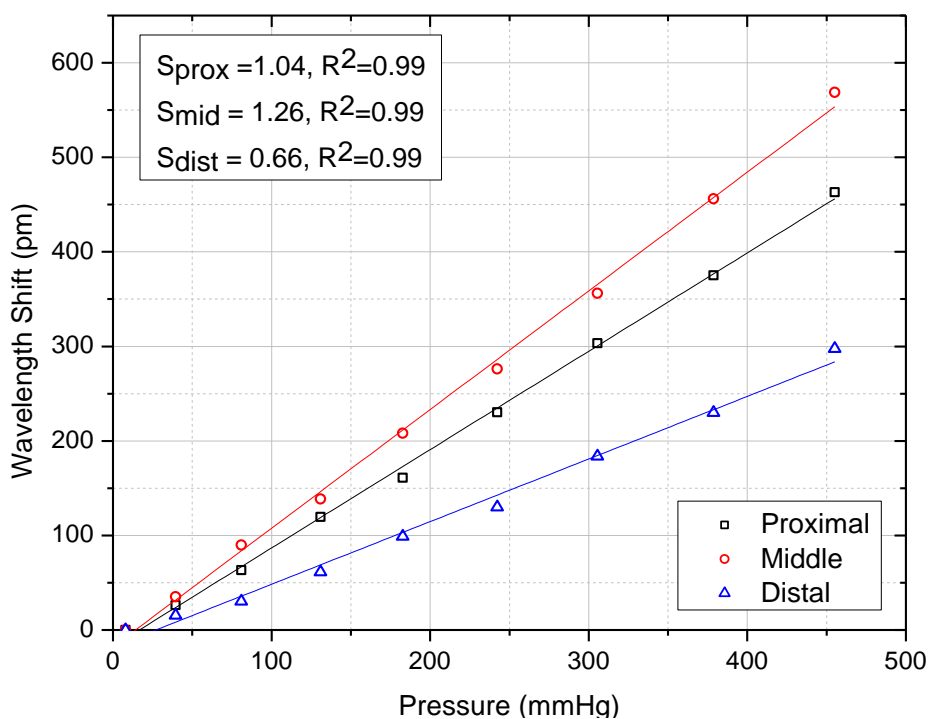


*Figure 39: Sensitivity to hydrostatic pressure in contact-sensitive configuration*

The sensitivities were calculated to be 1.04 pm/mmHg, 1.26 pm/mmHg and 0.66 pm/mmHg for the proximal, middle and distal pods, respectively. Each $R^2$ value was 0.99 or better, indicating strong linearity.

The reduction in pressure sensitivity for each of the pods from the hydrodynamic configuration is 42%, 26% and 61% for the proximal, middle and distal pods, respectively. The magnitude of these sensitivity losses correspond approximately to the thickness of the silicone encapsulating each of the pods.

### 6.2.2. Temperature Sensitivity

As with the previous temperature sensitivity test, an increase in temperature resulted in an increase in the Bragg wavelengths which resulted in an increase in indicated pressure, as shown in Figure 40.
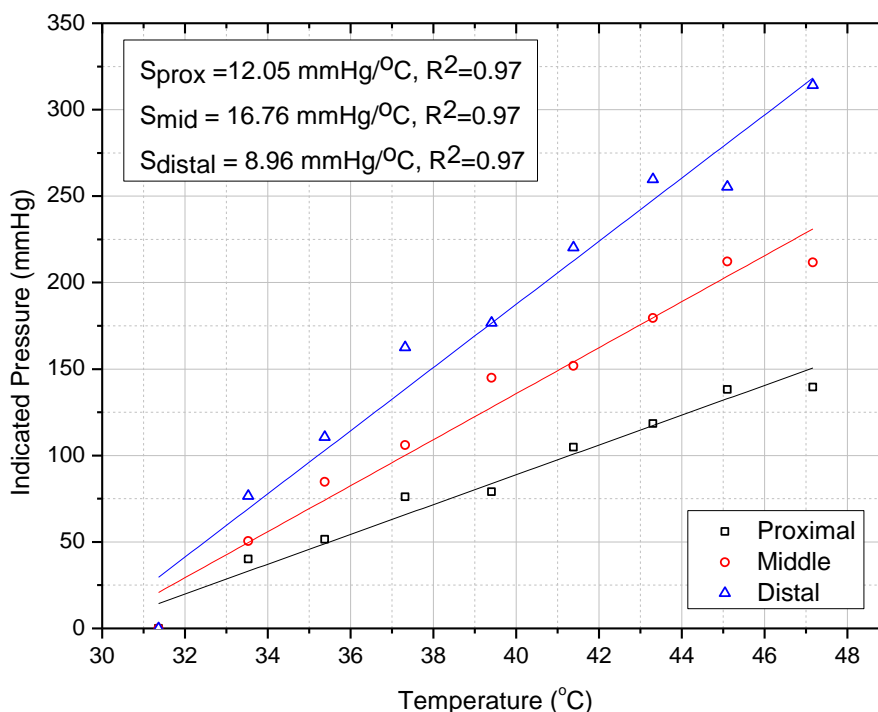


*Figure 40:   Temperature sensitivity of sensor in contact-sensitive configuration*

The sensitivities for the proximal, middle and distal pods were 12.1 mmHg/$^o$C, 16.8 mmHg/$^o$C and 9.0 mmHg/$^o$C respectively, each with an $R^2$ value of 0.97. These

temperature sensitivity values are comparable to those obtained from the non-encapsulated prototype (14.8 mmHg/$^{o}$C).

### 6.2.3. Contact Pressure Demonstration

In this sensing configuration, the pods responded to contact pressure. Increasing the contact pressure on each of the pods yielded a response similar to the application of hydrostatic pressure. A pressure waveform reproduction of the sensor is shown in Figure 41.
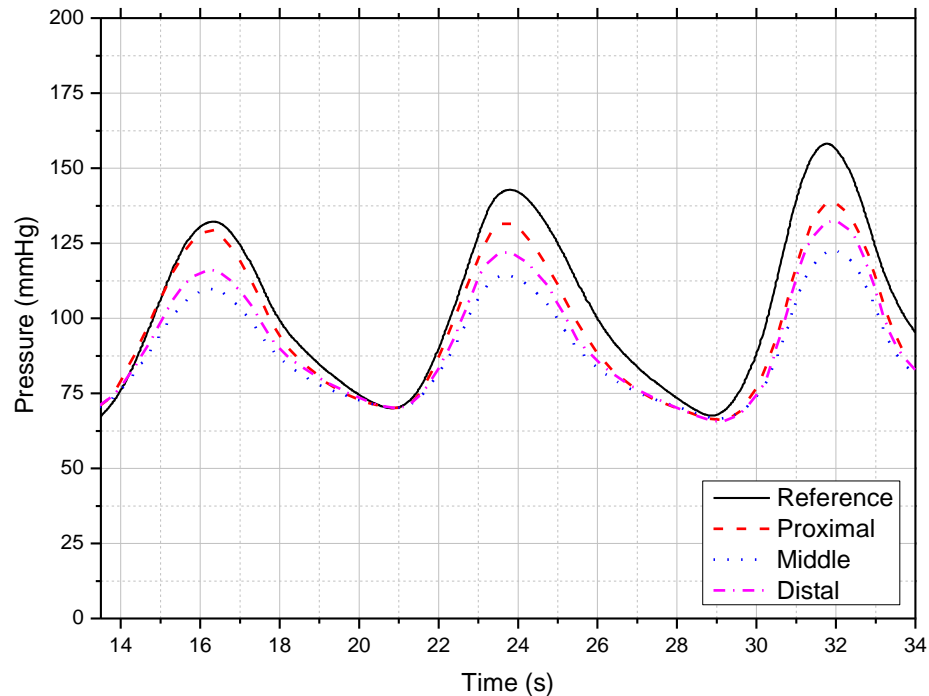


*Figure 41: Response of sensors in contact-sensitive configuration to contact pressure waveform using sensitivities calculated from hydrostatic pressure test in Section 6.2.1.*

As depicted, the pressure readings of each of the pods follow the waveform of the reference pressure for both increasing and decreasing pressures, though the peak pressure readings do not match. The mismatch in maximum pressure indications between the sensors and the reference transducer is due to the loss in pod sensitivity from the

mechanical properties of the latex rubber tubing of the contact-pressure device (refer Figure 25).

To correct for influence of the rubber tubing, pressure readings from the sensors were linearly scaled such that the maximum pressure readings from the sensor were approximately equal to maximum readings from the reference transducer. Scaling was achieved by adjusting the sensitivities for each of the pods. A plot of the scaled values is shown in Figure 42.
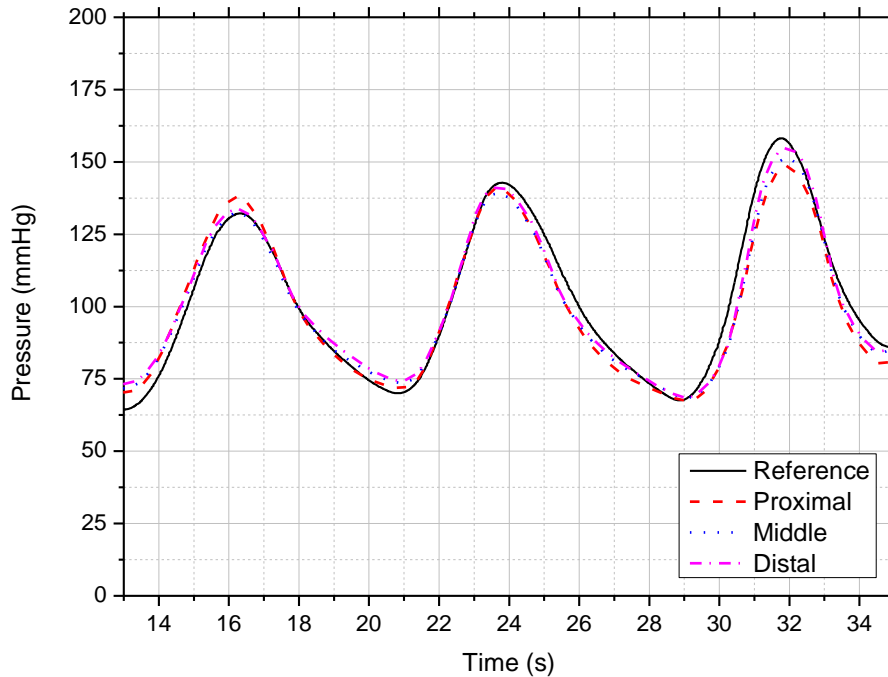


*Figure 42:   Scaled response of sensors in contact-pressure configuration. Adjusted sensitivities used here are 0.9, 0.8 and 0.5pm/mmHg for the proximal, middle and distal pods, respectively.*

The adjusted sensitivities used to achieve approximate peak matching were 0.9, 0.8 and 0.5 pm/mmHg for the proximal, middle and distal pods, respectively. From the scaled plot, it is evident that the pressure readings from the sensors are a reproduction of the

pressure waveform recorded by the reference transducer. These results are a successful demonstration of sensitivity to contact pressure.

## 6.3. Discussion

A key strength of this sensor design is its sensitivity. In the hydrodynamic configuration, the minimum calculated sensitivity of 1.7 pm/mmHg for the middle and distal pods exceeds the sensitivities reported by Arkwright, Voigt and Singlehurst [16][19][1]. This suggests that in instances of hydrodynamic pressures measurement, this design may provide superior pressure resolution over comparable devices. It should be noted, however, that the pressure resolution achieved in practice is a function of the wavelength resolving power of the interrogation system. The WDM interrogator used for these investigations provides a wavelength resolution of approximately 0.4 pm, which yields an as-tested pressure resolution of about 0.2 mmHg.

The TDM interrogator of the completed system is expected to provide a wavelength resolution of better than 1 pm, which theoretically yields a conservative pressure resolution of about 0.6 mmHg; exceeding the resolution specified in Table 1 (1 mmHg).

It was demonstrated that the sensing pods in the hydrodynamic configuration, with the exception of the proximal pod, were insensitive to contact pressure. As the middle pod exhibited minor response to contact pressure, it should be noted that manufacturing errors, in this case excess silicone in the silicone seal (item 3 of Table 2), may inadvertently sensitize a pod to contact pressure. In general, however, this test confirmed the pressure-specificity of the sensing pods in the hydrodynamic configuration.

In the contact-sensitive configuration, the middle sensing pod had a hydrodynamic sensitivity of 1.2 pm/mmHg; still higher than that of alternative optical designs. The remaining two pods yielded sensitivities comparable to those achieved by Arkwright [16]. Assuming a wavelength resolution of 1 pm (with the TDM unit), the proximal and middle pods theoretically achieve pressure resolution better than 1 mmHg, while the distal pod yields a resolution of 1.5 mmHg. These variations in pressure sensitivity suggest that the design is sensitive to the thickness of the silicone encapsulation, as would generally be expected. A thicker silicone encapsulation results in a reduction in sensitivity.

The resolutions of the proximal and middle sensing pods confirm that this sensor design is capable of achieving the resolution specifications of the HRM system, but the low resolution of the distal pod suggests that care should be taken to control the overall diameter of the encapsulating silicone. It should be noted that the results achieved here are a conservative characterization of sensitivity performance in the contact-sensitive configuration as silicone extrusion methods that control encapsulation thickness, such as with a commercial silicone extruder, are expected to yield a thinner and more uniform silicone coating. This is expected to yield improvements in sensitivity and consistency.

Based on qualitative assessment of the pressure waveform reproduction, testing of the contact-sensitive pods in the contact pressure device (refer Section 5.2.3) confirmed that the sensor responds to contact pressure. In summary, sensitivity to pressure in both hydrodynamic and contact pressure configurations has been successfully demonstrated.

The minimum radius of curvature required to introduce a manometer into the esophagus is 50 mm, as specified in Table 1. The bending results from these

investigations indicate that the mechanical flexibility of this design is more than sufficient; achieving a minimum radius of approximately 18 mm. At radii of curvature less than about 250 mm the sensor exhibits sensitivity to bending, though this is not expected to be an issue in practice as the esophagus is primarily straight and the sensing section of the device will not be bent when measurement is taking place. The sensitivity to bending in alternative optical designs has not been reported, so a direct benchmark of these results against comparable system cannot be done. As the optical fibre is the primary axial load path in Voigt's and Arkwright's design, and is a lesser but still significant load path in Singlehurst's design, it is suspected that the bend sensitivity demonstrated here is an improvement over comparable optical HRM sensors, though this has not been confirmed.

Regarding the temperature sensitivity tests, a notable result is that the temperature response of the pods in the hydrodynamic-specific configuration is comparable to response of the contact-sensitive configuration. The coefficient of thermal expansion for silicone elastomers is typically an order of magnitude higher than most metals and the optical fibre. It follows that introducing silicone to the sensing mechanism of the device would significantly increase its sensitivity to temperature. It is suspected, however, that the large sensing ports of this design are sufficient to allow the silicone gel to expand outward with minimal expansion force imparted to the rigid diaphragms, resulting in a comparable temperature response between the potted and un-potted configurations.

An important aspect of the sensor's response to temperature is linearity. The $R^2$ coefficients calculated from these tests indicate that linearity is such that a procedural temperature correction method similar to that of Sierra Scientific' solid state HRM device

(described in Section 2.6.3) may be successfully applied here. As a result the confounding influence of temperature is expected to be procedurally managed when the device is used in practice.

As previously discussed, the esophagus can impart axial load in excess of 140 g, which when applied directly to this sensor superstructure, would result in an erroneous pressure reading of about 25 mmHg. It is difficult to benchmark the axial loading sensitivity of this design as the axial loading sensitivities of comparable optical systems are unreported. Comparable devices utilize a silicone sleeve to minimize the 'grip' that the esophagus can impart to the sensor; the efficacy of which is unknown. The design presented here affords a two-pronged approach: it largely removes the fibre as an axial load path and the superstructure is to be encased in a silicone sleeve, as per comparable systems. Therefore, it is the opinion of this author that this design marks an improvement in the isolation of pressure readings from axial loads over alternative designs.

The design trade-off for the enhanced sensitivity, flexibility and resistance to axial loading affects is mechanical crosstalk. As shown in Table 3, the maximum crosstalk sensitivity was measured to be about 5% (uncorrected) for the case of the middle pod affecting the proximal pod. The influence is highest on directly adjacent pods and sensing pods that are not direct neighbours experience minimal crosstalk, typically 1% or less, indicating that the effect of crosstalk is largely localized. Testing a scenario in which a non-pressurized pod is bookended by two pods pressurized to about 400 mmHg has resulted in an erroneous readings of about -20 mmHg and 5 mmHg for uncorrected and corrected values respectively. This yields a combined crosstalk influence of about 1.25% after correction, which is a 75% reduction compared to the uncorrected values. This is a

significant improvement. When surrounding pods are pressurized to 150 mmHg or less, a maximum value typical in esophageal manometry, the uncorrected readings exceed 5 mmHg, whereas the corrected readings remain approximately 2.5 mmHg or less. At these low pressures, the correction method yields an improvement in readings of 50% or more. This demonstration is a clear indication that the crosstalk reduction method succeeds in reducing erroneous pressure readings.

In practice, the 'worst-case' scenario demonstrated here is not likely to occur. Instead, the maximum influence of crosstalk for the sensor within the esophagus will occur in the instance two of sensing pods straddling the bolus no-bolus demarcation line; simulated in the second crosstalk demonstration. In this case, the esophageal occlusion pressure on the 'no-bolus' side of the demarcation line, assumed to be 100 mmHg or so, will increase measurements on the 'bolus' side of the demarcation line by about 1% of 100 mmHg after correction, or 1 mmHg, assuming the 'no-bolus' sensor is sensitive to contact pressure. In the event that sensors are sensitive to hydrodynamic pressure only, a typical maximum pressure measurement would be about 30 mmHg (corresponding to maximum intrabolus pressure), and yield a crosstalk influence of about 0.3 mmHg; negligible in this context. In summary, residual crosstalk measurement error is not expected to be significant after correction under conditions typical of esophageal manometry.

It is expected that these corrections can be improved through enhanced fabrication precision. Manufacturing flaws create deviations from idealized geometry which complicates crosstalk and are suspected to be the primary contributor to non-linearity (see $R^2$ values less than 0.9 in Table 3 and the slight 'wave' affect in Figure 38). It has been the experience of this author that a fully assembled superstructure occasionally exhibits a

minor bend, typically due to the solder connections as Nitinol$^{TM}$ tubes may not be perfectly normal to capping washer faces. Clamping the slightly bent sensor into the pressure manifold used for crosstalk analysis forces the sensor straight, which can induce small displacements of the rigid diaphragms axially along the sensor and, to a lesser extent, radially. It is suspected that this introduces microbends in the optical fibre, which may contribute to some crosstalk non-linearity. An additional source of non-linearity can likely be attributed to the non-uniform dispersion of silicone around the annular seal (item 3 in Figure 13). Applying excess silicone to one location on the circumference of the rigid diaphragm will result in a silicone seal with an axially-varying stiffness. These 'stiff points' of the annulus may induce a moment in the fibre as it translates, inducing a microbend which may alter the Bragg reflection. Non-linearity exhibited by one sensing pod will affect adjacent pods. It is expected that these sources of error can be reduced through improved manufacturing methods. Overall, the results obtained in these investigations demonstrate that sensor crosstalk can be successfully characterized and largely compensated.

## 6.4. Summary

In summary, these investigations have successfully demonstrated sensor response to both hydrodynamic and contact pressure, achieving the pressure-specificity and sensitivity requirements listed in Table 1. Additionally, the sensor was demonstrated to be sufficiently flexible for use within the esophagus. The demonstrated linearity in the sensor's response to temperature indicates that a procedural temperature-correction method may be used to correct for temperature influences, similar to Sierra Scientifics

solid state sensors. Finally, the mechanical crosstalk can be characterized and the method to correct for it has been validated. Refinements in manufacturing techniques may improve crosstalk compensation further. In conclusion, these tests have demonstrated that sensor performance achieves the specifications outlined in Table 1.

# Chapter 7

## 7. Conclusion and Future Work

In the practice of high resolution manometry, existing manometric devices are subject to two limitations: (1) they generally do not exceed 36 sensing points and, (2) they cannot discern between hydrodynamic pressure and esophageal occlusion (contact) pressure in the absence of other measurements. The ability to discern hydrodynamic pressure alone is of benefit as measurement of intrabolus pressure is a direct indicator of the efficacy of bolus transport. Additionally, there are a number of clinically relevant parameters that are based on intrabolus pressure.

The introduction of fibre optics to the field of HRM has promised to extend the 36 sensing sites of current solid state manometer designs, addressing the first limitation of existing devices. However, the majority of these optical HRM designs do not address the second limitation of existing devices as they are unable to differentiate between contact and hydrodynamic pressure.

Singlehurst *et al* [1] have proposed an optical distributed pressure sensor capable of sensing hydrodynamic pressures only, potentially affording a solution to both limitations of conventional devices when applied to HRM. However, Singlehurst's design as reported does not meet the flexibility or spatial resolution requirements for HRM. Additionally, a method to sensitize the proposed device to contact pressure, a measurement required in conjunction with hydrodynamic pressure, is also lacking.

In this work, Singlehurst's sensing mechanism is further developed to create a fibre-optic based HRM system capable of sensitization to either hydrodynamic pressure alone,

or hydrodynamic and contact pressure. This pressure-selective configuration may allow the assembly of HRM arrays with novel sensing schemes.

Development of this HRM system has been comprised of two components: (1) development of a mechanical sensing array, and (2) development of a novel interrogation scheme. Concerning (2), the developed device is intended to be interrogated with a technique referred to as time division multiplexing, necessary to achieve 36 sensing sites or more. Time division multiplexing is a method that allows interrogation of individual gratings centred on the same Bragg wavelength by reading reflected pulses separated by a time delay. This technique has the advantage of allowing each grating to be centred on the same Bragg wavelength, reducing grating costs, and also affords a high interrogation frequency. Development work on this component of the HRM system has been conducted by others.

This thesis has been a presentation of item (1) of the developed HRM system: design of the mechanical sensing array. An analysis of the operating principle and a discussion of the parameters governing performance were provided with theoretical benchmarking against comparable designs. Through a novel variation from Singlehurst's design, pressure sensitivity, mechanical flexibility and axial-loading insensitivity were improved. The trade-off for this improved performance is mechanical crosstalk between sensing pods. A method of characterizing the crosstalk between pods was derived and a correction method that can be used to correct for crosstalk was developed and validated.

Sensor fabrication methodology was developed using laser machining with a femtosecond laser. A purpose-built 'laser lathe' was designed and constructed to provide the ability to laser-cut the main sensing pods of the sensor with high precision and

repeatability. An assembly technique was developed to fabricate the opto-mechanical sensing pods and assemble the metallic superstructure.

Characterization and performance assessments of the sensor were conducted through benchtop testing of fabricated three-pod prototypes. The sensor design was demonstrated to achieve a hydrodynamic sensitivity higher than any other comparable design. As well, the linear temperature response was such that procedural methods may be used to correct for the influence of temperature on the device, similar to practices employed currently in industry. The insensitivity to axial loading of this device is thought to be superior to comparable designs. Mechanical crosstalk in the sensor has been characterized and a correction method successfully demonstrated.

In summary, the optical HRM design presented here provides the opportunity to more directly measure intrabolus pressure with the option of also measuring contact pressures. This may provide a more direct measure of clinically relevant parameters in esophageal manometry that are not achievable with any single existing device.

## 7.1. Future Work

While this design has been demonstrated to achieve the HRM specifications outlined in Table 1, there is scope for future work.

The first area that warrants additional efforts is the encapsulation of the device in silicone. While it has been shown that the device is sensitive to contact pressure when encapsulated, a method to control silicone thickness and uniformity has not been developed. Encapsulation is likely to be most easily achieved by modifying a standard

commercially available silicone extruder, and it is recommended that this approach be employed. Encapsulation in silicone will be necessary in the event of *in vivo* trials.

There may be opportunity to simplify assembly of the mechanical superstructure. Nitinol$^{TM}$ cannot be welded to stainless steel, and it is for this reason that engineered solder has been used. However, Nitinol$^{TM}$ can be welded to itself. It is available in thin sheets and larger tubing, so it may be possible to replace the entire metallic superstructure with Nitinol$^{TM}$, instead of a mix of Nitinol$^{TM}$ and stainless steel. This would allow the entire assembly to be welded together instead of using solder. An assessment of cost implications is warranted, however, as Nitinol$^{TM}$ is considerably more expensive than stainless steel.

Further development work is also required for the TDM system. At the time of writing this, a proof of concept benchtop trial has been demonstrated where three FBGs have been successfully interrogated, however, a unit capable of interrogating 36 sensors has not yet been designed and there is much left to be done to produce such a unit.

The final major area for future work is *in vivo* testing. If a TDM interrogation system is still not ready, this can be achieved by using a prototype sensor of approximately 15 FBGs, interrogated with conventional WDM techniques. Successfully completing such testing would be a significant step towards generating potential industry interest in this technology.

# Bibliography

[1] D. A. Singlehurst, C. R. Dennison, and P. M. Wild, "A distributed pressure measurement system comprising multiplexed in-fibre Bragg gratings within a flexible super-structure," *Journal of Lightwave Technology*, vol. PP, no. 99, pp. 1-1, 0.

[2] "The Esophagus (Human Anatomy): Picture, Function, Conditions, and More," *WebMD*. [Online]. Available: http://www.webmd.com/digestive-disorders/picture-of-the-esophagus. [Accessed: 13-Jun-2012].

[3] B. Kuo and D. Urma, "Esophagus - anatomy and development," *GI Motility online*, May 2006.

[4] A. J. Bredenoord and A. J. P. M. Smout, "High-resolution manometry," *Digestive and Liver Disease*, vol. 40, no. 3, pp. 174-181, Mar. 2008.

[5] R. H. Holloway, "Esophageal manometry," *GI Motility online*, May 2006.

[6] J. G. Brasseur and W. J. Dodds, "Interpretation of intraluminal manometric measurements in terms of swallowing mechanics," *Dysphagia*, vol. 6, no. 2, pp. 100–119, 1991.

[7] I. Cook et al., "Opening mechanisms of the human upper esophageal sphincter," *American Journal of Physiology-Gastrointestinal and Liver Physiology*, vol. 257, no. 5, p. G748–G759, 1989.

[8] J. P, K. PJ, L. JA, S. V, and H. T, "Upper esophageal sphincter opening and modulation during swallowing.," *Gastroenterology*, vol. 97, no. 6, p. 1469, Dec. 1989.

[9] Pal, Anupam, R. Williams, Cook, Ian, and Brasseur, James, "Intrabolus pressure gradient identifies pathological constriction in the upper esophageal sphincter during flow," 2003.

[10] J. Ren et al., "Determinants of intrabolus pressure during esophageal peristaltic bolus transport," *The American Journal of Physiology*, vol. 264, no. 3 Pt 1, pp. G407-413, Mar. 1993.

[11] P. J. Kahrilas, J. Dent, W. J. Dodds, W. J. Hogan, and R. C. Arndorfer, "A method for continuous monitoring of upper esophageal sphincter pressure," *Digestive Diseases and Sciences*, vol. 32, no. 2, pp. 121-128, Feb. 1987.

[12] S. K. Ghosh, P. Janiak, M. Fox, W. Schwizer, G. Hebbard, and J. Brasseur, "Physiology of the oesophageal transition zone in the presence of chronic bolus retention: studies using concurrent high resolution manometry and digital fluoroscopy," *Neurogastroenterology & Motility*, vol. 20, no. 7, pp. 750–759, 2008.

[13] R. Tutuian, I. Mainie, A. Agrawal, R. M. Gideon, P. O. Katz, and D. O. Castell, "Symptom and Function Heterogenicity Among Patients with Distal Esophageal Spasm: Studies Using Combined Impedance|[ndash]|Manometry," *The American Journal of Gastroenterology*, vol. 101, no. 3, pp. 464-469, Mar. 2006.

[14] Ghosh, Sudip, Pandolfino, John, Zhang, Qing, Jarosz, Andrew, and Kahrilas, Peter, "Deglutive upper esophageal sphincter relaxation: a study of 75 volunteer subjects using solid-state high-resolution manometr." 2006.

[15] W. G. Paterson, "Esophageal peristalsis," *GI Motility online*, May 2006.

[16] J. W. Arkwright et al., "Design of a high-sensor count fibre optic manometry catheter for in-vivo colonic diagnostics," *Optics express*, vol. 17, no. 25, pp. 22423–22431, 2009.

[17] M. Fox et al., "High-resolution manometry predicts the success of oesophageal bolus transport and identifies clinically important abnormalities not detected by conventional manometry," *Neurogastroenterology & Motility*, vol. 16, no. 5, pp. 533-542, Oct. 2004.

[18] P. G. DINNING, J. W. ARKWRIGHT, H. GREGERSEN, G. O'GRADY, and S. M. SCOTT, "Technical advances in monitoring human motility patterns," *Neurogastroenterology & Motility*, vol. 22, no. 4, pp. 366-380, Apr. 2010.

[19] S. Voigt et al., "Homogeneous catheter for esophagus high-resolution manometry using fiber Bragg gratings," *Proceedings of SPIE*, vol. 7559, no. 1, p. 75590B-75590B-10, Feb. 2010.

[20] P. L. Swart, B. M. Lacquet, and A. A. Chtcherbakov, "Chirped fiber Bragg grating sensor for pressure and position sensing," *Optical Engineering*, vol. 44, no. 5, pp. 054402-054402-4, May 2005.

[21] R. M. Measures, *Structural Health Monitoring With Fiber Optic Technology*, 1st ed. San Diego, California, USA: Academic Press, 2001.

[22] Y.-J. Rao, "In-fibre Bragg grating sensors," *Measurement Science and Technology*, vol. 8, no. 4, pp. 355-375, Apr. 1997.

[23] M. Majumder, T. K. Gangopadhyay, A. K. Chakraborty, K. Dasgupta, and D. K. Bhattacharya, "Fibre Bragg gratings in structural health monitoring—Present status and applications," *Sensors and Actuators A: Physical*, vol. 147, no. 1, pp. 150-164, Sep. 2008.

[24] K. O. Hill and G. Meltz, "Fiber Bragg grating technology fundamentals and overview," *Lightwave Technology, Journal of*, vol. 15, no. 8, pp. 1263–1276, 1997.

[25] David, Nigel, "Fiber Optic Sensors for PEM Fuel Cells," 2011.

[26] C. R. Dennison, P. M. Wild, D. R. Wilson, and P. A. Cripton, "A minimally invasive in-fiber Bragg grating sensor for intervertebral disc pressure measurements," *Measurement Science and Technology*, vol. 19, p. 085201, 2008.

[27] P. L. Swart, B. M. Lacquet, and A. A. Chtcherbakov, "Chirped fiber optic Bragg grating esophageal pressure sensor," in *Optical Fiber Sensors Conference Technical Digest, 2002. OFS 2002, 15th*, 2002, pp. 235–238.

[28] F. H. Gravesen, P. Funch-Jensen, H. Gregersen, and A. M. Drewes, "Axial force measurement for esophageal function testing," *World journal of gastroenterology: WJG*, vol. 15, no. 2, p. 139, 2009.

[29] M. Becker et al., "Fiber-optical high-resolution esophagus manometry based on drawing-tower fiber Bragg gratings," in *Proceedings of the 3rd WSEAS international conference on Advances in sensors, signals and materials*, 2010, pp. 41–44.

[30] J. Arkwright et al., "In-vivo demonstration of a high resolution optical fiber manometry catheter for diagnosis of gastrointestinal motility disorders," *Optics express*, vol. 17, no. 6, pp. 4500–4508, 2009.

[31] J. W. Arkwright et al., "Measurement of Muscular Activity Associated With Peristalsis in the Human Gut Using Fiber Bragg Grating Arrays," *IEEE Sensors Journal*, vol. 12, no. 1, pp. 113-117, Jan. 2012.

[32] J. W. Arkwright et al., "A fibre Bragg grating manometry catheter for in-vivo diagnostics of swallowing disorders," in *Opto-Electronics and Communications Conference, 2008 and the 2008 Australian Conference on Optical Fibre Technology. OECC/ACOFT 2008. Joint conference of the*, 2008, pp. 1-2.

[33] P. Ask and P. Â. Öberg, "Pressure integrating transducer for oesophageal manometry," *Medical & Biological Engineering & Computing*, vol. 17, no. 3, pp. 360-364, May 1979.

[33] D. Singlehurst, Personal Communication. 01-Oct-2011.

[35] J. W. Arkwright et al., "Design and clinical results from a fibre optic manometry catheter for oesophageal motility studies," *Proceedings of SPIE*, vol. 7004, no. 1, p. 70042D-70042D-4, Apr. 2008.

[36] J. E. Pandolfino, S. K. Ghosh, Q. Zhang, A. Jarosz, N. Shah, and P. J. Kahrilas, "Quantifying EGJ morphology and relaxation with high-resolution manometry: a study of 75 asymptomatic volunteers," *American Journal of Physiology-Gastrointestinal and Liver Physiology*, vol. 290, no. 5, p. G1033–G1040, 2006.

[37] B. J. Soller, D. K. Gifford, M. S. Wolfe, and M. E. Froggatt, "High resolution optical frequency domain reflectometry for characterization of components and assemblies," *Opt. Express*, vol. 13, no. 2, pp. 666–674, 2005.

[38] S. T. Kreger, D. K. Gifford, M. E. Froggatt, B. J. Soller, and M. S. Wolfe, "High Resolution Distributed Strain or Temperature Measurements in Single- and Multi-Mode Fiber Using Swept-Wavelength Interferometry," in *Optical Fiber Sensors*, 2006, p. ThE42.

[38] Zhang, Jinye. Personal Communication. 20-Nov-2011.

[40] K. S. C. Kuang, W. J. Cantwell, and P. J. Scully, "An evaluation of a novel plastic optical fibre sensor for axial strain and bend measurements," *Measurement Science and Technology*, vol. 13, p. 1523, 2002.

[41] R. J. Bartlett, R. Philip-Chandy, P. Eldridge, D. F. Merchant, R. Morgan, and P. J. Scully, "Plastic optical fibre sensors and devices," *Transactions of the Institute of Measurement and Control*, vol. 22, no. 5, pp. 431-457, Dec. 2000.

[42] C. R. Dennison and P. M. Wild, "Enhanced sensitivity of an in-fibre Bragg grating pressure sensor achieved through fibre diameter reduction," *Measurement Science and Technology*, vol. 19, no. 12, p. 125301, Dec. 2008.

[43] Kojima, Seiji, Komatsuzaki, Shinji, Kurosawa, Yoshinori, and Hongo, Akihito, "Embedding type strain sensors using small-diameter fiber bragg grating to composite laminate structures," *Hitachi Cable Review*, vol. 23, Aug. 2004.